Simulation, Design and Characterization of a Silicon Piezoresistive Accelerometer, Fabricated by a Bipolar-Compatible Industrial Process

Dissertation
submitted to the Faculty of Sciences of the University of Neuchâtel
to obtain the degree of Doctor of Sciences

by

Thomas Tschan

Dipl. Phys. ETHZ

Institute of Microtechnology
University of Neuchâtel
Breguet 2
CH-2000 Neuchâtel
Switzerland

printed by Difo-Druck GmbH, D-8600 Bamberg

Thought is the work
of the Mind,

as

Love is the occupation
of the Spirit.

Joan Walsh Anglund

IMPRIMATUR POUR LA THÈSE

Simulation, conception et caractérisation
des accéléromètres piézorésistifs de silicium
fabriqués dans une technologie compatible
avec un procédé bipolaire industriel

de Monsieur Thomas Tschan

UNIVERSITÉ DE NEUCHÂTEL

FACULTÉ DES SCIENCES

La Faculté des sciences de l'Université de Neuchâtel
sur le rapport des membres du jury,

Messieurs N. de Rooij, A. Shah, H. Seidel
(Munich) et J. Knutti (Fremont, USA)

autorise l'impression de la présente thèse.

Neuchâtel, le 15 juin 1992

Le doyen :

A. Robert

Abstract

A silicon accelerometer consists of a silicon mass suspended by thin silicon beams. The displacement of the mass due to accelerations can be detected by several methods, one of which is to measure the resistivity change of strain gauges implanted into the thin silicon beams. This work aims to produce a piezoresistive accelerometer with a reasonable sensitivity, high resonance frequency and which is protected against overforces.

This text describes the systematic analysis of the development steps of a piezoresistive silicon accelerometer fabricated with a bipolar compatible industrial process. First, the device is simulated using analytical formulae and finite element modeling. Based on the restrictions given by the chosen fabrication technology the optimization of a four-beam bridge-type device is discussed. For the fabrication of the sensitive device an industrial bipolar process has been adapted which resulted in a process sequence with only four additional steps. One of these, the deep dry etching of silicon, has been investigated for two gas combinations and optimized for our application. One of the most important steps is the encapsulation and damping of the sensitive device. Both liquid- and gas-damped accelerometers were realized and compared to theoretical predictions. The squeeze film theory was applied for both damping mediums and agreed well with experimental results. A simple chip-by-chip encapsulation method allows the device to be critically damped and to be overforce protected. The development resulted in a 50 *g* air-damped accelerometer with a useable frequency range of 1200 Hz over the whole temperature range of -20° to 120°C.

Contents

List of Notations

Symbol	Description	Unit
α	plate aspect ratio	
β	magnification factor	
γ	damping ratio	
ε	strain	
η	dynamic viscosity	Pa s
θ	phase angle	rad
Θ	moment of inertia	kg m^2
κ_s	force reduction factor	
λ	eigenvalue	
λ	mean free molecular path	m
μ	mass per unit length of the beam	kg/m
υ	kinematic viscosity	m^2/s
ξ	nondimensional plate displacement	
$[\pi]$	piezoresistance tensor	
π_{kl}	piezoresistive coefficients	Pa^{-1}
π_l	longitudinal piezoresistive coefficient	Pa^{-1}
π_t	transversal piezoresistive coefficient	Pa^{-1}
ρ	resistivity	Ω cm
ρ	density	kg/m^3
σ	squeeze number	
σ	stress	N/m^2
σ_l	longitudinal stress	N/m^2
σ_t	transversal stress	N/m^2
τ	nondimensional time	
ϕ	angle	rad
χ	nondimensional film thickness perturbation amplitude	
ψ	nondimensional pressure perturbation	
ω	frequency	rad/s
ω_0	resonance frequency	rad/s
ω_c	cutoff frequency	rad/s

a	acceleration	m/s^2
A	(cross sectional) area	m^2
b	angular frequency	rad/s
c	coefficient of viscous damping	kg/s
c_s	speed of sound in fluids	m/s
c_{sq}	squeeze film damping coefficient	kg/s
C	overall chip size ($C = 2L + S$)	m
C_i	constants	
D	junction depth of the piezoresistor	m
D_o	characteristic diameter	m
e	variation in the plate spacing	m
E	modulus of elasticity	N/m^2
E_F	Fermi level	eV
f	frequency	s^{-1}
f_{res}	resonance frequency	s^{-1}
f_o	nondimensional damping force	
f_1	nondimensional spring force	
F	force	N
$F_\beta(\alpha)$	Fermi integral	
h	gas film thickness	m
h_o	mean spacing of the plate	m
H	thickness of the seismic mass	m
I_y	moment of inertia of the cross section with respect to the axis y	m^{-4}
k	spring constant	N/m
K	gauge factor	
K_{max}	maximum kinetic energy	J
Kn	Knudsen number	
l	length of a plate	m
L	length of the beam of an accelerometer	m
m	mass	kg
m*	effective or added mass	kg
M	moment	Nm
n	number of beams	
N	dopant concentration	cm^{-3}
p(x,t)	force per unit length in function of time and space	N/m
p(x,y)	pressure	N/m^2
P	length of a piezoresistor	m
P(N,T)	piezoresistance factor	
P_a	ambient pressure	N/m^2
Q	amplitude of vibration	m
r	curvature radius	m
R	resistance	Ω

R_a	reaction force at the end a	N
s_{kl}	stress tensor	N/m^2
S	side length of the quadratic seismic mass at the top side	m
S_o	sensitivity of the accelerometer	$\mu V/V\ g$
t	time	s
T	thickness of beam	m
T	temperature	K or °C
u(t)	deflection of the beam in function of time	m
U_{max}	maximum potential energy	J
V	width of piezoresistor	m
w	width of a plate	m
w(x,t)	deflection of the beam in function of time and space	m
W	width of beam	m
x,y,z	coordinates	m
z(x)	deflection of the beam in function of x	m

Constants :

E	module of elasticity of Si in the [110] direction	$1.69\ 10^{11}$ Pa
g	terrestrial acceleration	$9.81\ ms^{-2}$

Abbreviations :

FS	full scale
FSO	full scale output
KOH	potassium hydroxide
OCP	open circuit potential
PE	plasma etching
RF	radio frequency
RIE	reactive ion etching
SFB	silicon fusion bonding
TC	temperature coefficient
TCO	temperature coefficient of offset
TCR	temperature coefficient of piezoresistor
TCS	temperature coefficient of sensitivity

Chapter 1
Introduction

The first section of this chapter describes several aspects of silicon sensors with particular emphasis on accelerometers and their applications. The different silicon based sensing technologies are compared in section 1.2. The next section summarizes the history of silicon accelerometers. Section 1.4 explains the background of the work. The piezoresistive effect in p-type silicon is briefly reviewed in section 1.5. Finally the structure of this work is outlined.

1.1 SILICON ACCELEROMETER - AN IMPORTANT MICROSENSOR

Sensors are the sense-organ of the electronic world and form an interface between the worlds of physics and chemistry and modem, electronic circuits. In order to improve the flexibility of automated systems, a feedback signal from a sensitive element which has high quality and reliability is needed. Silicon sensors produce an electrical output that corresponds to some physical, chemical or biological quantity, for example pressure, acceleration, force, ion concentration or a biological molecule. The sensing elements are often the critical components determining the feasibility of new products. For example, all modem cars rely on a fuel delivery system based on manifold absolute pressure and flow sensors which are sold in volume under $ 15.

Integrated circuits have changed many aspects of our life. However, while the microelectronic revolution has been spreading, a more subtle technology - silicon micromachining - has been gradually developed leading to the precisely defined three dimensional sculpting of silicon. Since only silicon can meet the aggressive cost or cost/performance requirements of new sensor products, almost all new sensor applications are silicon-based. Silicon technology is also displacing older technology in traditional applications. Using standard or modified semiconductor batch processing technology allows lower production costs and higher profit to be made from the huge know-how of silicon processing in, for example ultra-pure materials, advanced processes, high volume manufacturing and packaging technologies. In integrated circuits only the electrical properties of silicon are exploited. Micromechanics utilizes both electrical and mechanical properties of silicon and thus creates a new generation of electro-mechanical silicon chips.

There are many factors making silicon micromachining technology so attractive. Silicon is almost a perfect mechanical material, especially for sensors. It is stronger than steel, it does not show mechanical hysteresis, its hardness is the same as quartz and its thermal conductivity is near that of aluminum. Silicon is also readily machineable with a variety of chemical and electrochemical etchants. When all these mechanical attributes are combined with the electronic performance of silicon and its sensitivity to light, magnetic fields and stress, it becomes obvious that silicon provides a unique fundamental base technology for all types of micromechanical sensors and actuators. In addition to these excellent properties, silicon brings significant advantages from the established mainstream electronic industry.

Due to the low price and reliability of the sensors, the market is growing very vigorously (see Fig. 1.1). The increase is 10 - 30 %/year for the various application sectors [1]. The growth of silicon based sensors is expected to be much faster than the total market. The best opportunities are for low cost, high volume sensors for use with microprocessors. Pressure sensors represent the largest established market for sensors (1990: 1.4 Billion ECU) [2]. The silicon accelerometer market is expected to grow faster than the one for pressure sensors, on average about 27%/year [3]. The years following 1992 will see a

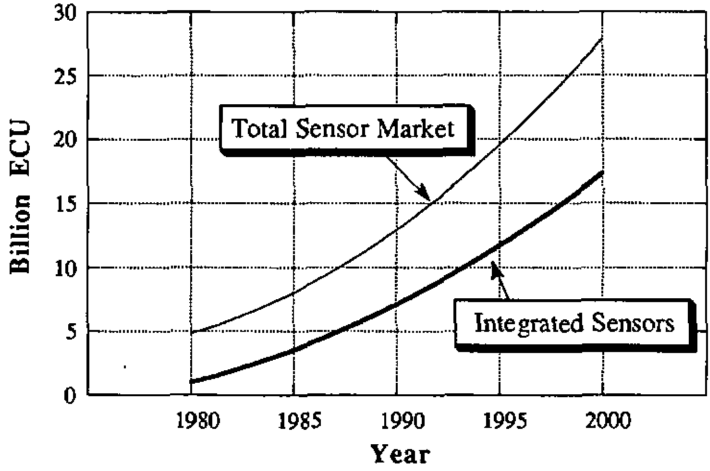

Fig. 1.1 Sensor market predictions [4]

step increase in automotive acceleration sensors usage due to volume implementation of suspension and air bags which have incorporated microprocessors and microcontrollers.

Acceleration is for most applications an important parameter, since both velocity and displacement can be calculated by single and double integration, respectively, in time. Due to the improvements of silicon accelerometers the prices have dropped and the reliability has increased in such a way that they can be implemented into huge volume products (i.e. automotive market). Table 1.I shows the different fields of applications of silicon accelerometers. As the position of an object (e.g. vertical or horizontal) can be detected also by an accelerometer, there are many possible low cost applications in the consumer market for example, a clothes iron in a horizontal position and not moving can be switched off for safety reasons.

The silicon sensor market is gradually moving in the direction analogous to other electronic components: higher integration. There are two ways for a possible on-chip integration : electronic or mechanical integration. In the area of electronic integration there are several possible levels of integration enhancing sensor performance. In the case of piezoresistive pressure sensors or accelerometers the basic sensing element includes only four resistors. These resistors require additional signal conditioning in order to provide a useful signal for a final user application. The passive on-chip circuit integration may include offset balancing, temperature compensation of both offset and sensitivity and even signal normalization. As silicon is used as basic material it is possible to integrate on the same chip active circuitry for signal amplification. One major disadvantage of further integration for most applications is the higher engineering and tooling cost required to provide efficient manufacturing of the device. Therefore the crossover point above which higher level of integration offers lower cost sensors is a function of the

Table 1.I Fields of application for integrated accelerometers [3]

Market segment	Application
Automotive	Smart Suspension: 4 to 6 accelerometers / car
	ABS Brakes 1 accelerometer / car
	Air Bag actuation
Aerospace	Closed Loop (Servo) Acceleration Sensors
	Weapons (missiles)
	Navigation
Automation	Vibration sensors
Control	Earth quake monitoring
Transportation	Handling of fragile goods
Medical	Monitoring of body motion (pace maker)

existing technology infrastructure and knowledge : further integration might become expensive. For only a few and very high performance applications, full on-chip signal conditioning is reasonable. Sensors which have the sensing element and the signal-processing circuit integrated on one chip are called smart sensors [5]. The integration of further mechanical parts on-chip provides a potential for substantial benefits to the users. For instance Nova Sensor presented a batch fabricated piezoresistive silicon accelerometer [6] with incorporated overforce stops on the same chip (see section 5.2). Thus high volumes needed for new markets can be attained.
The characteristics of different sensing technologies for silicon accelerometers are described in the next section.

1.2 DETECTION OF ACCELERATION

Most accelerometers consist of a mass-spring system, and therefore are based on Newton's second law of motion. The force acting on an accelerated mass corresponds to the product of mass times acceleration. Thus the deflection of the spring is a direct parameter of the acceleration (within the elastic limit).
From now on, we will only consider silicon accelerometers. In that case the spring is a thin silicon beam with a block of silicon as seismic mass at its end (see for instance Fig. 3.15). Under acceleration the seismic mass is deflected which leads to a deformation of the thin silicon beam. There are three main sensing technologies to detect the movement of the mass :

- capacitive
- piezoelectric
- piezoresistive

Their basic characteristics are compared in Table 1.II.
In the **capacitive** case the surface of the mass forms an electrical capacitance with an external electrode. As the accelerometer is encapsulated by either pyrex glass plates [7] or silicon caps [8], which form a small cavity, the counter electrodes can be integrated into the cavity. A movement of the seismic mass due to an applied acceleration changes the capacitance of the parallel-plate capacitor. In order to have a reasonable capacitance change, the mass and the outer electrode are separated by a few microns (≈ 2 μm). This small cavity leads to an overdamping of the sensor at atmospheric pressure [9, 10]. Thus the pressure inside the cavity has to be reduced and to be well controlled, which complicates the production process. A serious problem with capacitive sensors is that the leads connecting the sensor to the outside tend to show stray capacitances which are of the same order as the sensor capacitance. This makes it mandatory to include electronic circuitry on the sensor chip in order to convert the change in capacitance (some pF) into an electrical signal

Table 1.II Comparison of simple sensing technologies [14]

	Capacitive	Piezoelectric	Piezoresistive
Impedance	High	High	Low
Electrical Loading Effects	Very High	High	Low
Size	Large	Small	Moderate
Temperature Range	Very wide	Wide	Moderate
Linearity Error	High	Medium	Low
DC Response	Yes	No	Yes
AC Response	Wide	Wide	Less Wide
Damping Available	Yes	No	Yes
Sensitivity	High	Moderate	Moderate
Zero Shifts due to shock	No	Yes	No
Turn-over or Shunt Calibration	Yes	No	Yes
Electronics Required	Yes	Yes	No
Cost	High	High	Low
Cross axis Sensitivity	Primarily dependent on mechanical design, not transduction		

[11 - 13]. However, this approach is advantageous since it displays a high sensitivity in comparison to the piezoresistive effect [15].

Another way of directly measuring force is based on the **piezoelectric** effect [16]. In many crystalline materials, such as quartz a mechanical stress produces an electric polarization and, reciprocally, an applied electric field generates a mechanical strain. Silicon unfortunately does not show this piezoelectric effect. To circumvent this problem it was found possible to deposit piezoelectric layers on top of the silicon beams. The desired signal conversion then takes place in these layers. In the beginning CdS and CdSe layers were used, today sputtered ZnO films are common and can be deposited in a reliable and silicon process compatible way [17, 18].

Most solid-state sensors for mechanical signals are based on the **piezoresistive** effect. The change in specific conductivity due to an applied strain is defined as piezoresistance. It was first reported by Lord Kelvin in 1856. Based on this effect, strain gauges were developed that today are widely used to measure force. A very short summary of the physical background of this effect is given in section 1.5. In 1954 Smith reported experiments that showed that the piezoresistive effect was about a hundred times greater in silicon and germanium than in metallic conductors. Several years later this fact was used for the design of the first silicon pressure sensors, having four piezoresistors diffused on its thin membrane and connected to a Wheatstone bridge. Two great advantages of the piezoresistive principle are that a true DC

response can be measured and secondly no electronic circuitry is needed for the detection of the voltage change.
Other detection methods like the piezojunction effect [19, 20], resonators [21, 22], thermopile [23] or integrated optic detection [24] have never reached the level of low cost devices for industrial application.

1.3 HISTORY OF SILICON ACCELEROMETERS

The first silicon micromachined accelerometers with integral packaging were developed by Roylance at Stanford University in 1975 [25]. That device was a single cantilever structure with a silicon mass and piezoresistive sensing. Seven years later, Petersen et al. demonstrated a miniature deflectable cantilever beam based on capacitive detection, which was fabricated immediately adjacent to the MOS signal-detection circuitry [26]. A piezoelectric accelerometer consisting of a cantilevered beam structure overcoated with a ZnO film and with the electrical signal directly coupled to the gate of a MOS transistor was realized by Chen et al. in 1982 [17]. A year later he added a silicon proof mass to obtain a higher sensitivity using the same detection principle [18]. In 1983 Rudolf published a micromechanical capacitive accelerometer with a two-point inertial-mass suspension [27]. The sensitive device was encapsulated by two anodically bonded glass wafers which formed the counter-electrodes. Benecke presented in 1985 a frequency-selective, piezoresistive silicon vibration sensor, consisting of an array of mechanical oscillators [28]. At Transducers' 87 different approaches to achieve critical damping of piezoresistive accelerometers were presented. A cantilever-type accelerometer mounted on a thick damping material in order to get a well damped device was proposed by Tsugai et al. [29]. Nakamura used oil as a damping material for his accelerometer having silicon stoppers on both sides of the gold-plated silicon mass [30]. Another important parameter of an accelerometer is its cross-axis sensitivity. A Wheatstone bridge configuration of eight piezoresistors which theoretically eliminates all cross acceleration sensitivity was published by Sandmaier at the same conference [31]. The combination of integrated overrange protection and integral air damping of a piezoresistive accelerometer was developed by Barth from NOVA Sensor [6]. There was still one pyrex wafer used for the overrange protection on one side. Another approach to damp and to protect against overload piezoresistive silicon accelerometers was presented by Knutti from ICSensors in 1988 [32]. He enclosed the sensitive die from both sides with a silicon cap having integrated over force stops. The small cavity filled with gas damped the device critically. Olney from Endevco altered the damping characteristics of their air-damped capacitive accelerometer by the number and location of grooves and holes in the moving plate [33]. An uniaxial accelerometer in silicon based on the piezojunction effect was first published by Puers in 1988 [19]. Until 1989 it was not possible to test a piezoresistive accelerometer if it is free and working or whether it is broken. Thus the self-test feature developed by Allen from ICSensors was a great improvement since it allows to test the functionality of the device without applying any acceleration [34-36]. Furthermore this self-test feature, which is based on the capacitive principle, can be used for temperature compensation. In contrast to piezoresistive accelerometers the cross-axis sensitivity of capacitive accelerometers can not be compensated electrically. Thus a high level of symmetry of the sensitive device is required. The sensor assembly proposed by Henrion [37] consists of three silicon chips, bonded together at the wafer level. The center layer is comprised of the proof mass, which is supported by eight springs, four at the top and four at the bottom. Electrochemical etching from both sides of the wafer forms a double-sided symmetrical structure which minimizes cross-axis sensitivity and harmonic distortion. Suzuki et al. utilized a pulse width modulation technique to detect the acceleration of their capacitive accelerometer [38]. In order to increase the effective mass compared to the size of the die Yamada proposed 1990 a piezoresistive silicon accelerometer with a surrounding mass structure [39]. As further integration is advantageous a surface micromachined piezoresistive accelerometer was proposed by Dunn [40]. Analog Devices announced the successful high volume fabrication of a surface micromachined accelerometer at the beginning of 1992 [41, 42]. A capacitive accelerometer using sense element structures fabricated on the surface of a wafer was presented by Cole in 1991 [43]. The sense element consists of an asymmetrically shaped flat plate of metal supported above the substrate surface by two torsion bars.

1.4 BACKGROUND OF THE WORK

This short section explains what background has led us to develop a piezoresistive silicon accelerometer. When this work started in April 1988, piezoresistive silicon pressure sensors were already well established on the market. At that time the first piezoresistive silicon accelerometers were commercially available. The opportunity to have a cheap and reliable device for an enormously increasing market intensified the worldwide research on silicon accelerometers. Since at our institute the work on the design, fabrication and characterization of piezoresistive pressure sensors [44] was in its final phase, a lot of experience on electrochemical etch-stop and piezoresistors existed already. As that project was done in collaboration with ASCOM Microelectronics Bevaix and KELLER AG Winterthur, both partners agreed to contribute to the work on piezoresistive accelerometers. The combination of a semiconductor production company (ASCOM) and a specialist in the encapsulation of piezoresistive pressure sensors was very promising. The objective was to develop a silicon piezoresistive accelerometer based on the same bipolar compatible process as is used for the pressure sensors fabricated by ASCOM. It was decided to install two plasma etching facilities in our small R&D line and at the same time ASCOM planned to build a completely new 4 inch production line. Furthermore the Institute of Microtechnology ordered workstations for finite element modeling and computer aided design. Therefore the development that is reported in this text was able to be performed within an excellent environment.

1.5 PIEZORESISTIVITY OF MONOCRYSTALLINE SILICON

The change in specific conductivity due to an applied strain is defined as piezoresistance. This effect in silicon is summarized in this section based on the literature of the last 40 years [45-60]. First, formulae which describe the crystal-orientation dependence of the piezoresistive coefficients are developed. As these coefficients depend also on temperature and dopant concentration, their influence will be discussed at the end of this section.

In 1954 C.S. Smith discovered the relatively large piezoresistive effect in silicon [45]. He was interested in crystal symmetry. Piezoresistivity is one of the few electrically anisotropic properties of materials.

A strain affects the resistance of a conductor both because of changes in the specific conductivity and because of changes in the length and cross-sectional area. In metals, the two effects have the same order of magnitude, but in certain semiconductors such as germanium and silicon, the change in specific conductivity, which is defined as piezoresistance, is typically far more significant than the change in dimensions. In silicon resistors the fractional change of resistance is proportional to the increase of the strain to which it is subjected. For small change this relation can be expressed by the equation

$$\frac{\Delta R}{R} = K \, \Delta\varepsilon \qquad (1.1)$$

where R = resistance, K = proportionality constant or gauge factor and ε = strain.

For conventional metal strain gauges the gauge factor is about 2. However, for silicon resistors a gauge factor of 200 is achievable.

The overall resistance change for a silicon piezoresistor can be written as

$$\frac{\Delta R}{R} = \frac{\Delta \rho}{\rho} + \frac{\Delta P}{P} - \frac{\Delta D}{D} - \frac{\Delta V}{V} \tag{1.2}$$

where ρ, P, D and V are respectively resistivity, length, thickness and width of the silicon resistor. Since the effect of resistivity change is the predominant effect, eq. 1.2 can be reduced to

$$\frac{\Delta R}{R} \approx \frac{\Delta \rho}{\rho} \tag{1.3}$$

Since the elastic shear strain that can be introduced into a crystalline solid is usually quite small, only the linear theory of the relationship between the resistivity and the strain is required. The resistivity of a material, unstrained or in any state of homogeneous strain, can be described by a symmetric second rank tensor, containing a set of six independent coefficients. The state of strain of the material can also be described by a symmetric second rank tensor, or another set of six coefficients. Thus the most general linear relationship between the resistivity and the strain can be expressed by six linear equations, involving thirty-six coefficients. Using the subscripts scheme as is customary in the theory of elastic properties, the piezoresistance equations for a cubic crystal become

$$\rho_i = \rho_o \left[1 + \sum_{j=1}^{6} \pi'_{ij}\, s_j \right] \qquad \text{for } i = 1, 2, 3 \tag{1.4}$$

$$\rho_i = \rho_o \left[\sum_{j=1}^{6} \pi'_{ij}\, s_j \right] \qquad \text{for } i = 4, 5, 6 \tag{1.5}$$

The π'_{ij} coefficients are the piezoresistive coefficients, ρ_o is the isotropic resistivity of the unstressed crystal and s_j is the stress matrix. The π_{ij} coefficients form a square matrix of 36 terms and are primed to indicate the arbitrary orientation of the coordinate system. For crystals with cubic symmetry, as silicon or germanium, the components of the piezoresistance tensor can be reduced to three independent coefficients π_{11}, π_{12} and π_{44}. When the coordinate axes are aligned with the crystal axes, it has the following form

$$[\pi] = \begin{vmatrix} \pi_{11} & \pi_{12} & \pi_{12} & 0 & 0 & 0 \\ \pi_{12} & \pi_{11} & \pi_{12} & 0 & 0 & 0 \\ \pi_{12} & \pi_{12} & \pi_{11} & 0 & 0 & 0 \\ 0 & 0 & 0 & \pi_{44} & 0 & 0 \\ 0 & 0 & 0 & 0 & \pi_{44} & 0 \\ 0 & 0 & 0 & 0 & 0 & \pi_{44} \end{vmatrix} \tag{1.6}$$

However, all 36 of the coefficients may be nonzero when referred to a Cartesian system of arbitrary orientation relative to the crystallographic axes. For most applications it is advantageous to divide the stress in relation to the resistor into a longitudinal and transverse direction :

$$\frac{\Delta R}{R} = \pi_l \cdot \sigma_l + \pi_t \cdot \sigma_t \tag{1.7}$$

with the coefficients

$$\begin{aligned} \pi_l &= \pi_{11} - 2(\pi_{11} - \pi_{12} - \pi_{44})\, F_{11} \\ \pi_t &= \pi_{12} + (\pi_{11} - \pi_{12} - \pi_{44})\, F_{12} \end{aligned} \tag{1.8}$$

and the dimensionless direction factors F_{11}, F_{12} respectively, which are given by the angle between the direction of stress and the crystallographic axes. The piezoresistive coefficients π_{ix} for n- and p-doped silicon are given in Table 1.III.

Using Hooke's law in eq. 1.7, we will find eq. 1.1 again, with $E_l\,\pi_l$ and $E_t\,\pi_t$ as the longitudinal and transverse gauge factors, respectively, and E_l and E_t the Youngs' moduli in the corresponding direction.

A graphical representation of the coefficients π_l and π_t for p-type silicon with (001) orientation is given in Fig. 1.2. Both coefficients are 0 in the <100> directions and have their maxima in the <110> directions. The corresponding coefficients for a n-type substrate with (001) orientation look similar, but their maxima are in the <100> and their local minima (≠ 0) are in the <110> direction. Since KOH, an anisotropic etchant (see for ex. [61, 62]), is used for most silicon micromachined devices, the orientation of the structures and thus of the piezoresistors depends on the etch characteristics. The surface of the wafer is a (001) plane and the edges are intersections of the fast etching {001}

Table 1.III Piezoresistive coefficients for n- and p-doped silicon [56]

	ρ [Ωcm]	π_{11} [10^{-11} Pa^{-1}]	π_{12} [10^{-11} Pa^{-1}]	π_{44} [10^{-11} Pa^{-1}]
p - silicon	7.8	+ 6.6	− 1.1	+ 138.1
n - silicon	11.7	− 102.2	+ 53.4	− 13.6

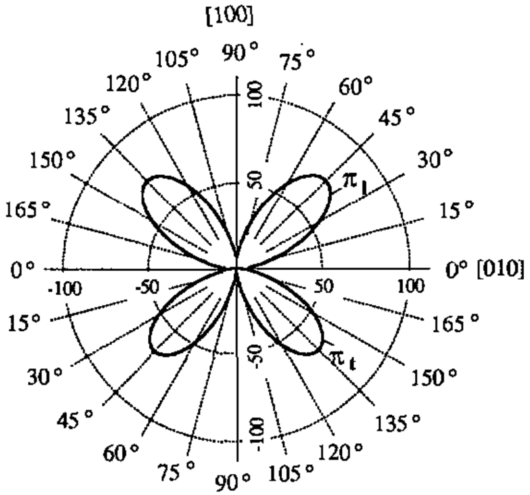

Fig. 1.2 Piezoresistive coefficients in the (001) plane of Si at room temperature [56]

planes and of the very slow etching {111} planes. This leads to a side orientation on the wafer surface in the <110> direction. In this direction, the longitudinal and transverse coefficients of p-type silicon are about twice that of n-type silicon. Thus p-type and not n-type piezoresistors are implanted into the beams of silicon piezoresistive micromechanical devices. The longitudinal and transverse coefficients for both types of silicon are listed in Table 1.IV.

The coefficients are not only dependent on the crystal orientation but also on the dopant concentration and on temperature. Kanda [56] has shown, that in general, the piezoresistance coefficient $\pi(N,T)$ with an impurity concentration N and at a temperature T can be written in the form

$$\pi(N,T) = P(N,T) \; \pi(300\ K) \tag{1.9}$$

where P(N,T) is the piezoresistance factor and given by

Table 1.IV Longitudinal and transversal piezoresistive coefficients and gauge factors of n- and p-doped (001) silicon for [110] directions in the crystal (ρ (n-Si) = 7.8 Ωcm, ρ (p-Si) = 11.7 Ωcm) [56]

[110] direction	π_l or π_t	π_l or π_t [10^{-11} Pa^{-1}]	gauge factor	
longitudinal	$1/2(\pi_{11}+\pi_{12}+\pi_{44})$	71.8 -31.2	121.3 -52.7	p-Si n-Si
transversal	$1/2(\pi_{11}+\pi_{12}-\pi_{44})$	-66.3 -17.6	-112.1 -29.7	p-Si n-Si

$$P(N,T) = \frac{300}{T} \cdot \frac{F'_{s+(1/2)}(E_F/kT)}{F_{s+(1/2)}(E_F/kT)} \tag{1.10}$$

$$\text{and} \quad F_\beta(\alpha) = \int_0^\infty \frac{x^\beta}{1 + e^{x-\alpha}}\, dx \tag{1.11}$$

is the Fermi integral and a prime indicates derivative of the Fermi integral with respect to E_F/kT. The Fermi integral is a function of temperature and the Fermi energy. The Fermi energy is determined from N by using the following relation :

$$N = 4\,\pi \left(\frac{2\, m^*\, k\, T}{h^2}\right)^{3/2} F_{1/2}(E_F/kT) \tag{1.12}$$

where m* is the effective mass. For p-type silicon, the scattering exponent s is -1/2 (see eq. 1.10) and $m^* = 0.55\ m_{electron}$ [56]. The graph of P(N,T) is shown in Fig. 1.3.

An important advantage of piezoresistors is that very thin layers can be fabricated by means of standard microelectronic technology, so that the current is limited to the surface of the element under bending, where stresses are maximum. Moreover, the geometry of the resistors can be easily defined.

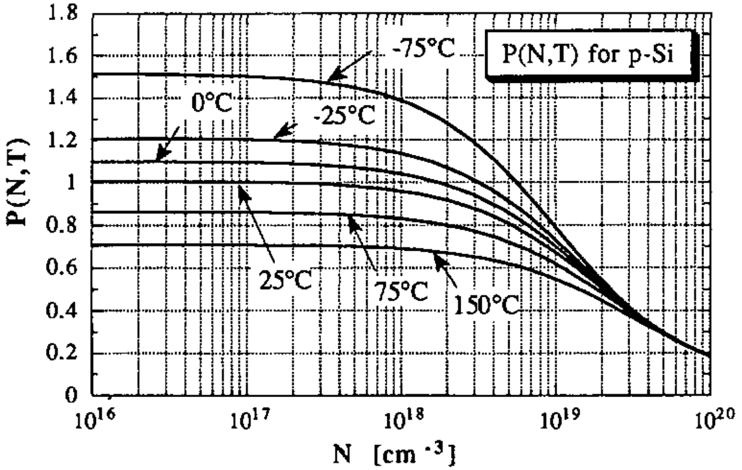

Fig. 1.3 Piezoresistance factor P(N,T) for p-silicon in function of dopant concentration and temperature [56]

In silicon technology typical junction depths are between 0.5 and 3 μm. Figure 1.3 shows that the piezoresistance coefficients decrease with increasing impurity concentration. In diffused or implanted resistors the impurity concentration decreases with depth, hence, the piezoresistance coefficients show an increasing profile. To calculate the average temperature dependence of diffused piezoresistors, integration over the depth profile is required. Hence, a relatively high surface concentration does not necessarily result in a very low temperature dependence, as Fig. 1.3 (which is valid for uniform bulk material) would suggest, since the deeper and thus lower doped layers exhibit a higher temperature coefficient. For this reason, shallow implanted resistors with very sharp doping concentration profile can achieve lower temperature dependences than deep diffused resistors with equal sheet resistance.

The interpretation of the large piezoresistance effects in semiconductors in terms of the multivalley model was developed by Smith [45], Herring [63] and Keyes [48]. In the case of silicon, the constant energy surfaces are six ellipsoids in the momentum space aligned with the crystal axes. The application of an anisotropic stress condition now changes the relative energies, and hence changes the occupations in these valleys and electrons will be transferred. Thus the conductivity becomes anisotropic. If, on the other hand, the crystal is stressed in a symmetrical axis of the valleys, no resistance change will be noticed. For more details, we refer to the literature given above.

1.6 OUTLINE OF THE THESIS

This thesis is divided into nine chapters. Chapter 2 presents two basic mass beam configurations of accelerometers and develops analytical formulae for the stress distribution and resonance frequency. In addition the sensor structure is simulated using finite element modeling and predictions are compared with the classical approach.

In chapter 3 the fabrication of the first prototype of the sensor chip is described. Deep dry etching and etch compensation structures are developed and optimized. The design and the process sequence using an industrial, bipolar compatible process are given for the second prototype.

Chapter 4 shows the measurement systems. The performance of unencapsulated sensor chips are discussed and compared with the theoretical predictions.

It is necessary to protect a sensor chip against overload and to damp it. In chapter 5, the damping effects of thin fluid films on a moving plate are theoretically described.

Chapter 6 presents different encapsulation techniques for the sensor chip.

Chapter 7 shows the measured performance of oil- and air-damped accelerometers. The damping film thickness for critical damping is calculated based on the formulae developed in chapter 5. The third part presents the temperature response of offset and sensitivity and discusses the basic ideas of compensation circuits.

Chapter 8 summarizes the conclusions of the preceding chapters and gives some suggestions for further research.

Chapter 2

Simulation of the Sensor Chip

In this chapter the sensitive die of an accelerometer is simulated. There are basically two main types, the cantilever-type with its mass suspended from only one side and the bridge-type having its mass suspended from at least two opposite sides. In the first sections of this chapter, analytical formulae which describe the resonance frequency and the stress distribution in the beams are given for both types. In order to optimize the device performance, a formula for the beam length which maximizes the sensitivity of a bridge-type accelerometer is developed. In addition, the main characteristics are simulated using finite element analysis. In subsection 2.4.4, the results of analytical formulae are compared to those of the finite element modeling.
Parts of this chapter have been published in [64, 65].

2.1 INTRODUCTION

The development of a new type of silicon accelerometer consists of three main steps : design including modeling, fabrication process and characterization. In order to reduce the development time, theoretical predictions are becoming increasingly important [66]. For the last five years Finite Element Modeling (FEM) [67] has been used for the simulation of micromechanical structures [68-70]. This technique enables us to visualize all the different modes of vibration and their corresponding resonance frequencies for any possible structure. Static or dynamic calculations can be done using the boundary conditions closest to reality. Furthermore in the case of a piezoresistive accelerometer, it is possible to optimize the location of the piezoresistors, because detailed stress distributions can be predicted. However, analytical formulae are very powerful - in the case of simple structures - in order to see the dependence of different parameters (sensitivity, resonance frequency) on the dimensions of the device [71, 72].
In this chapter two basic types of silicon piezoresistive accelerometers are simulated using both classical formulae and FEM. First formulae for stress and

resonance frequency are developed for a simple beam under load. Boundary conditions corresponding to an accelerometer sensor chip entirely determine the solution. This analytical approach allows the dimensions of the mass-beam system to be optimized with respect to the desired sensitivity and bandwidth and to the technological constraints of the chosen industrial fabrication process. Results of the FEM are presented and the predictions and limits of both types of simulation are discussed. In section 4.4, the measured performance of fabricated devices will be compared to the theoretical predictions. It has to be noted that throughout this chapter modeling concerns only the sensitive device. The damping and encapsulation effects will be discussed in chapter 5.

2.2 TYPES OF ACCELEROMETERS

In an accelerometer there are many possible ways to suspend the seismic mass using beams. However, we can distinguish two basic configurations of the mass-beam system : the bridge-type and the cantilever-type accelerometer. These are compared below.

bridge-type accelerometer	**cantilever-type accelerometer**
• mass suspended from at least two opposite sides	• mass suspended from one side
• center of mass of the proof mass moves in the z-direction under acceleration in z-direction	• center of mass of the proof mass moves on an arc under acceleration in z-direction
• maximum and opposite stress at each end of the beam under constant acceleration	• nearly uniform stress on the surface of the beam under constant acceleration
• low cross sensitivity	• large sensitivity in the main axis

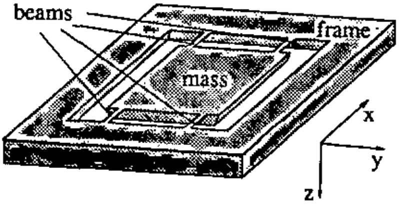

Fig. 2.1 Schematic view of a four-beam bridge-type accelerometer

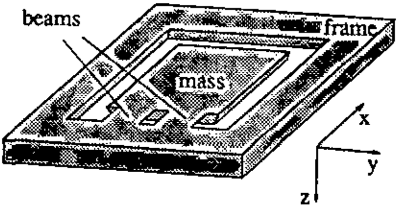

Fig. 2.2 Schematic view of a two-beam cantilever-type accelerometer

2.3 ANALYTICAL FORMULAE

2.3.1 Introduction

Basically an accelerometer can be considered as a beam under load. Therefore pure bending of a simple beam [73-75], which leads to differential equations in space and time, will be treated first. The formulae of the deflection curve and resonance frequency for both types of accelerometers will be deduced by applying the corresponding boundary conditions to the general solution of these differential equations. In this section we follow the treatment of a beam under load as proposed by Timoshenko [76]. Taking into account the technological constraints of the chosen industrial, bipolar compatible fabrication process, a formula which maximizes the sensitivity of a four-beam bridge-type accelerometer for a given chip size is developed in subsection 2.3.5.

2.3.2 Beam under Load

First we derive an expression for the relation between the strain ε and the curvature radius r.
As it can be seen from Fig. 2.3

$$\varepsilon_x = \frac{\overline{SS'} - \overline{NN'}}{\overline{NN'}} = \frac{(r + z)\phi - r\phi}{r\phi} = \frac{z}{r} \tag{2.1}$$

From Hooke's law it follows that the stress σ_x is given by :

$$\sigma_x = \frac{E\,z}{r} \tag{2.2}$$

where E is the modulus of elasticity of silicon.

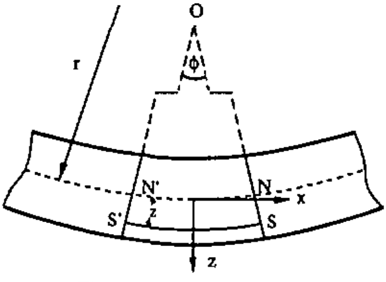

Fig. 2.3 Bent beam

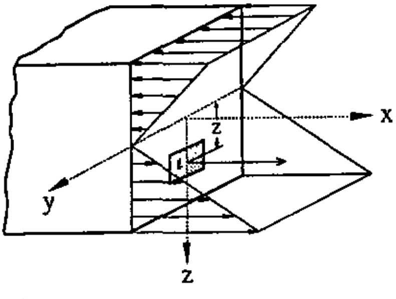

Fig. 2.4 Stress distribution on a cross-section of the beam

As we look at the relation between the moment M and the curvature radius r, let dA denote an elemental area of cross section at distance y from the neutral axis (Fig. 2.4). The force acting on this elemental area is the product of the stress and the area dA, i.e. (Ez/r) dA. The moment of the force acting on the element dA with respect to the neutral axis is (Ez/r)dA z. Adding all such moments over the cross section and setting this result equal to the moment M of the external forces, the following equation for determining the radius of curvature r is obtained:

$$\int \frac{E}{r} z^2 \, dA = \frac{E I_y}{r} = M \tag{2.3}$$

in which $I_y = \int z^2 \, dA$ is the moment of inertia of the cross section with respect to the neutral axis y.

In order to derive an expression for the relation between the curvature and the shape of the curve, we know from basic mathematics that the curvature radius r of an arbitrary function y = f(x) at point x in a cartesian coordinate system is given by [77]

$$r = \frac{\left[1 + (f'(x))^2\right]^{3/2}}{f''(x)} \tag{2.4}$$

where the prime indicates the derivative of f with respect to x.

However, in practical applications only very small deflections of beams are allowable and the deflection curves z(x) are very flat. Thus the first derivative of the curve's shape is nearly zero and we assume with sufficient accuracy (an angle of 2° results in a 0.2% error of the radius) that

$$z'(x) = 0 \tag{2.5}$$

where z(x) is the shape of the curve. With the coordinate system given in Fig. 2.3 and using eq. 2.4 and 2.5 the curvature radius and the shape of the curve are related by

$$\frac{1}{r} = -\frac{d^2z}{dx^2} \tag{2.6}$$

Equation 2.3 thus becomes

$$E I_y \frac{d^2z}{dx^2} = -M \tag{2.7}$$

Regarding the bending moments (Fig. 2.5), it can be seen from the equilibrium of the element that they are not equal at two adjacent cross sections and that the increase dM in the bending moment equals the moment of the couple represented by the two equal and opposite forces F, i.e.,

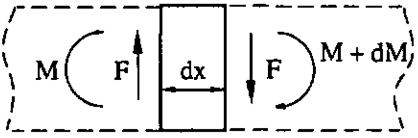

Fig. 2.5 Bending moments

$$dM = F\,dx \tag{2.8}$$

Using the Newtonian law, the differential equation of the deflection of the beam w(x,t) becomes

$$\mu(x)\,dx\,\frac{d^2w}{dt^2} = p(x,t)\,dx + dF \tag{2.9}$$

where p(x,t) is the force per unit length as a function of position and time and $\mu(x)$ is the mass per unit length.
Using the density ρ and the cross sectional area A(x), $\mu(x)$ equals ρ A(x). Thus according to eqs. 2.7 and 2.8 we transform eq. 2.9 into

$$\frac{d^2}{dx^2}\left(E\,I_y(x)\,\frac{d^2w}{dx^2}\right) = p(x,t) - \rho\,A(x)\,\frac{d^2w}{dt^2} \tag{2.10}$$

Thus, for a beam with constant cross section A and no applied force p(x,t), we obtain :

$$E\,I_y\,\frac{d^4w}{dx^4} = -\,\rho\,A\,\frac{d^2w}{dt^2} = -\,\mu(x)\,\frac{d^2w}{dt^2} \tag{2.11}$$

The separation of the deflection function in two distinct functions of space and time w(x,t) = z(x) u(t) results in

$$\frac{\ddot{u}(t)}{u(t)} = -\,\frac{E\,I_y\,z^{(4)}(x)}{\mu\,z(x)} = -\,\omega^2 \tag{2.12}$$

or:

$$\ddot{u}(t) + \omega^2\,u(t) = 0 \tag{2.13}$$

$$z^{(4)}(x) - \frac{\mu\,\omega^2}{E\,I_y}\,z(x) = z^{(4)}(x) - \frac{\lambda^4}{L^4}\,z(x) = 0 \tag{2.14}$$

where $\lambda^4 = \frac{\mu \, \omega^2}{E \, I_y} L^4$.

The general solutions of eqs. 2.13 and 2.14 are

$$u(t) = A \cos(\omega t) + B \sin(\omega t) \tag{2.15}$$

and

$$z(x) = C_1 \cos \frac{\lambda}{L} x + C_2 \sin \frac{\lambda}{L} x + C_3 \cosh \frac{\lambda}{L} x + C_4 \sinh \frac{\lambda}{L} x \tag{2.16}$$

The eigenvalues λ and thus the resonance frequencies as well as the C_i of the space solution are determined by the boundary conditions.

2.3.3 Formulae for the Bridge-Type Accelerometer

a) Calculation of the static deflection and stress distribution

In order to develop the formulae for the bridge-type accelerometer, the structure, schematically drawn in Fig. 2.6, will be reduced to a beam under load with well defined boundary conditions. Under an acceleration a in the z-direction, a force F acting on the silicon mass will lead to a deflection of the beams. Thus the seismic mass under acceleration can be substituted by a force of magnitude mass times acceleration. Since for most mass-beam configurations the beams' mass is smaller than 0.1% of the silicon mass, their reaction force due to any acceleration becomes negligible. Furthermore, the frame of the sensor chip is considered to be rigid. This implies for the reduced model both ends to be clamped i.e. they can not move in any direction and they end horizontally. Consequently the system of forces and moments shown in Fig. 2.7 has to act on the massless beam in order to be equivalent to a bridge-type sensor chip under acceleration.

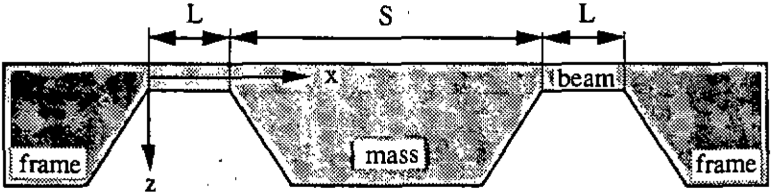

Fig. 2.6 Cross section of a bridge-type accelerometer

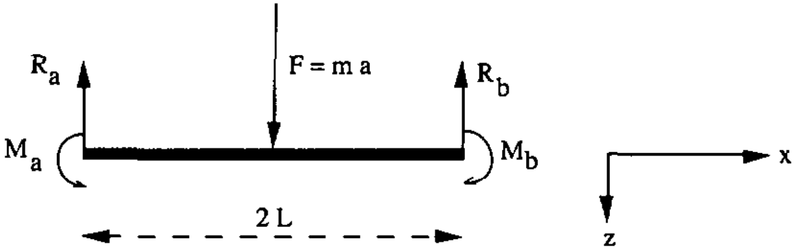

Fig. 2.7 Equivalent model of a bridge-type accelerometer

From equilibrium it follows that

$$M_a = M_b = M \tag{2.17}$$

$$R_a = R_b = R \tag{2.18}$$

$$R_a + R_b = F \tag{2.19}$$

The moment M to keep the beam of length 2L under a single concentrated load F at both ends horizontal is calculated in [78] and is

$$M = -\frac{F\,L}{4} \tag{2.20}$$

Hence, for x < L and using eqs. 2.17 - 2.20

$$M(x) = -M - R\,x = \frac{F}{2}\left(\frac{L}{2} - x\right) \tag{2.21}$$

Double integration of eq. 2.21 in x, using eq. 2.7 and the boundary conditions $z'(0)=0$, $z(0)=0$, we obtain the deflection curve of the two beams of a bridge-type accelerometer for $x \le L$ as

$$z(x) = \frac{m\,a\,L^3}{24\,E\,I_y}\left\{3\left(\frac{x}{L}\right)^2 - 2\left(\frac{x}{L}\right)^3\right\} \tag{2.22}$$

Therefore the stress at the surface (z = T/2) of a beam can be calculated with eqs. 2.2, 2.3 and 2.21

$$\sigma_x(x) = \frac{M(x)}{I_y}\,z = \frac{T\,L}{8\,I_y}\,m\,a\left(1 - 2\left(\frac{x}{L}\right)\right) \tag{2.23}$$

b) Dynamic response of the bridge-type accelerometer

As mentioned above, the resonance frequency can be determined out of eq. 2.16 using the boundary conditions. The bridge-type accelerometer has to fulfil the following boundary conditions

$$z(0) = 0 \tag{2.24}$$

$$\frac{dz}{dx}(0) = 0 \tag{2.25}$$

$$\frac{dz}{dx}(L) = 0 \tag{2.26}$$

$$E\, I_y \frac{d^3w(x,t)}{dx^3}(x{=}L) = \frac{m}{2}\frac{d^2w(x,t)}{dt^2}(x = L) \quad \text{(Newtonian law)} \tag{2.27}$$

Then we obtain for λ and the C_i terms of eq. 2.16

$$C_1 + C_3 = 0 \tag{2.28}$$

$$C_2 + C_4 = 0 \tag{2.29}$$

$$-C_1 \frac{\lambda}{L} \sin\lambda + C_2 \frac{\lambda}{L} \cos\lambda - C_3 \frac{\lambda}{L} \sinh\lambda + C_4 \frac{\lambda}{L} \cosh\lambda = 0 \tag{2.30}$$

$$\begin{aligned} &E\, I_y \frac{\lambda^3}{L^3}\left(C_1 \sin\lambda - C_2 \cos\lambda + C_3 \sinh\lambda + C_4 \cosh\lambda\right) = \\ &-\frac{m}{2}\omega^2\left(C_1 \cos\lambda + C_2 \sin\lambda + C_3 \cosh\lambda + C_4 \sinh\lambda\right) \end{aligned} \tag{2.31}$$

Solving this system of 4 equations for the 4 unknown C_i terms leads to one equation for λ, which has to be satisfied for any C_i

$$\frac{\mu L}{m} = \frac{\lambda}{2}\, \frac{1 - \cos\lambda\, \cosh\lambda}{\cos\lambda\, \sinh\lambda + \sin\lambda\, \cosh\lambda} \tag{2.32}$$

Figure 2.8 shows the graph of eq. 2.32 for different mass ratios. As can be seen for high ratios of $m/\mu L$, λ becomes $\ll 1$. As the mass of the beams is much smaller than the seismic mass, eq. 2.32 can be expanded as a series until the 5th order of λ.

$$\cos\lambda \cosh\lambda = 1 - \frac{\lambda^4}{6} + O(\lambda^6) \tag{2.33}$$

$$\cos\lambda \sinh\lambda = \lambda - \frac{\lambda^3}{6} + O(\lambda^5) \tag{2.34}$$

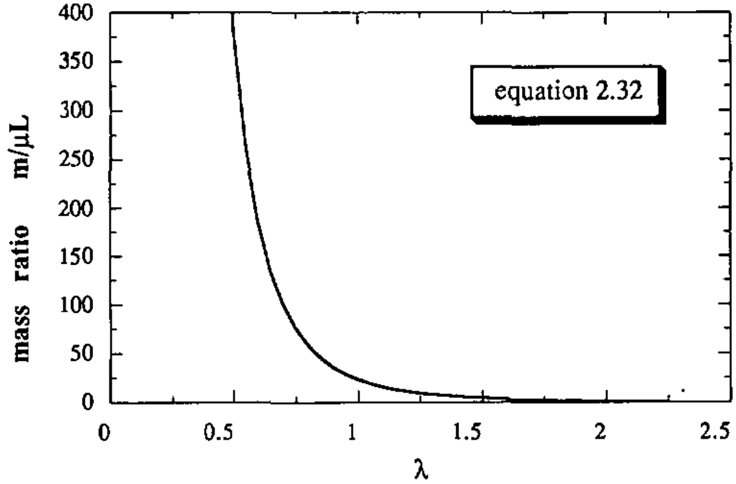

Fig. 2.8 λ in function of different mass ratios (see eq. 2.32)

$$\cosh\lambda \, \sin\lambda = \lambda + \frac{\lambda^3}{6} + O(\lambda^5) \tag{2.35}$$

With eqs. 2.33 - 2.35 in eq. 2.32 we obtain for the first resonance frequency :

$$\lambda^4 = \frac{24 \, \mu \, L}{m} \tag{2.36}$$

Thus using eq. 2.14
$$\omega_o = \sqrt{\frac{24 \, E \, I_y}{m \, L^3}} \tag{2.37}$$

The formula for the first resonance frequency can also be obtained in the following way. The mass-beam system of the bridge-type accelerometer corresponds to a spring mass system, which has its first resonance at

$$\omega = \sqrt{\frac{k}{m}} \tag{2.38}$$

The spring constant k is given by the deflection curve of the beam (eq. 2.22) and thus we have

$$F = k \;\; z(L) = m \;\; a \tag{2.39}$$

This also leads to eq. 2.37.

Table 2.I Analytical formulae for the bridge-type accelerometer

Beam deflection	$z(x) = \frac{m\,a\,L^3}{12\,n\,E\,I_y}\left(3\left(\frac{x}{L}\right)^2 - 2\left(\frac{x}{L}\right)^3\right)$	for $x \le L$	(2.40)
Stress at surface	$\sigma_x(x) = \frac{T\,L}{4\,n\,I_y}\,m\,a\left(1 - 2\left(\frac{x}{L}\right)\right)$	$\propto \frac{L\,S^2}{W\,T^2}$	(2.41)
Resonance frequency	$\omega_0 = \sqrt{\frac{12\,n\,E\,I_y}{m\,L^3}}$	$\propto \frac{\sqrt{W}\,T^{3/2}}{S\,L^{3/2}}$	(2.42)

L = beam length, T = beam thickness, W = beam width, $I_y = \frac{1}{12} W T^3$ = moment of inertia, n = number of beams ($n \ge 2$), a = acceleration, m = seismic mass, x = coordinate along beam axis x with origin at frame end, S = length of the quadratic seismic mass at the surface

All the basic formulae of the bridge-type accelerometer are summarized in Table 2.I and correspond to the literature formulae [72, 79]. The sensitivity can be calculated by the multiplication of the mean stress within the piezoresistors with the piezoresistive coefficients in that crystallographic direction (see section 1.5). Calculated data of fabricated devices are given in Table 5.II.

2.3.4 Formulae for the Cantilever-Type Accelerometer

a) Calculation of the static deflection and stress distribution

The development of analytical formulae for a cantilever-type accelerometer is similar to that for the bridge-type accelerometer given above. Again the structure, schematically drawn in Fig. 2.9, will be replaced by a massless beam with well defined boundary conditions (Fig. 2.10). The silicon mass under acceleration in the z-direction is substituted by a force of magnitude mass times acceleration. Since the silicon mass is suspended from only one side, one beam's end of the equivalent model is free and the other one is clamped, e.g. it can not move in any direction and it ends horizontally. This condition requires a moment and a force on that end. Therefore the system of forces and moments acting on a massless beam as shown in Fig. 2.10 is equivalent to a cantilever-type sensor chip under acceleration. From the equilibrium it follows that

$$R_a = m\,a \qquad (2.43)$$

$$M_a = m\,a\left(L + \frac{S}{2}\right) \qquad (2.44)$$

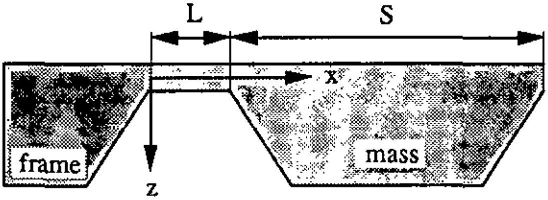

Fig. 2.9 Cross section of a cantilever-type accelerometer

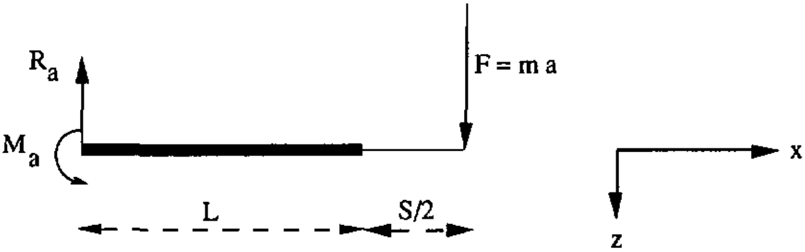

Fig. 2.10 Equivalent model of a bridge-type accelerometer

Using eqs. 2.43 and 2.44 the momentum for $x \leq L$ becomes

$$M(x) = m\,a\left(L + \frac{S}{2}\right) - m\,a\,x \tag{2.45}$$

Double integration of x, using eq. 2.7 and the boundary conditions $z(x{=}0) = 0$, $z'(x{=}0) = 0$ we find

$$z(x) = \frac{m\,a}{2\,E\,I_y}\,x^2\left(\left(L + \frac{S}{2}\right) - \frac{1}{3}\,x\right) \qquad \text{for } x \leq L \tag{2.46}$$

Because the seismic mass will never bend, the deflection curve for $L \leq x \leq L + S$ is

$$z(x) = z(L) + \frac{dz}{dx}(x{=}L)\,(x - L) \qquad \text{for } L \leq x \leq L + S \tag{2.47}$$

Therefore using eqs. 2.2, 2.3 and 2.44 the stress at the surface ($z = T/2$) of the beam will be

$$\sigma_x(x) = \frac{M(x)}{I_y}\,z = \frac{m\,a\,T}{2\;I_y}\left(\left(L + \frac{S}{2}\right) - x\right) \qquad \text{for } x \leq L \tag{2.48}$$

b) Calculation of the resonance frequency

We will use the Rayleigh principle [80] for an analytical solution, where the frequency of vibration will be found from using the principle of the conservation of energy in the system. As the mass of the spring is small in comparison to the mass of the load, the mode of vibration will not be substantially affected by the mass of the spring (useful approximation for arbitrarily formed structures).
Using eq. 2.13 and the Rayleigh principle which equates the maximum kinetic energy and the maximum potential energy, we obtain for the cantilever-type accelerometer :

$$K_{max} = \frac{1}{2} \int \left(\frac{dw}{dt}\right)^2 dm = \frac{1}{2}\,\omega^2\,u(t)^2 \int_0^{L+S} z^2\,dm \qquad (2.49)$$

$$U_{max} = \frac{I}{2} \int_0^{L+S} E\,I_y \left(\frac{d^2w}{dx^2}\right)^2 dx = \frac{1}{2}\,u(t)^2 \int_0^{L+S} E\,I_y \left(\frac{d^2z}{dx^2}\right)^2 dx \qquad (2.50)$$

For the calculation of the maximum kinetic energy, the kinetic energy of the beam can be neglected. Thus we find

$$K_{max} \sim \frac{1}{2}\,\omega^2\,u(t)^2 \int_L^{L+S} z^2\,dm = \ldots = \qquad (2.51)$$

$$= \frac{1}{2}\,\omega^2\,u(t)^2\,m \left(\frac{m\,a}{E\,I_y}\right)^2 \left\{\frac{1}{9}L^6 + \frac{1}{3}S\,L^5 + \frac{21}{48}S^2L^4 + \frac{7}{24}S^3L^3 + \frac{1}{12}S^4L^2\right\}$$

$$U_{max} = u(t)^2\,\frac{1}{6}\,\frac{m^2\,a^2}{E\,I_y}\left\{L^3 + 3\,L\,\frac{S^2}{4} + 3\,L^2\,\frac{S}{2}\right\} \qquad (2.52)$$

Equating eqs. 2.51 and 2.52 (Rayleigh principle) we obtain for the first resonance frequency

$$\omega^2 = \frac{E\,I_y}{m\,L^3}\;\frac{4 + 6\left(\frac{S}{L}\right) + 3\left(\frac{S}{L}\right)^2}{\frac{4}{3} + 4\left(\frac{S}{L}\right) + \frac{21}{4}\left(\frac{S}{L}\right)^2 + \frac{7}{2}\left(\frac{S}{L}\right)^3 + \left(\frac{S}{L}\right)^4} \qquad (2.53)$$

c) Calculation of the resonance frequency, without neglecting the mass of the beams [81]

The efficiency of the Rayleigh method becomes obvious, if the exact solution is obtained using eq. 2.16. In this case the mass of the beams is not neglected. Three of the four boundary conditions for the cantilever-type accelerometer remain the same as for the bridge-type accelerometer (eqs. 2.24, 2.25 and 2.27), except for eq. 2.26 we have

$$E\, I_y \left(\frac{d^2 z(x)}{dx^2}\right)(x=L) = \Theta\, \omega^2 \left(\frac{dz}{dx}\right)(x=L) \qquad (2.54)$$

where Θ is the moment of inertia of the mass m with respect to the axis z. Introducing the general solution (eq. 2.16) into eq. 2.54 and with eqs. 2.28, 2.29 and 2.31 we get a system for the four unknown C_i, which finally leads to the following transcendental equation for λ

$$\frac{1+\alpha\beta\lambda^4}{\cos\lambda\ \cosh\lambda} + \left(1-\alpha\beta\lambda^4\right) + \lambda\left(\alpha-\beta\lambda^2\right)\tanh\lambda\ - \lambda\left(\alpha+\beta\lambda^2\right)\tan\lambda = 0 \qquad (2.55)$$

where $\alpha = \frac{m}{\mu\ L}$, $\beta = \frac{\Theta}{L3\ \mu}$ are dimensionless parameters. With eq. 2.14 and a solution λ of eq. 2.55, the resonance frequency can be calculated.

All basic formulae of the cantilever type accelerometer are summarized in Table 2.II and correspond to already published formulae [72, 79]. The sensitivity is given by multiplying the mean stress sensed by a piezoresistor with the piezoresistive coefficients (see section 1.5). Calculated data of fabricated devices are listed in Table 4.1 of chapter 4.

Table 2.II Analytical formulae for the cantilever-type accelerometer

Beam deflection	$z(x) = \frac{m\,a}{2\,E\,I_y}\,x^2 \left\{\left(L+\frac{S}{2}\right) - \frac{1}{3}\,x\right\}$	for $x \le L$	(2.56)
Stress at surface	$\sigma_x(x) = \frac{m\,a\,T}{2\,I_y} \left\{\left(L+\frac{S}{2}\right) - x\right\}$		(2.57)
Resonance frequency	$\omega_o = \sqrt{\frac{E\,I_y}{m\,L^3}\ \frac{4+6\left(\frac{S}{L}\right)+3\left(\frac{S}{L}\right)^2}{\frac{4}{3}+4\left(\frac{S}{L}\right)+\frac{21}{4}\left(\frac{S}{L}\right)^2+\frac{7}{2}\left(\frac{S}{L}\right)^3+\left(\frac{S}{L}\right)^4}}$		(2.58)

L = beam length, T = beam thickness, W = beam width, $I_y = \frac{1}{12}\,W\,T^3$ = moment of inertia, n = number of beams (n ≥ 2), a = acceleration, m = seismic mass, x = coordinate along beam axis x with origin at frame end, S = length of the quadratic seismic mass at the surface

2.3.5 Design Considerations

Every accelerometer design aims at a high sensitivity and high resonance frequency. But as can be seen from the analytical formulae, there is a trade-off between the sensitivity and the resonance frequency [71]. Increased sensitivity implies lowered resonance frequency and vice versa. Thus every accelerometer should be optimized in regard to its application. In the design phase a first estimate of the performance can be made using classical formulae.

Since optimization work on cantilever-type accelerometers has already been published in the literature [71], all the following calculations apply to four-beam bridge-type accelerometers having a quadratic seismic mass. As arbitrarily formed beams require finite element modeling, we assume straight beams in order to use the formulae of subsection 2.3.3. Furthermore we define the overall chip size C as the sum of the side length S of the (quadratic) mass and twice the beam length L.

Figure 2.11 shows the calculated sensitivity and resonance frequency in function of the beam length L for a fixed chip size of 3 mm. It can be seen that the maximum sensitivity is reached for a beam length of about 500 μm. Some dimensions of the design are constrained by the choice of the process technology. In addition the length of the piezoresistors also influences the dependence of the sensitivity on the beam length. Calculations have shown that for a device having a beam thickness of 12 μm (given by the epitaxial layer

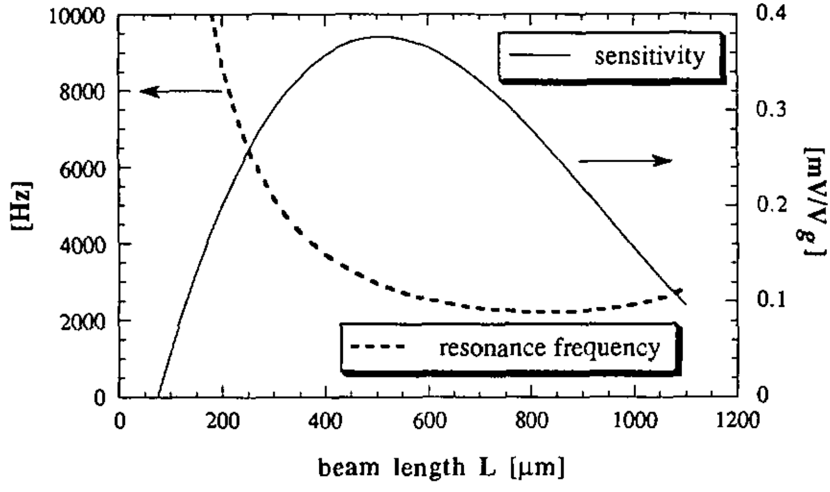

Fig. 2.11 Sensitivity and resonance frequency of a bridge-type accelerometer as a function of the beam's length for a constant overall size (3000 μm), width (100 μm), thickness (12 μm), number of beams (4) and piezoresistor length (75 μm), calculated using analytical formulae

thickness) and a beam width of 100 μm (= minimum size needed for the chosen dimensions of the piezoresistor) the resonance frequency becomes greater than 900 Hz for any beam length (assuming a wafer thickness of 380 μm). As for many applications the needed frequency range is below 1 kHz, we will develop a formula for the beam length which maximizes the sensitivity of a four-beam bridge-type accelerometer taking into account all the technological restrictions and the dimensions of the piezoresistors.

Since we have been using an industrial bipolar compatible process [82, 83] and an electrochemical etch-stop technique, the thickness of the beams is given by the epitaxial layer thickness. The detailed description of the industrial fabrication process is given in section 3.4. Equations 2.41 and 2.57 (Tables 2.I and 2.II) show that for high sensitivity the beam width has to be as small as possible [84]. Moreover, its minimal size is given by the lateral dimensions of the piezoresistors. Since the price of a silicon accelerometer is directly related to its size, we will consider the overall size C (sum of side length of the mass and twice the beam length) as a constant design parameter. Therefore the only free parameter of a quadratic accelerometer design remains the length of the beams.

With this in mind, we first calculate the average stress σ_{av} sensed by a piezoresistor of length P and junction depth D integrated into a beam of thickness T (see Fig. 2.12). We assume for all resistors that one end is positioned exactly at the connection of the beam with the frame (Fig. 2.12) or

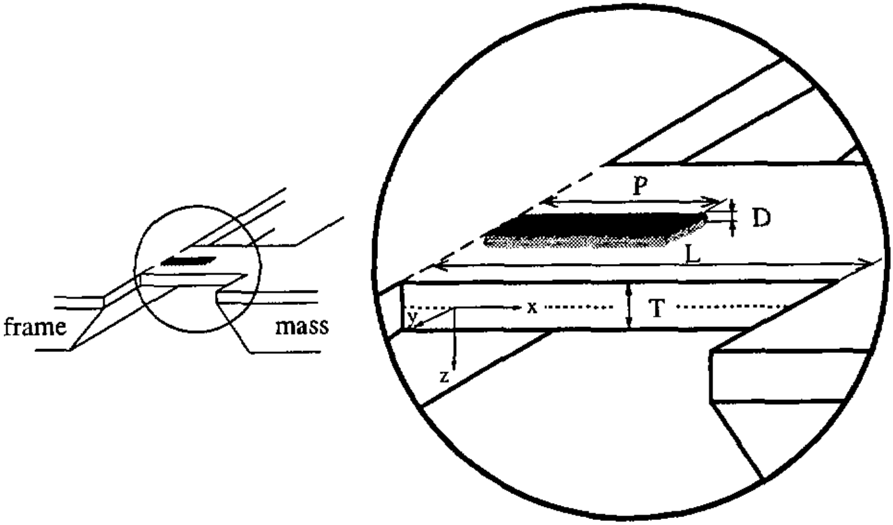

Fig. 2.12 Location and dimensions of the piezoresistors

with the mass, that is, where the maximal stress σ_{max} at the surface occurs. We see from eqs. 2.40 and 2.41 that the stress in the beam depends linearly upon x and z. Thus, we obtain for the average stress

$$\sigma_{av} = \sigma_{max}\left(1 - \frac{D}{T}\right)\left(1 - \frac{P}{L}\right) \tag{2.59}$$

with L = length of the beam and σ_{max} = maximal stress at the surface at each end of the beam.

Assuming an uniform doping of all piezoresistors (a good approximation for implanted resistors), the piezoresistance coefficients are constant. Therefore the sensitivity S_0 of a bridge-type accelerometer is proportional to the average stress σ_{av} sensed by the piezoresistor (eqs. 2.41 and 2.59) :

$$S_0 \propto \frac{L\,m}{W\,T^2}\left(1 - \frac{D}{T}\right)\left(1 - \frac{P}{L}\right) \tag{2.60}$$

where m = seismic mass, W = width of the beam.

Since the width W of the beam is given by the minimal lateral dimensions of the piezoresistor, and since the thickness T of the beams and the junction depth D of the resistor are defined by the chosen process technology, we consider them to be constants and we get

$$S_0 \propto L\,m\left(1 - \frac{P}{L}\right) \tag{2.61}$$

The mass is proportional to the volume of the mesa like form etched by KOH. The volume of a truncated pyramid with top and bottom surfaces F and G, and height h, is given by

$$V_{Pyramid} = \frac{h}{3}\left(F + \sqrt{F\,G} + G\right) \tag{2.62}$$

As explained above, we consider the overall size (sum of the side length S of the mass and twice the beam length L) to be a constant, i. e., 2L + S = C with C = constant. Thus, we can replace the sidelength S of the mass by a function of L, i.e. C - 2L. Therefore eq. 2.61 becomes, using eq. 2.62,

$$S_0 \propto L^3 + L^2\left(\frac{\sqrt{2}}{2}H - (P + C)\right) + \frac{1}{12}L\left(3\,C^2 + 2H^2 + 12CP - 3\sqrt{2}H(C + 2P)\right) + O\left(L^0\right) \tag{2.63}$$

where H is the wafer thickness. Since we look for the maximum sensitivity for a given overall size, the derivation of S_0 to L has to be 0. Thus, eq. 2.63 leads to a quadratic equation in L, which has the following solutions:

$$L = \frac{1}{6}\left\{\left(2\,(C + P) - \sqrt{2}H\right) \pm \sqrt{(C - 2P)^2 - \sqrt{2}\,H\,(C - 2P)}\right\} \qquad (2.64)$$

We see in Fig. 2.11, that for a constant overall size C, the sensitivity S_o reaches its maximum at the length of the beam of 507 μm, the same value as would be obtained using eq. 2.64. Assuming homogeneous doped piezoresistors the sensitivity S_σ was calculated by multiplying the averaged stress σ_{av} with the longitudinal piezoresistance coefficient ($\pi_l = 72\ 10^{-11}\ \mathrm{Pa}^{-1}$ for p-type, 7.8 Ωcm and (001) orientated silicon for [110] direction at room temperature), since the relative change of one piezoresistor corresponds to the output's change of an ideally balanced Wheatstone bridge configuration (for details see section 1.5 and subsection 3.4.2).

Figure 2.13 shows the maximum possible sensitivity and the corresponding resonance frequency as a function of the overall size C. It can be seen that with increasing chip size the maximum sensitivity increases and the resonance frequency decreases, but is still greater than 1 kHz for an overall size of 3 mm.

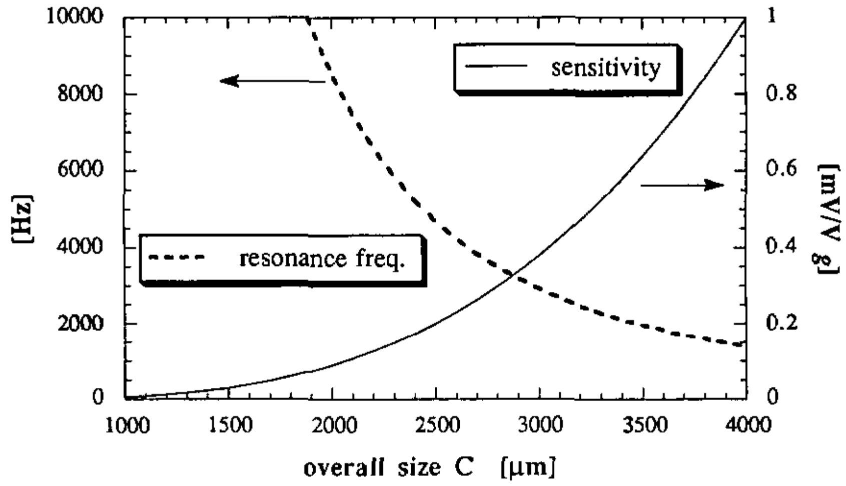

Fig. 2.13 Maximized sensitivity and its corresponding resonance frequency of a four-beam bridge-type accelerometer in function of overall size, calculated by analytical formulae (thickness and width of the beam 12 μm and 100 μm, respectively)

2.3.6 Limits of Analytical Formulae

To use an analytical approach, the structure has to be simplified to a system of forces, moments and shapes in such a way that while still fitting to reality it consists of basic, analytically solvable subsystems. In the case of accelerometers the analytical description is insufficient or almost unsolvable in the four important situations described below.

- So far we have reduced the frame - beam - mass system forming the sensitive part of the accelerometer to a simple beam under a concentrated load, either with both ends clamped (bridge-type) or with only one end clamped (cantilever-type). As only the base of the frame of the sensitive device is glued on a substrate for the characterization, the extremities of the beams are therefore not rigidly clamped to the frame. The influence of this feature on the response of the real system cannot be predicted using analytical formulae. However, the detailed stress distribution at the interface of the beam and the frame is of great interest in order to find the optimal position of the piezoresistors.
- It is difficult to predict the higher modes of vibration and their corresponding resonance frequencies by using analytical methods. These data are a criterion to estimate the mechanical cross-axis sensitivity.
- Passivation layers and temperature effects induce stresses, and it is nearly impossible to model the influence of a prestressed frame by analytical calculations. But such stresses can affect the temperature dependence of sensitivity and resonance frequency.
- Static and dynamic calculations for specially shaped beams, e.g., U - or L - like, are extremely difficult. Arbitrarily formed beams have a potential of higher sensitivity for the same chip size [37].

However, using Finite Element Modeling (FEM) these problems as well as any non-linear effects can be treated and analyzed.

2.4 FINITE ELEMENT MODELING (FEM)

2.4.1 Introduction

Finite element modeling (FEM) is a powerful tool for the simulation of micromechanical structures [68 - 70] since it does not have the limitations of the analytical formulae listed above. FEM is a standard numerical modeling technique extensively used in the engineering field for structural and component design. The application of this method to sensor and microstructure design is becoming a standard tool in the sensor industry.

The work described in this thesis was performed using the university version of the commercially available finite element program ANSYS® from Swanson Analysis Systems Inc. The only restriction of this version is its limitation to a wavefront of 500. The number of equations which are active after any element has been processed during the solution procedure is called the wavefront at a given point. This program was run on a Apollo D3500 workstation utilizing a 360 MB hard disk.

The technique of submodeling was used to achieve refined accuracy for small features within the region of interest of a FEM model, as well as keeping the wavefront small (< 500). In this technique the displacements resulting from a coarsely meshed model are used as boundary conditions for the submodel, which is cut out of the original structure. The lower drawing in Fig. 2.15 is a finely meshed submodel of the coarse model. These submodels can be built closer and closer to the region of interest. This iterative method can be applied as often as required to smaller regions and finer models, until the desired mesh refinement is achieved.

Most sensors have several axes of symmetry. Using symmetrical boundary conditions reduces the model size. However, for a modal analysis, as well as for the simulation of a transverse acceleration where asymmetrical behaviour is expected, the complete sensor structure has to be used for the calculations.

Since an accelerometer can not be reduced to a two-dimensional model, it has to be simulated with 3D elements. We used stif45 elements, which are three-dimensional isoparametric solid elements with 8 nodes and three degrees of freedom at each node. In spite of the possibility of submodeling, the meshing of an accelerometer with regard to our restricted wavefront is not easy. For a stress calculation, the region of interest consists of one half of the beam and of a very small part of the frame to which the beam is connected. As the volume of interest is only 1/1000 of the volume of the complete structure, we tried to mesh the beam as finely as possible and the seismic mass in a very coarse manner, trying to avoid creation of brick elements with a bad sidelength ratio and to keep the angle of the bricks always between 90° ± 45°. Finally, we had about 1000 elements for the coarse model and about 2700 elements for the submodel.

We have observed that the refinement of the meshing as much as the manner of meshing (equidistant or variable length of elements) influences the calculated, detailed stress distribution up to 10 %. This shows that the meshing has to be done very carefully. The amount of solution error that is due to poor mesh discretization was approximated by the energy error. The energy error which is similar in concept to the strain energy, represents the error associated with the discrepancy between the averaged and unaveraged stresses. This discrepancy is due to the assumption that only the displacements are continuous at the nodes. Though the stresses are calculated from the displacements and should also be continuous, they generally are not. Although the value of the percentage energy error which can be considered to be "significant" is

problem dependent, this parameter helped to judge the mesh quality.
Furthermore, it is difficult to estimate the boundary conditions which are closest to reality. As the beams of the first series of the accelerometer's second prototype were not covered with any passivation layer, FEM analysis was performed on a pure silicon structure.

2.4.2 Modal Analysis

Figure 2.14 shows the first three modes of vibration of a four-beam bridge-type accelerometer, whose dimensions are given in the figure caption. The corresponding resonance frequencies are 2760 Hz, 4430 Hz and 5700 Hz and thus, their ratio becomes 1:1.6:2.1. The first mode corresponds to the fundamental mode of motion in the vertical acceleration axis, whereas at the next highest modes the seismic mass rotates around the x and y axis, respectively. In comparison to the work of Moser et al. [85], these asymmetric modes occur at much lower frequencies than the second symmetric mode. The frequency of the second mode (rotation around x) depends on the effective spacing between the two beams on each side of the four-beam bridge-type accelerometer. As the separation increases, the resonance frequency rises and this mode is harder to initiate, which is desirable. The totally opposite case occurs when the two beams are completely brought together. This is the case of the two-beam bridge-type accelerometer (see subsection 3.4.1), with the resonance frequency of the second mode (560 Hz) below that of the vertical displacement mode (2470 Hz).

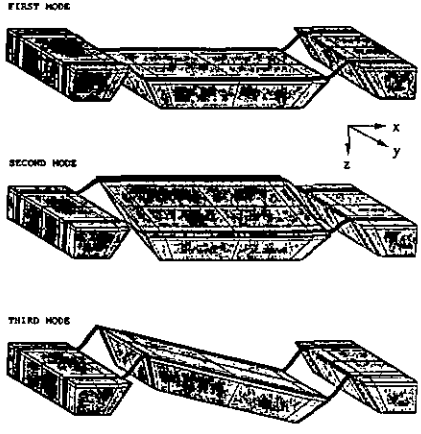

Fig. 2.14 First three modes of a four-beam bridge-type accelerometer (Beam length 300 μm, width 100 μm, thickness 8.5 μm, mass 2400 μm)

Due to the mass' suspension of a cantilever-type accelerometer, the seismic mass moves on an arc in the first mode of vibration. In the second and third mode, we notice rocking around one of its longitudinal axes as well.

2.4.3 Static Analysis

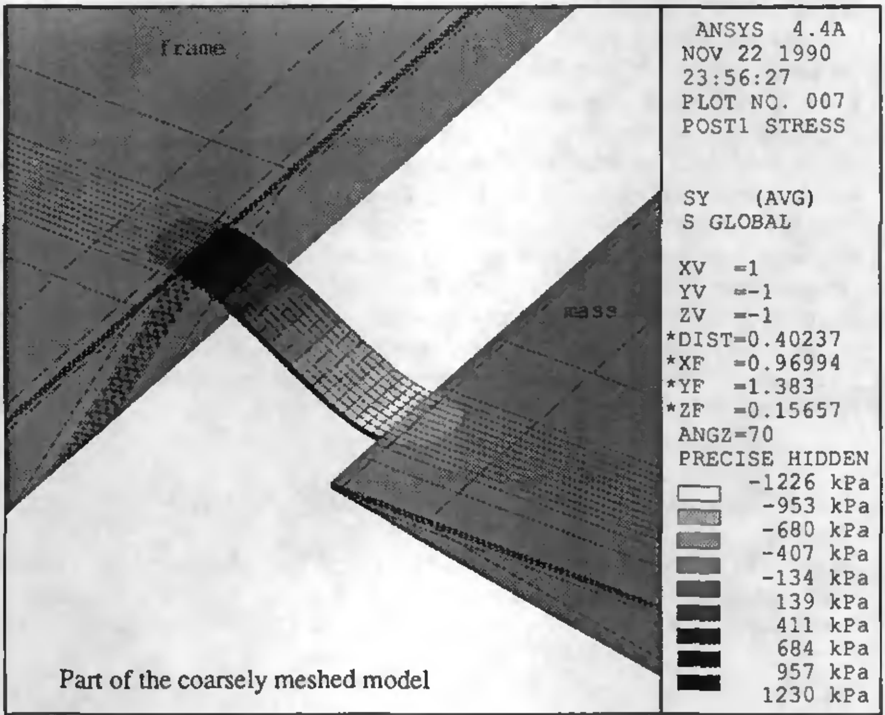

Part of the coarsely meshed model

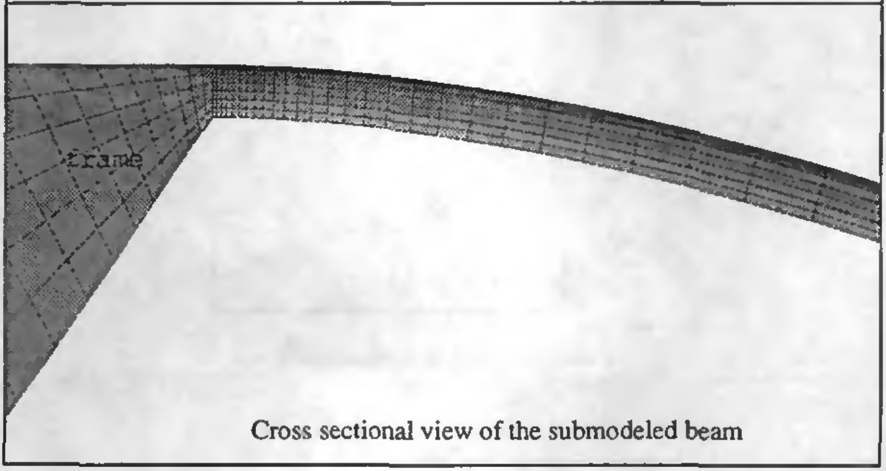

Cross sectional view of the submodeled beam

Fig. 2.15 Part of a coarsely meshed accelerometer and cross sectional view of the submodeled part of a beam; the accelerometer is exposed to an acceleration of 1 *g* in the vertical axis.

For these simulations the base of the accelerometer's frame was fixed. The technique of submodeling was applied to obtain details of the peak stress region at the beam-frame interface. Figure 2.15 shows in the upper part a coarsely meshed section of a four-beam bridge-type accelerometer exposed to an acceleration of 1 *g* in the vertical axis. It can be noticed that the highest positive and negative stresses occur near the extrema of the beam, where the piezoresistors will be implanted. The displacements calculated for the coarse model were used as boundary conditions for the finely meshed submodel, of which a cross section is shown in the lower part of Fig. 2.15. The optimal position of the piezoresistors is found, where the integration of stress over the length of a piezoresistor becomes a maximum. This results in positioning the piezoresistors at the extrema of the beams.

In contradiction to the bridge-type, the stress across the surface of the beam of a cantilever-type beam is nearly uniformly distributed. This implies piezoresistors should be aligned perpendicularly and longitudinally to form a full wheatstone bridge.

2.4.4 Comparison FEM to Analytical Formulae

In order to compare the results of the analytical formulae and finite element analysis we have calculated the performance of the sensitive devices using the same dimensions (given in the corresponding figure captions) for both types of

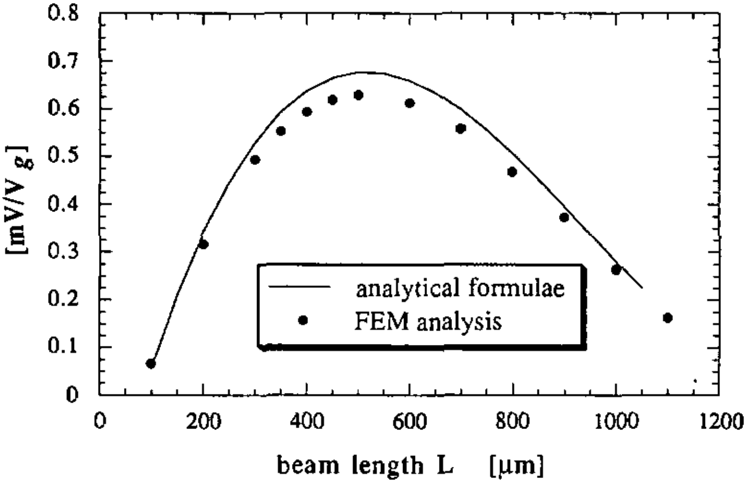

Fig. 2.16 Comparison of calculated sensitivity in function of the length of the beam using analytical formulae and FEM (width of the beams 100 μm, thickness of the beams 8.5 μm, overall size 3000 μm)

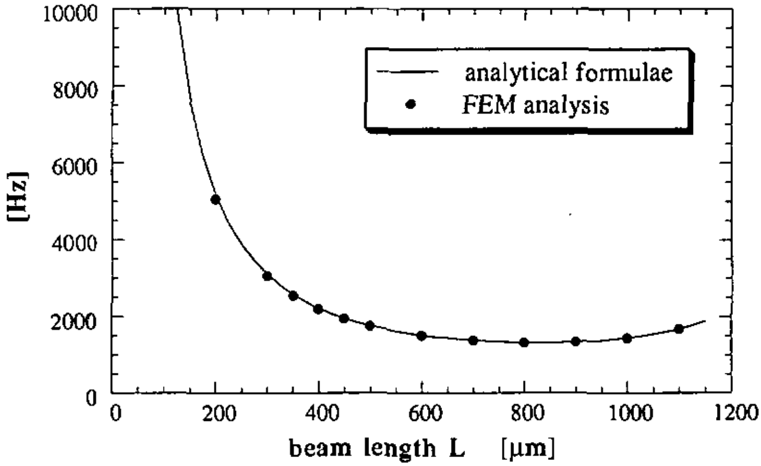

Fig. 2.17 *Comparison of calculated resonance frequency as a function of the length of the beam using analytical formulae and FEM (width of the beam 100 μm, thickness of the beam 8.5 μm, overall size 3000 μm)*

calculations. We assumed as a boundary condition for the finite element model, that only the base of the accelerometer's frame is fixed. Figure 2.16 shows the sensitivity as a function of the beam's length. The calculated values are about 10% higher than the FEM ones. But the dependence of the sensitivity on L at a constant overall size is in both cases similar. The maximum is reached at the same value of L for both methods. The resonance frequency as a function of the length of the beam can be seen in Fig. 2.17. Excellent agreement of both calculations can be observed.

2.5 CONCLUSIONS

We can distinguish mainly two mass-beam configurations, the bridge-type and the cantilever-type, respectively. For structures of both types having straight beams, analytical formulae are very powerful in order to see easily the dependence of sensitivity and resonance frequency on various design parameters. Many device dimensions are determined by the chosen bipolar compatible industrial fabrication process and by the lateral size of the piezoresistors. For a given chip size of a quadratic four-beam bridge-type accelerometer design, the only free device parameter remains the length of the beams. We developed a formula for the beam length which maximizes the sensitivity as a function of the overall chip size and of the physical dimensions of the piezoresistors.

Compared to the bridge-type, cantilever-type accelerometers are much more sensitive for the same beam length and mass. As the peak stress region in the cantilever is of the same sign and nearly the same size at the surface of the whole beam, very short beams are advantageous.

In FEM analysis, boundary conditions which correspond best to reality, as well as process related effects such as rounded corners, can be taken into account for the calculations. This allows a more detailed prediction of the characteristics of the device than by analytical formulae [70]. A further advantage of FEM analysis over analytical formulae is the ease in determining higher vibrational modes and their corresponding resonance frequencies which indicate the degree of the mechanical transverse sensitivity. Additionally, passivation layers, non-linear effects, arbitrarily formed beam structures and encapsulations can still be treated by FEM analysis [86], whereas their analytical description is very difficult without further simplifications and assumptions.

Pure silicon structures have been simulated. The predictions of both theoretical approaches agree within 10%. In section 4.4 these results will be compared to the performance of fabricated devices.

Chapter 3

Fabrication of the Sensor Chip

The fabrication of the first prototype revealed two steps to be crucial: the etching of the remaining membrane and the protection of the convex corners of the silicon mass against overetching. Since no layer was found that gave sufficient and reliable protection of the metallization against wet etchants, a plasma process for deep dry etching of silicon was developed. Using a photoresist mask and a chlorine/fluorine gas mixture vertical walls were etched. This contrasts with pure fluorine gas, which behaved as an isotropic etchant. The process parameters were optimized with regard to a good selectivity towards the masking material and a high etchrate (≈ 1 μm/min.). Different etch compensation structures for KOH etching were investigated. Finally the dimensions of the second prototype and the bipolar compatible process sequence are described. In addition, the possibility to electrically compensate the transverse sensitivity of a bridge-type accelerometer are discussed.
Parts of this chapter have been published in [87-89].

3.1 FIRST PROTOTYPE OF SENSITIVE ELEMENTS

Since the first prototype was intended only to test the feasibility of the system, the majority of the measurements and the encapsulation were made with the second prototype.

3.1.1 Objectives

First a process sequence for the fabrication of piezoresistive accelerometers was developed. In order to achieve compatibility to the existing industrial fabrication process for pressure sensors at ASCOM, Aluminum as metallization material and KOH as wet etchant for silicon were compulsory. As the first prototype was entirely fabricated in our small R&D laboratory with no implanter, the piezoresistors were diffused in spite of the known disadvantages of this over implanted ones. Furthermore we did not perform an electrochemical etch-stop on the first generation.

3.1.2 Fabrication Steps

The whole fabrication sequence is given in Table 3.I. Two process steps were crucial : the appropriate doping of the diffused piezoresistors and when the membrane between the rim and the seismic mass is etched through, the protection of the metallization (Al) against KOH.

The piezoresistors were diffused out of doped silicon dioxide layers (VAPOX). The process was simulated with SUPREM (Stanford University Process Engineering Models Program) which allowed the process parameters to give a resistivity of about 5 Ω/□ for the p^{++} regions and about 200 Ω/□ for the low doped p regions to be determined. Since these values are extrema for our installation, the uniformity was poor which lead to rather high offset

Table 3.I Fabrication sequence of the first prototype (IMT laboratory)

Step	Process
0	Silicon wafer : n - type, 3-5 Ωcm, double side polished, 3 inch
1	Wet oxidation, 1.5 μm
2	Deposition of low phosphorous doped VAPOX (channel stop)
3	Photolithography and oxide opening for p and p^{++} regions
4	Deposition of low boron doped VAPOX (after diffusion : 180 Ω/□, junction depth 1.0 μm)
5	Photolithography and oxide opening for p^{++} regions
6	Deposition of high boron doped VAPOX (after diffusion : 5.1 Ω/□, junction depth 2.9 μm)
7	Diffusion (1100° C, 10 min. N_2, 40 min. O_2)
8	Photolithography and contact openings
9	Aluminum evaporation
10	Photolithography and etching Al
11	Anneal (25 min., 450° C)
12	Deposition PECVD Si_xN_y (8000 Å)
13	Photolithography and opening of region between mass and rim
14	Photolithography on backside and opening of oxide
15	KOH etching from the backside down to double beam thickness (≈ 30 μm) (front side protected by means of a chuck)
16	KOH etching from both sides (60° C , 40 % = 10.61 moles/l)
17	Stripping of PECVD Si_xN_y in BHF

values.

During the etching of silicon from the back of the wafer, the front side is protected by means of a chuck. Unlike in case of pressure sensors,- the remaining membrane between the seismic mass and the rim must be etched. Therefore, the front side of the chip is exposed to the etchant. Using 40 weight percent KOH at 60° C and assuming a membrane thickness of 15 µm this etching step lasts about 1 hour. Since aluminum is etched by KOH within some seconds the metallization needs to be protected. No photosensitive organic layer was found to withstand the whole etch period. The same layers were also found to be inadequate as a protection of the metallization against the isotropic etchant (mixture of HNO_3 (65%), HF (50%) and CH_3COOH in the volume ratio of 3.5 : 1 : 1). Since aluminum is the interconnection material, the temperature of any subsequent process step can not exceed 450° C due to Al spike formation and diffusion at elevated temperatures [90]. Since silicon nitride is not etched in KOH, we used PECVD nitride (deposition temperature 350° C) as a protection layer. On a flat surface, SixNy withstands KOH without forming pinholes for more than 24 hours. For our application a nitride layer was deposited over the metal lines. The step coverage is excellent, but due to the roughness of the aluminum surface, some pinholes (1 on about 10 metallization lines) in the protection layer were observed (see Fig. 3.1). This lowered the yield enormously, because the underlying aluminum layer was immediately etched by KOH penetrating through the pinhole.

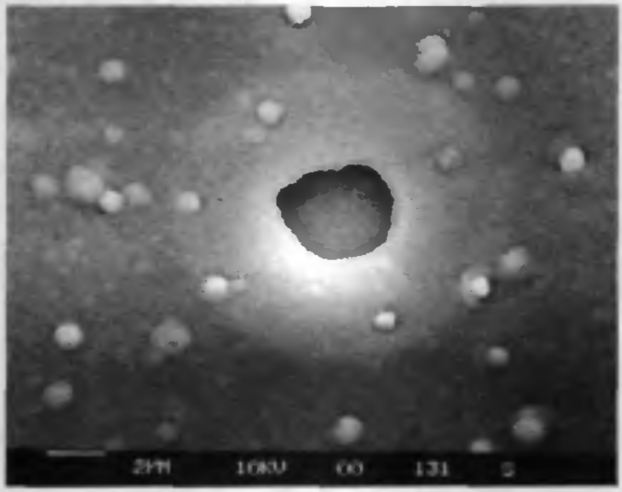

Fig. 3.1 Pinhole in the Si_xN_y layer covering Aluminum interconnections

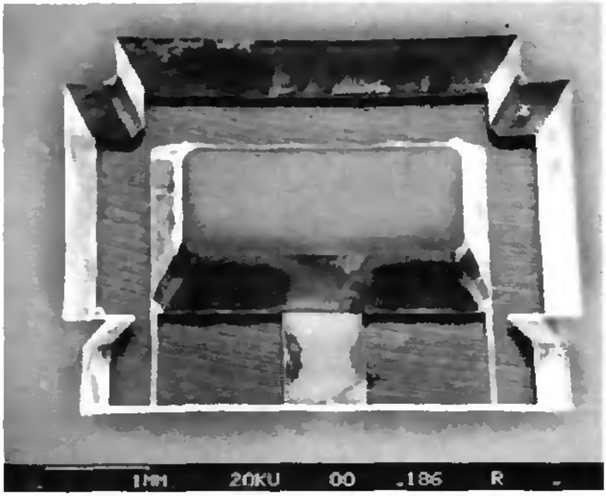

Fig. 3.2 View on the back of a cantilever-type accelerometer (first prototype)

3.1.3 Results

The back of a cantilever-type accelerometer produced as described above is shown in Fig. 3.2. Figure 3.3 shows the output of a two-beam bridge-type accelerometer in function of acceleration at different frequencies. The

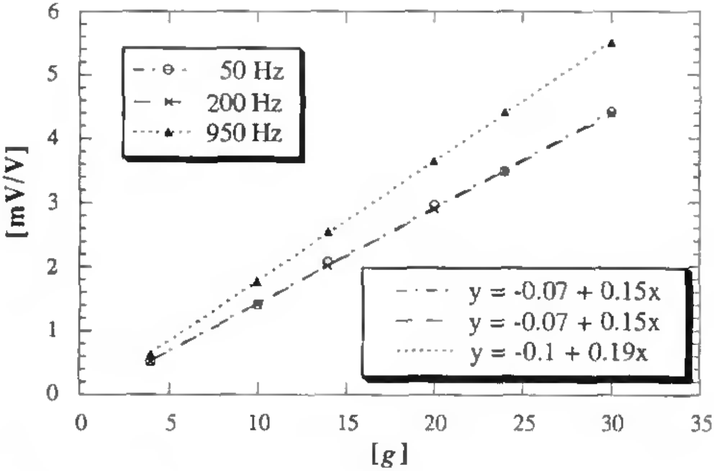

Fig. 3.3 Linearity of a two-beam bridge-type accelerometer (first prototype)

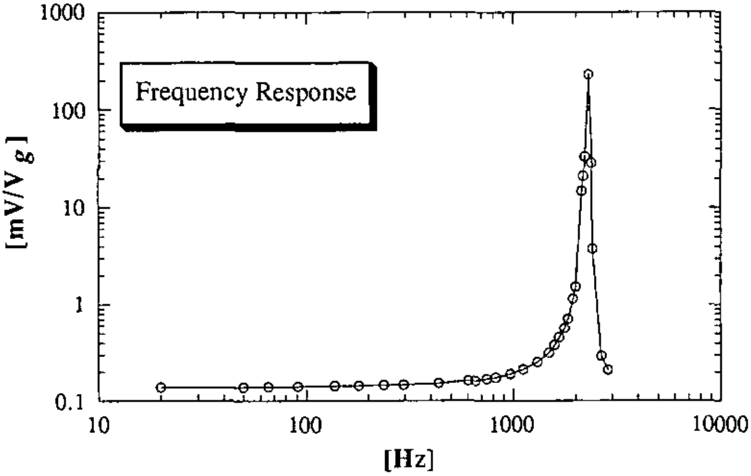

Fig. 3.4 Frequency response of a two-beam bridge-type accelerometer (first prototype)

sensitivity at low frequencies is about 150 μV/V *g* and increases for increasing frequencies. This can be clearly seen in the frequency response given in Fig. 3.4. We measured a resonance frequency of 2300 Hz. The calculated sensitivity and resonance frequency for this type of accelerometer were 123 μV/V *g* and 2660 Hz. The difference is mainly due to four reasons :

- The thickness of the beams is difficult to control (no etch-stop).
- There was not a perfect corner compensation technique used (see section 3.3).
- The junction depth of the diffused resistors is difficult to control.
- The passivation layers (silicon dioxide) on the beams have not been taken into account in the calculations.

3.1.4 Conclusions

The process sequence presented above allowed the feasibility of fabricating a piezoresistive silicon accelerometer within the imposed technological constraints to be investigated. The wet etching of the silicon membrane using a PECVD silicon nitride layer as an aluminum protection against KOH was insufficient reliable. The pinholes in the protection layer are caused by the surface roughness of the evaporated aluminum. Therefore the main work focused on replacing the wet etching of the membrane by a process for which a simple masking material can be used and the metallization was not attacked [91]. This investigation led to the development of a dry etching process for deep silicon etching. This work is described in detail in section 3.2. As measurements and simulations have shown, the thickness of the beams has to be well controlled. Thus the electrochemical etch stop will be included for the next generation of accelerometers. Furthermore compensation structures must be developed for small size accelerometers because these are too small to use the compensation technique proposed by Buser et al. [92] (see section 3.3). As the next generation of accelerometers was fabricated at ASCOM Microelectronics, the piezoresistors were implanted. The industrial process is given in section 3.4.

3.2 DEEP DRY ETCHING OF SILICON

3.2.1 Introduction

The fabrication of the first prototype has shown, that no reliable aluminum masking material against KOH for a Si etch depth of about 15 µm could be found which maintained the bipolar compatibility. As dry etching [93] had already proved the possibility to etch steps several microns deep into silicon [94], its process parameters were optimized to give a reliable, well controllable etch behaviour having an etch-rate of about 1 µm/min. and a good selectivity against standard IC-compatible masking materials. From the literature two gas combinations seemed to be promising with regard to our application : fluorine/oxygen (SF_6/O_2) [95] gas mixtures having the potential of high etch rates and chlorine/fluorine (C_2ClF_5/SF_6) gas mixtures known for anisotropic etch behaviour. Different masking materials such as photoresist, aluminum or silicon dioxide were compared. The etch trials were examined with regard to selectivity, etch depth and underetching [88].

In dry etching using parallel plate systems two basic etch configurations are distinguished, each characterized by the electrode to which the RF power is connected. In the plasma etching mode (PE), the RF power is coupled to the upper electrode, which is in contradiction to the reactive ion etching mode (RIE) with the high frequency coupled to the lower electrode on which the substrate is placed. In general the etching in the RIE mode shows higher anisotropy but exhibits a lower selectivity compared to the PE mode. These effects are due to the higher energy ion bombardment in the RIE mode, which in turn heats the substrate more up.

The combination of wet and dry etching plays an increasingly important role as a powerful tool for micromachining applications. It is often included not only into the process sequence for the fabrication of silicon accelerometers, but also for other applications such as free standing silicon structures [96] or cantilevers with square cross section for scanning probe microscopy [97].

3.2.2 Experimental Setup

Two parallel plate reactors with 13.56 MHz RF generators are used (LEYBOLD Z401S). For both systems loadlocks guarantee low contamination. The active gases are fed through a showerhead-like upper electrodes and thus gives to an excellent etching uniformity. In the first system, where the etching with SF_6/O_2 gases is performed, the RF power can be capacitively coupled either to the upper electrode (plasma etching mode: PE) or to the lower one (reactive ion etching mode: RIE). In the second system, which is used for the C_2ClF_5/SF_6 gas mixtures, only RIE can be applied.

As listed in Table 3.II, different IC-compatible masking materials were used for the deep etching of (100) p-type silicon wafers (resistivity: 3–5 Ωcm): positive photoresists AZ 1518 (standard IC-resist) and AZ 4562 (highly viscous), thermal silicon dioxide, electron-beam-evaporated aluminum.

The etched steps in silicon and the mask thicknesses were measured by means of a surface profiler (Alphastep 200) or a mechanical stylus for step height measurements (Cary Compar). The undercut was determined by SEM observation.

3.2.3 Etch Results and Discussion

Table 3.II summarizes the main process conditions on the left-hand side and the results of the deep dry etching trials on the right. The selectivity is defined as the ratio of the etch rates between silicon and the masking material. The

Table 3.II Process parameters and results of deep dry etching of silicon

Gases	Mask material	thickn. [µm]	Mode	Pressure [mbar]	Power [W]	Etch-depth [µm]	Etch-rate Si [µm/min]	Selectivity	Under cut vs Depth
SF_6/O_2	AZ 1518	1.8	PE	0.07	220	46	0.9	28	0.55
SF_6/O_2	AZ 4562	6.2	PE	0.07	220	110	0.9	20	0.55
SF_6/O_2	SiO_2 *	1.8	PE	0.05	300	150	1	85	0.65
SF_6/O_2	Al	1.8	PE	0.07	300	>500	1.3	>300	0.8
C_2ClF_5/SF_6	AZ 4562	6.2	RIE	0.12	180	30	0.6	5.2	0
C_2ClF_5/SF_6	SiO_2 *	1.8	RIE	0.1	160	34	0.5	19	0.56

* thermal silicon dioxide

undercut is calculated by dividing the lateral underetch distance by the vertical etch depth.

a) Fluorine/Oxygen Gas Mixtures

In the first phase, SF_6/O_2 gases were tested because they offer high selectivity and thereby deep silicon steps. These gas combinations are also well known for dry etching of silicon in IC-technology [98]. Since the silicon substrate is grounded for PE, it is subjected only to low energy ion bombardment. Hence, the photoresist is less damaged in the PE mode than in the RIE mode. This is advantageous in order to achieve high etch depths using a photoresist mask. Therefore the PE mode has been chosen instead of RIE for these etch trials. Due to the lower heating of the substrate higher power can be applied than in the RIE mode. The greater power leads to the production of more active etching ions. Thus, the decrease of the etch rate due to the low energy impact can be compensated by an increase of reactive species. We finally found, for similar silicon etch rates, a selectivity for photoresist that is at least three times better than that for RIE.

Using a standard IC-photoresist (AZ 1518) a maximum etch depth of 46 µm has been obtained before the photoresist could no longer guarantee complete protection of the surface. As indicated in Table 3.II, with a thicker photoresist (AZ 4562) the maximum achievable etch depth could be increased to more than 100 µm at a selectivity of about 20. The SEMs of Figs. 3.5 and 3.6 show an etched convex corner and the profile of a etched step where the AZ 4562

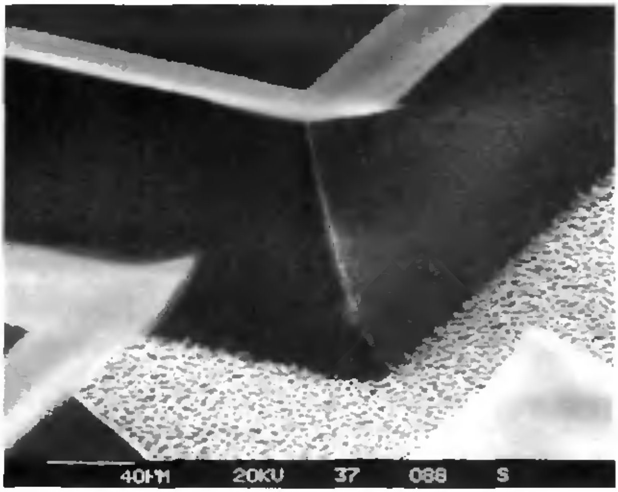

Fig. 3.5 Silicon corner (depth 110 µm) etched with SF_6/O_2 and a photoresist mask (not yet stripped)

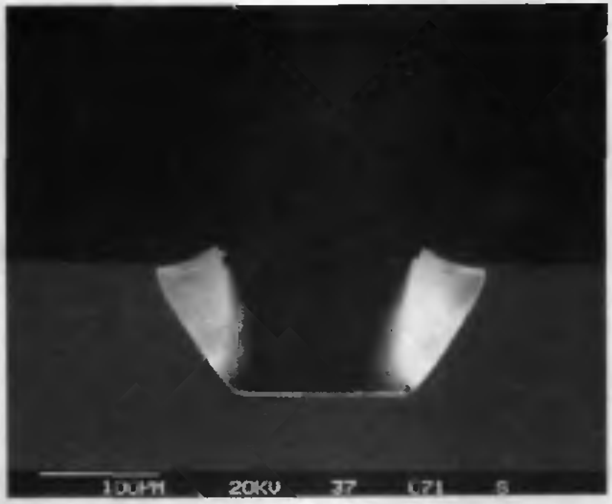

Fig. 3.6 Etch profile using SF_6/O_2 with a photoresist mask (not yet stripped)

has not been stripped yet. It can be clearly seen that the fluorine gases lead to a large undercut. This is due to the fluorine atom isotropically etching silicon, which is known to occur at a considerably higher rate than the vertical etch induced by ion bombardment. As Fig. 3.5 illustrates further, the sidewalls of the silicon corner are relatively smooth and the etched surface is granulated. The roughness (about 5 % of the etch depth) is a result of ion impact and (re)deposition effects.

With our etch conditions as given in Table 3.II increasing the exposed silicon surface resulted in a rise in the etch rate. Furthermore, we observed that the photoresist mask deteriorates faster. The damage of the photoresist is mainly caused by the increased temperature of the substrate, since more etch reactions take place due to the increased exposed silicon area. At higher temperature the etching species are also more reactive and thus, the chemical part becomes more dominant than the physical bombardment. This results in a higher etch rate with greater undercut. However, the effect of rising etch rate with increasing exposed silicon surface can only be sustained if the consumption of reactive ions is small compared to the generation rate. Otherwise a loading effect can occur and thereby decrease the etch rate.

Etch experiments were also carried out using silicon dioxide as masking material. In contrast to photoresist, it was possible to increase the RF power and to lower the working pressure without taking the risk of burning or damaging the oxide mask. The oxide etch rate turned out to be even smaller than that of the photoresist. A selectivity of 85 and etch depths up to 150 µm could be achieved. A convex corner and an etched silicon step with the oxide

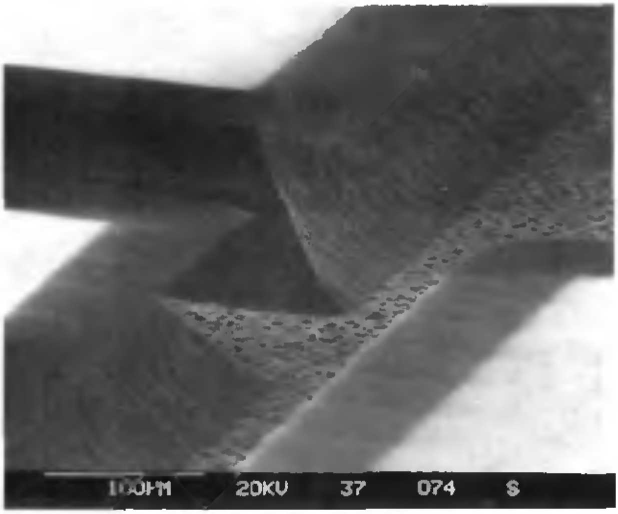

Fig. 3.7 Silicon corner (depth 116 μm) etched with SF_6/O_2 using an oxide mask (not yet stripped)

mask still on top are illustrated in Figs. 3.7 and 3.8.

As a the third IC-compatible masking material, aluminum was applied. First tests revealed that at relatively high silicon etch rates, the aluminum mask is barely etched at all in SF_6/O_2 gases; the oxygen seems to react with the aluminum to form alumina which is resistant to fluorine plasmas. Thus, it was

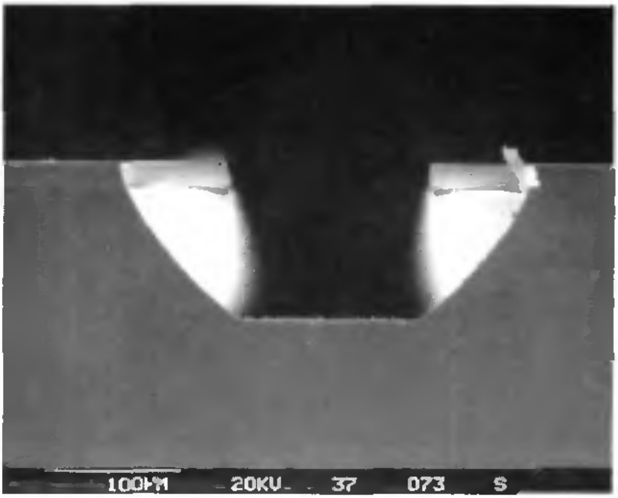

Fig. 3.8 Etch profile using SF_6/O_2 with a oxide mask (not yet stripped)

possible to realize silicon steps of more than 500 µm.
For a fixed RF power the working pressure was optimized for small undercut and high etch rate. Maximum etch rates were found between 0.08 mbar and 0.12 mbar for a power range of 250 ± 50 W. At pressures lower than 0.03 mbar the power had to be reduced in order to avoid high energy ion impact that would have damaged the masking material. Because of the low power, however, the etch rate decreased considerably. Finally, we observed no significant change in the undercut and etch profile between 0.03 mbar and 0.07 mbar. As pressure was increased from 0.08 mbar to 0.12 mbar, the sidewalls became more and more rounded [87].

b) Chlorine/Fluorine Gas Mixtures

In order to reduce the undercut, in a second phase, chlorine/fluorine gas mixtures which have been reported to exhibit good anisotropy were examined [99]. RIE of silicon with C_2ClF_5/SF_6 gas combinations was performed at relatively high RF power. Thereby, the silicon etch rate, which is normally small for chlorine gases, could be increased to about half a micron per minute. Since, however, photoresist is strongly attacked in chlorine gases, a rather high working pressure was chosen to weaken the etching by ion bombardment.
As shown in Table 3.II, silicon etching up to 30 µm has been achieved with a selectivity of more than five by using relatively thick photoresist (AZ 4562). In Figs. 3.9 and 3.10 a convex corner and the profile of an etched step can be seen. An almost perfect anisotropy is observed, i.e., practically no undercut

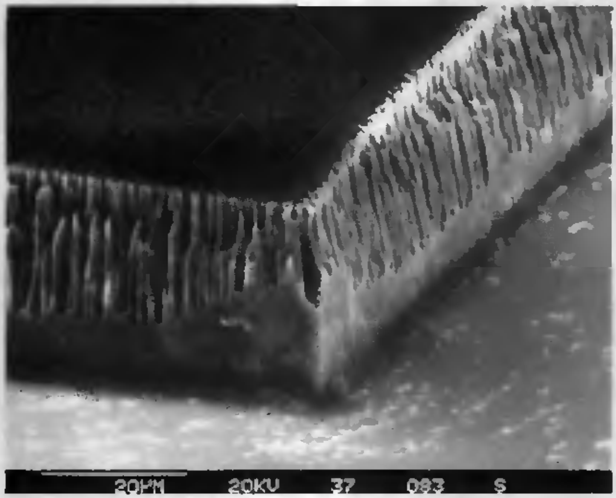

Fig. 3.9 Silicon corner (depth 30 µm) etched with C_2ClF_5/SF_6 and a photoresist mask (not yet stripped)

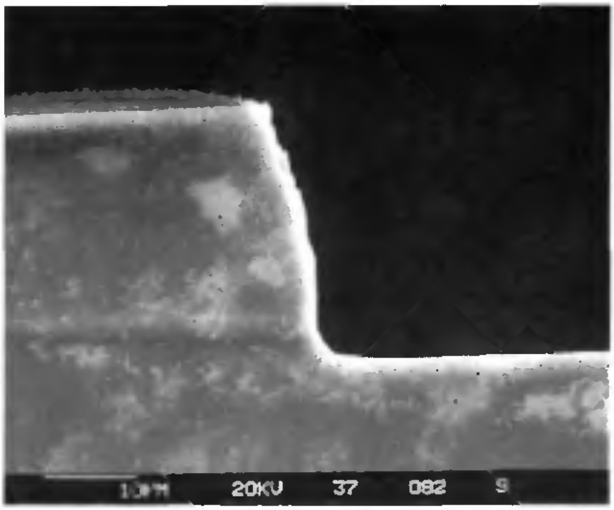

Fig. 3.10 Silicon profile etched with C_2ClF_5/SF_6 and a photoresist mask (not yet stripped)

and vertical sidewalls. One reason may be that chlorine atoms cover the silicon surface and thereby slow down further etching reaction. Especially on the sidewalls where the energetic ion bombardment is low, only a few volatile $SiCl_x$ compounds are produced and almost no etching occurs [100].

Applying silicon dioxide as masking material resulted in a similar maximum etch depth as for the 6.2 µm thick AZ 4562; i.e., 34 µm deep silicon steps have been achieved using 1.8 µm thick thermal oxide. However, in contrast to the photoresist mask, the oxide mask exhibits an undercut. (A similar effect has also been noticed for SF_6/O_2 gases: using silicon dioxide instead of photoresist as mask leads to an enhanced undercut.) It might be that more radicals containing carbon are generated during etching with photoresist than with an oxide mask. Such radicals can react on the surfaces and produce polymer films. These polymer depositions stay on the sidewalls since these are only subjected to low energy impact, and thus impede lateral etching. An additional reason for an increased undercut may be that silicon dioxide as masking material prevents polymer film formation because the oxygen released during etching reacts with the unsaturated species to form volatile products [93].

When only a small part of the wafer is covered with photoresist, the same effect has been observed as for SF_6/O_2 gases: the photoresist is damaged faster. Thus, etch depths are smaller and, in addition, the high anisotropy is lost. For example, when less than 50 % of the wafer was covered by AZ 4562, an etch depth of 20 µm and an undercut of 0.2 were measured.

3.2.4 Conclusions

Process parameters of two gas mixtures (C_2ClF_5/SF_6 and SF_6/O_2) were optimized with regard to a good selectivity towards the masking material and a relatively high etch rate (≈ 1 µm/min.).
Several masking materials were tested for SF_6/O_2 gases: photoresist, silicon dioxide and aluminum. Photoresist exhibits a lower selectivity but leads to less undercut than does silicon dioxide. As aluminum is barely etched at all in SF_6/O_2 plasma, it was possible to etch more than 500 µm deep steps out of silicon. The major drawback of the SF_6/O_2 processes is the relatively isotropic etch behaviour.
In order to investigate the influence of the masking material on the processes using C_2ClF_5/SF_6 gases, photoresist and silicon dioxide were tested. The trials with oxide showed a rather isotropic etch behaviour whereas no undercut was observed for photoresist. This may be due to sidewall passivation by an organic layer which slows down the lateral etching. Compared to the pure fluorine gas mixtures, the measured selectivity is reduced by a factor of about four. Thus, vertical steps of up to 30 µm were achieved with the photoresist mask in a C_2ClF_5/SF_6 plasma.
Both gas mixtures exhibit a selectivity to photoresist high enough to pierce through a 12 µm thick silicon membrane using a photoresist mask. The SF_6/O_2 processes show a relatively isotropic etch behaviour. However, given prior knowledge of the reproducible undercut, these effects can be compensated for by an appropriate design of the silicon beams of the accelerometer. Vertical walls were obtained using a C_2ClF_5/SF_6 plasma. Thus, rectangular beams can be fabricated. As ASCOM Microelectronics only possesses a fluorine plasma etcher, the dry etching process with SF_6/O_2 gases was used for the second generation of accelerometers.

3.3 ETCH COMPENSATION STRUCTURES

3.3.1 Introduction

KOH is often used as an anisotropic wet etchant for silicon micromachining, because of its high anisotropy [101] (ratio of the etch rate of plane (001) to the etch rate of plane (111) ≈ 150 for KOH 40 weight percent at 60°C). Additionally it is easy to handle, relatively harmless and cheap. Silicon dioxide or nitride are mostly used as masking materials. It is well known that corner undercutting occurs at convex corners in anisotropic etching of (100) oriented silicon [102 - 105] using any known anisotropic etchant such as EDP [106] (a mixture of ethylenediamine, pyrocatechol and water) or KOH, if the edge of the mask is parallel to the [110] orientation [62]. This is an unwanted effect for most applications, e.g. for the fabrication of accelerometers. In order to keep the cross sensitivity of an accelerometer as low as possible the mass is suspended by the beams at its corners. Therefore perfect convex corners of the mesa like mass are mandatory for good device behaviour. Underetching of the corners decreases the effective seismic mass which in turn lowers the sensitivity of the device. This can be clearly reduced or even prevented by so-called corner compensation structures which are added to the corners in the mask layout.

In the past few years several different compensation structures for KOH have been published (see Fig. 3.11). Bean et al. [107, 108] added small squares whose sides were parallel to the <110> direction. Buser et al. [92, 109] published a rectangular compensation structure with <010> oriented bands. This renders feasible the etching of a convex corner that is formed by two {111} planes. The band, which is added to the convex corner in the <010> direction, is underetched by vertical (100) planes. Thus, shortly before the etch depth is reached, a vertically oriented membrane is formed that frees the convex corner from the surface to the etch ground. Since the (100) planes all etch at the same rate, the width of the compensation has to be twice the etch depth. Puers and Sansen [110] compared in their work squares, triangles and flat triangles. Wu et al. [111, 112] also proposed triangles. His and Puers' structures are based on the idea that the sides of the compensation triangle are parallel to the fastest etching planes. The size of the triangle is given by their etch rate of these planes which in turn depends on the etchant concentration and etch temperature.

Using <010> oriented beams, a perfect sharp corner defined only by (111) planes is obtained, whereas the triangular and squared compensations give rather rugged corners. Wu et al. found the {212} planes to be the undercutting planes at the convex corners in a mixture of KOH and propanol. For a pure

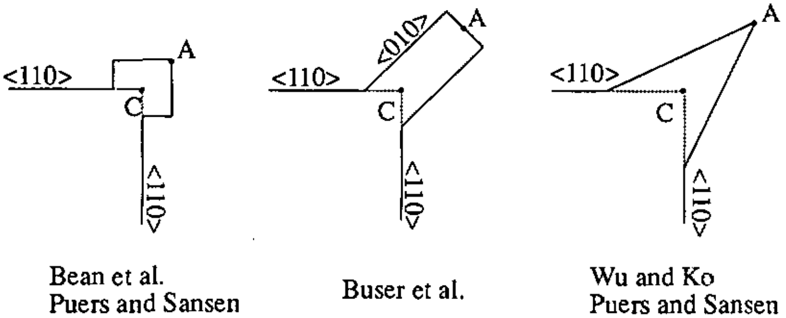

Fig. 3.11 Different compensation structures (distance AC determines the spatial requirement)

KOH solution Bean et al. and Puers et al. proposed the {313} planes to be the fastest etching ones. This is in contradiction to the results of Sandmaier et al. [113 - 115], who found the {411} planes responsible for underetching. Linder et al. measured the {122} planes for KOH concentrations below 6 moles per litres and the {411} planes for higher concentrations to be dominant [116].
The distance AC in Fig. 3.11 is a parameter for the spatial requirements of the different compensation structures. We find with our etch conditions (KOH 40%, 60° C) for AC:

square :	2.2 * etch depth	[110]
triangle :	6 * etch depth	[110]
band in <010> direction :	> 4 * etch depth	[92]

For most of the applications as V-groove crossings or accelerometers, there is not enough space to apply these compensation structures. Thus, the etch front which largely determines the corner undercutting has to be deviated, using combinations of these structures. Based on this idea Gerlach published a series of squares with mask slits [117], and Sandmaier et al. [113] presented a squared compensation structure combined with <110> oriented beams. Another compensation structure using a combination of <010> and tens of <110> oriented beams proposed in the same article by Sandmaier results in a perfect convex corner. We focused our work on compensation structures with small spatial requirements with regard to the application in accelerometers.

3.3.2 Simulation and Experimental

The underetching of simple compensation structures can be easily predicted. As they are becoming more and more sophisticated, etch simulation programs

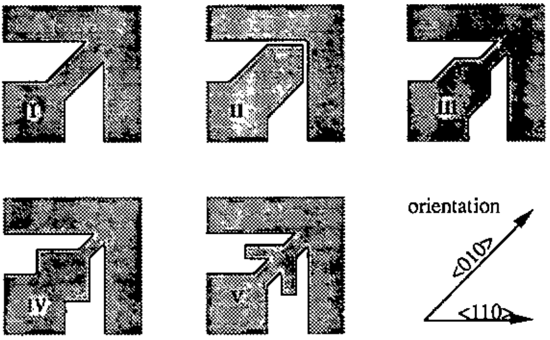

Fig. 3.12 Tested compensation structures for (001) silicon and using KOH 40% at 60°C

are needed to reduce the expense for developing compensation structures with low spatial requirements. Simulation allows the etch front and the etched structure to be visualized within minutes. At our institute, the Anisotropic Simulation Etch Program ASEP [118, 119] has been developed and used for the design of compensation structures for accelerometers. The program treats the etch behaviour of all the {001}, {111} and of the fast etching {311} planes at any concave or convex corner. Thus, the etch front at the wafer surface can be well simulated. However, as at the base of a convex corner several different planes are etched [114, 116], the final corner shape must be determined experimentally in spite of simulation.

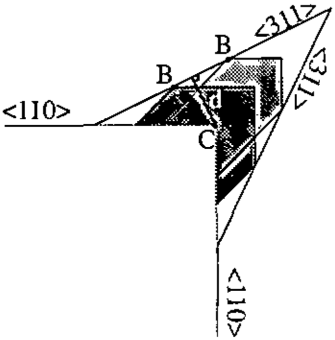

Fig. 3.13 Basic idea of all compensations

We tested the five different compensation structures shown in Fig. 3.12. All are based on the idea, that the {311} planes through B will reach point C when the etching will be stopped (Fig. 3.13). Etch tests with a total of 68 different dimensions of these 5 basic designs were performed on 3 inch p-type silicon wafers with a thermal oxide mask. The test structures were etched in 40 % KOH at 60°C.

3.3.3 Etch Results

Design I resulted in the sharpest corner. But with small space conditions the convex corners are not etched free. Although designs II to V are based on the same idea, we got different results for different design sizes. We noticed that the larger the <010> oriented beam the better the corner obtained. The outer, second <010> beam in the designs III to V increased the sharpness of the final convex corner compared to design II. After an etch depth of 380 μm, for all compensation designs, a ridge like formation about 8 μm high remained in the <010> direction on the etched membrane. We obtained the best corner quality with design III. Figure 3.14 shows a close look at a compensated corner of a realized piezoresistive silicon accelerometer.

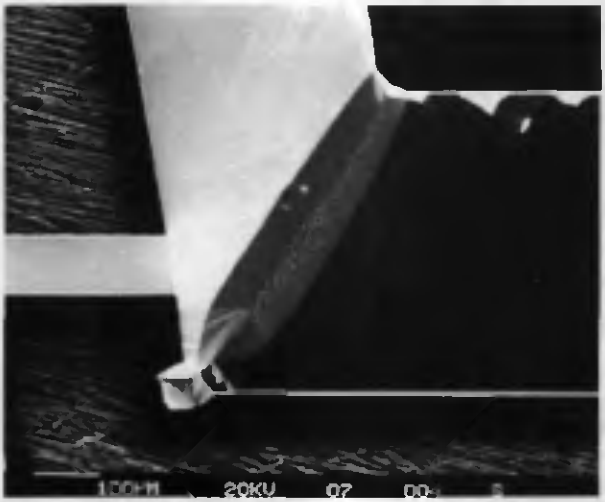

Fig. 3.14 Convex (compensated) corner of a piezoresistive silicon accelerometer

3.3.4 Conclusions

The etch simulation program ASEP allows the etch front of any mask structure in KOH to be predicted. Due to the unknown etch behaviour at the base of a convex corner, the final corner sharpness, after having completely underetched the compensation structure, can not be predicted, but the main etched form corresponded well with the simulation. The compensation, using beams in the <010> direction, results in a perfect sharp convex corner, but it is not feasible, if there is little space for the compensation structure. As the different sized designs with the same etch distance of the {311} planes to the final corner resulted in different corner shapes, we conclude that the {311} planes are not the fastest etching ones, which agrees with the observations of Sandmaier. The different etch rates obtained by the wagon wheel method show that the {311} plane is not exactly in the direction of the etch rate maximum [120]. Furthermore we measured an angle at the wafer surface of about 31° of the fastest etching plane to the <110> direction, which corresponds better with the angle of the <410> to the <110> direction (30.96°) than of the <310> to <110> (26°). This explains as well the better corner quality for larger beams. Using the electrochemical etch-stop, the remaining 8 µm high silicon ridge in the <010> direction can be etched away by overetching in order to get a flat membrane. We have chosen design III as a compensation structure for accelerometers, because it gave adequate corner quality. The corner is rounded on a distance of 40 to 70 µm (Fig. 3.14). Design V could be better adapted to the different etch rates which will lead to a similar compensation structure as proposed by Sandmaier, which is a combination of a <010> and several <110> oriented beams. The experiments have shown, that compensation structures must be adjusted to every mask design.

3.4 SECOND PROTOTYPE

3.4.1 Design

The second prototype was entirely fabricated at ASCOM Microelectronics in Bevaix. At the beginning of 1991 the company's production line moved into a new fabrication building. Thereby the wafer size was changed from 3 to 4 inch. The first design of the second prototype was fabricated on three inch. The sensor chip was designed squared in order to fabricate on the same wafer sensors with three different beam configurations but equal masses. As many piezoresistors were placed in the region between mass and frame, only the beam's definition and metallization masks determined finally the sensor chip. All the other mask patterns were identical from chip to chip. Therefore only two masks had to be replaced if the beam configuration was changed.
First the overall size of a bridge-type accelerometer (length of the seismic mass and twice the length of a beam) was chosen to be 3 mm. Since an accelerometer for the range of 50 g with a large bandwidth was required, the length of the beams was fixed at 300 μm, although calculations for a bridge-type accelerometer have shown that a beam length of 500 μm would lead to a maximum sensitivity for this overall size. According to analytical formulae the shorter beams reduces the maximum achievable sensitivity by 20 % but on the other hand increases the resonance frequency by 60 % (see section 2.3).
Four piezoresistors were connected in a wheatstone bridge. As piezoresistive pressure sensors with aluminum on the membrane show offset hysteresis for varying temperature [121], highly doped regions connect the piezoresistors on the beam. Hence Aluminum for interconnection was only used on the frame. Every piezoresistor consists of two 15 μm x 75 μm boron doped diffusions connected by a highly doped region. Thus, the minimum width of a beam is mainly given by the outer dimensions of a piezoresistor. As the electrochemical etch-stop was applied, the thickness of every beam is given by the thickness of the epitaxial layer (12 μm).
Two bridge-type designs with 2 and 4 beams, respectively, and one cantilever-type design were realized on the same wafer. The two beams of the bridge-type have a width of 200 μm on the mask and support the seismic mass in the middle of two opposite sides. The piezoresistors are symmetrically placed on the two beams to compensate electrically any rotation about the longitudinal axis. In order to reduce the transverse sensitivity of the four-beam bridge-type

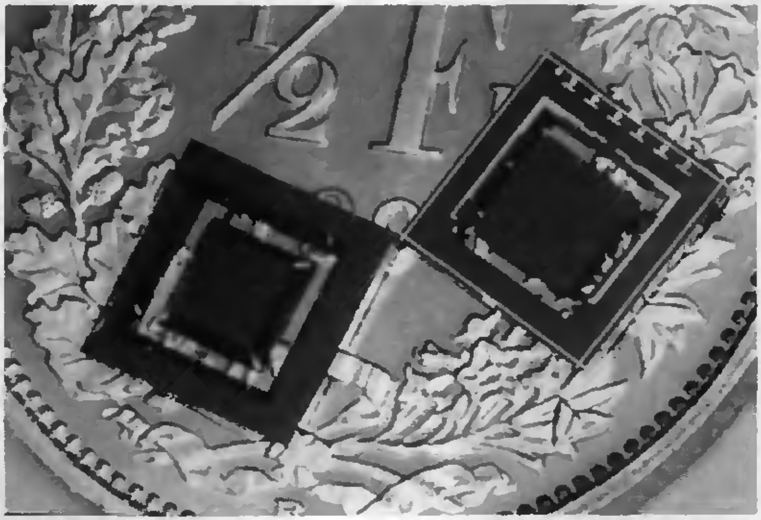

Fig. 3.15 Front side and back of a four-beam bridge-type sensor chip

design, the beams on each side should be spaced maximally. This implies the mass to be supported at its corners. Since overetching can not guarantee a perfect mesa form of the proof mass (see section 3.3), the beams are at a distance of 200 µm from the corner. This assures a well controlled form of the beam. To have a reasonable sensitivity for the four-beam bridge-type accelerometer its beam length was minimum, i.e. 120 µm on the mask. The mass of the cantilever-type is supported by two beams of 800 µm width each and an intermediate space of 580 µm.

A 400 µm large region on the frame between the metallization and the border of the chip and the contact pads was kept free of metallization in order to allow trials of different encapsulation methods. This results in a chip size of 4.5 x 4.5 mm. Since having three different mass-beam configurations on the same wafer causes many difficulties, the 4 inch design consists only of four-beam bridge-type accelerometer configurations. Due to the isotropic etch behavior of the dry etching with SF_6/O_2, the beams' width was increased to 130 µm. The length of the beam (300 µm) as well as the size of the seismic mass (2.4 x 2.4 mm) have not been changed. The number of chips per wafer was raised from 120 on 3 inch to 218 on 4 inch. Figure 3.15 shows the back and the front side of a four-beam bridge-type accelerometer of the 4 inch design.

3.4.2 Transverse Sensitivity

The aim of the development of an accelerometer is to fabricate a device which is sensitive in only one axis. As the mechanical transverse sensitivity is mainly determined by the configuration of the sensor, it has to be taken into account during the design phase. The beams of a piezoresistive silicon accelerometer are at the top surface of the sensor chip. The center of mass of the proof mass, however, is in the midplane of the silicon wafer, about 200 µm below the surface. This offset of the center of mass below the plane of support leads to movement of the mass when it is subjected to transverse acceleration.

The mass of a four-beam bridge-type accelerometer tends to deflection under an acceleration along the y- or the x-axis as shown in Fig. 2.14 as the second and third mode, respectively. The tilt up at one end of the mass is compensated for by a tilt down at the opposite. The electrical response to these deflections can be greatly reduced by the appropriate interconnection of the sensing resistors on the beams. Sandmaier [31] first published a configuration using eight piezoresistors for a bridge-type accelerometer. There are two longitudinally loaded resistors on each beam, one at the mass end and one at the frame end. They can be connected to a Wheatstone bridge as given in Fig. 3.16, where the subscripts refer to mass or frame end and the number refers to the beam. Although acceleration in the x and y directions results in a variation of the individual resistor values, the bridge output voltage remains constant assuming identical resistor changes (see Table 3.III). As can be seen using Table 3.III every branch of the Wheatstone bridge in Fig. 3.16 does not change for any cross-acceleration, since the two sensing resistors on each branch change with opposite sign and thus compensate each other.

Let us consider a Wheatstone bridge which consists of four identical resistors and assuming identical resistor changes under acceleration. Furthermore we

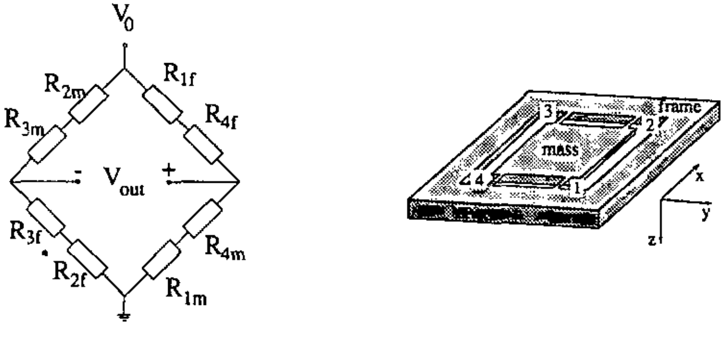

Fig. 3.16 Connection scheme to compensate cross-axis acceleration (subscripts refer to mass or frame end, number refer to beams)

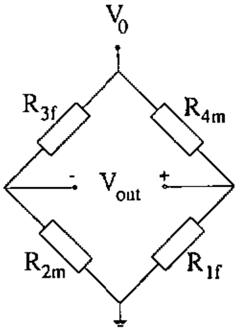

Fig. 3.17 Connection scheme using four sensing resistors to compensate cross-axis acceleration (subscripts refer to mass or frame end, numbers refer to beams)

Table 3.III Changes of the individual resistors under crossacceleration

	ΔR with x accel	ΔR with y accel	ΔR with z accel
R1f	+	-	-
R1m	-	+	+
R2f	-	-	-
R2m	+	+	+
R3f	-	+	-
R3m	+	-	+
R4f	+	+	-
R4m	-	-	+
Vout	0	0	+

assume that two of the resistors will increase and the other two decrease. Thus the differential output will only change if the increasing resistors are connected on opposite branches of the bridge. If these two increasing resistors are adjacent, the output voltage will not change for any acceleration. Consequently we propose with only four sensing resistors e.g. with R_{1f}, R_{2m}, R_{3f} and R_{4m}, an interconnection scheme (Fig. 3.17) whose output is not affected by any cross-axis acceleration. It can be seen from the subscripts of the chosen four resistors, that there is one resistor on each beam and two of the four are implanted at the mass end and the other two at the frame end of the corresponding beam. In addition those at the mass end are placed on two beams situated diagonal opposite each other, e.g. on the beams with the numbers 2 and 4 (see Fig. 3.16), whereas those at the frame end are placed on the beams with the numbers 1 and 3. Therefore the configuration of the Wheatstone bridge as given in Fig. 3.17 (see also Table 3.III) will only change its output voltage with z-acceleration. Since technological reasons (e.g. homogeneity of doping of the resistors) do not favour the eight-resistor configuration for cross-axis compensation, the standard Wheatstone bridge with four sensing resistors (Fig. 3.17) is much more advantageous due to its simplicity.

Unlike the bridge-type accelerometer, the cantilever-type does not have a symmetry of bending due to cross axis accelerations. An acceleration in x deflects the mass upward, bending the beam. Unlike the bridge-type accelerometer, it is impossible to distinguish between acceleration in the vertical axis (principle axis) and acceleration in the x-direction. Thus there is an important off-axis sensitivity in the range of 5 to 15%, depending upon the exact geometries of the structure [122]. This problem can be avoided by either adding a mass to the top [123, 30] or by tilting the accelerometer so that the center of mass and the center of bending of the beam are coplanar in this off-axis direction [25]. Typically, this angular error is in the 3 to 8° range.

3.4.3 Fabrication

The sensor chips are fabricated on double-side polished, four inch wafers of thickness 390 µm. The substrate is (100) oriented silicon, boron doped to a resistivity of 3-5 Ωcm. In a first step a 12 µm thick, phosphorus doped epitaxial layer was grown. After a thermal oxidation, the oxide was patterned and a boron doped layer was predeposited. The deep diffusion established the contact to the p-type substrate. The p^{++} regions were realized in a similar way, but they were diffused only some microns deep into the epitaxial layer. In a next step, n-type regions were defined in order to contact the epitaxial layer. The oxide grown during the diffusion of the n-type regions served as a mask for the boron implantation of the piezoresistors. This step was followed by a diffusion. The interconnections of the piezoresistors to form the wheatstone bridge and the interconnections required for the electrochemical etch-stop were made with evaporated Aluminum. As the thermal oxide on the back was not thick enough to withstand KOH etching for an etchdepth of about 380 µm, an additional PECVD silicon nitride layer was deposited on the back. Alignment of the openings on the back with the top resistors was achieved by means of a double side mask aligner. Alignment marks on both sides were realized in the first photolithography of the whole process sequence in order to improve the precision of further alignments. After the opening of the back, a photoresist mask was patterned on the front side. This layer served as a mask against plasma etching and defined the beams of the accelerometer. Membranes were etched anisotropically in 40 weight percent potassium hydroxide at 60°C, while protecting the front side from the KOH by clamping the wafer in a chuck, which left only the back side exposed to the etch solution. To achieve a high uniformity of the membrane the four electrode electrochemical etch stop was used. This technology requires an epitaxial layer and a contact to the substrate and to the epitaxial layer.

The electrochemical etch-stop is based on the potential dependent etch rate of p- and n-type silicon [124]. B. Kloeck et al. [125] measured an open circuit potential (OCP) of about -1.5 V (with respect to the reference electrode, a saturated Calomel Electrode) for both types of silicon in the <100> direction. Etch stopping is observed on both materials for biases sufficiently positive of the OCP. It is supposed that an oxide is formed on the silicon surfaces and thus stops the etching. In the four electrode configuration [126], the potentiostat is connected to the p-substrate to maintain a controlled etching potential, close to the OCP of p-type silicon. A second voltage supply is connected between the epitaxial layer and the substrate to bias the epitaxial layer at a passivating potential, i.e. more anodic than the oxide formation potential for n-type silicon (-1.08 V with respect to the reference electrode), and thus more than + 0.4 V with respect to the substrate. In practice, this voltage is set at about 1.5 V, which puts the epitaxial layer at 0 V with respect to the reference electrode.

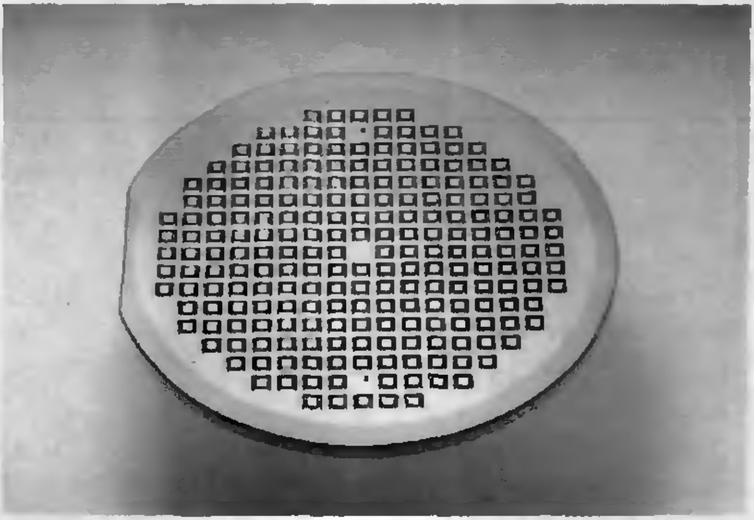

Fig. 3.18 Processed 4 inch wafer containing 218 sensor chips

The four elctrode setup is advantageous because it gives excellent results even with reverse-diode leakage currents as large as 10 mA per wafer from p-n junction defects. As soon as the etch front reaches the n-type epitaxial layer, the current through the counter electrode (platinum) increases and forms a peak, which signals the onset of the etch stop. In a fabrication this peak can be automatically detected. As overetching is not critical, very smooth surfaces with homogeneous thickness can be achieved.

After the wet etching of the membrane, a photoresist film was sprayed onto the back. In the next step the membrane was etched through from the front side using a dry etching process (see section 3.2) with the photoresist mask patterned before the KOH etching. The sprayed photoresist layer prevented the beams being thinned from the back during overetching. In spite of this protection resistors with no passivation layer showed an increased resistivity after plasma etching. An additional anneal at 400°C for 15 minutes led to the resistivity returning to the initial value. After stripping the remaining photoresist, the 218 sensor chips are ready to be diced and/or encapsulated. The processed 4 inch wafer can be seen in Fig. 3.18. The whole process is summarized in Table 3.IV and visualized in Fig. 3.19.

Table 3.IV Process sequence for piezoresistive accelerometers using a bipolar compatible, industrial process (ASCOM Microelectronics, Bevaix)

Step	Process	Mask
1	Epitaxial layer growth, 12 μm, phosphorus doped	
2	Thermal oxidation, 8500 Å	
3	Double side photolithography and oxide opening for p^+ regions	Mask 1 / 2
4	Predeposition of boron	
5	Removal of oxide layers	
6	Boron diffusion + oxidation	
7	Photolithography and oxide opening for p^{++} regions	Mask 3
8	Predeposition of boron	
9	Removal of oxide layers	
10	Boron diffusion + oxidation	
11	Photolithography and oxide opening for n^+ regions	Mask 4
12	Predeposition of phosphorus	
13	Removal of oxide layers	
14	Phosphorus diffusion + oxidation	
15	Photolithography and oxide opening for piezoresistors	Mask 5
16	Boron implantation	
17	Anneal piezoresistors + oxidation	
18	Photolithography and oxide opening for contacts	Mask 6
19	Photolithography and oxide opening on the back for the membrane etching	Mask 7
20	Aluminum evaporation	
21	Photolithography and aluminum etching	Mask 8
22	Aluminum anneal	
23	Deposition of PECVD nitride on back side	
24	Photolithography and nitride opening for membrane	Mask 9
25	Photolithography front side for definition of beams	Mask 10
26	Membrane etching in KOH	
27	Covering the back by photoresist	
28	Plasma etching from the front side	
29	Stripping photoresist	

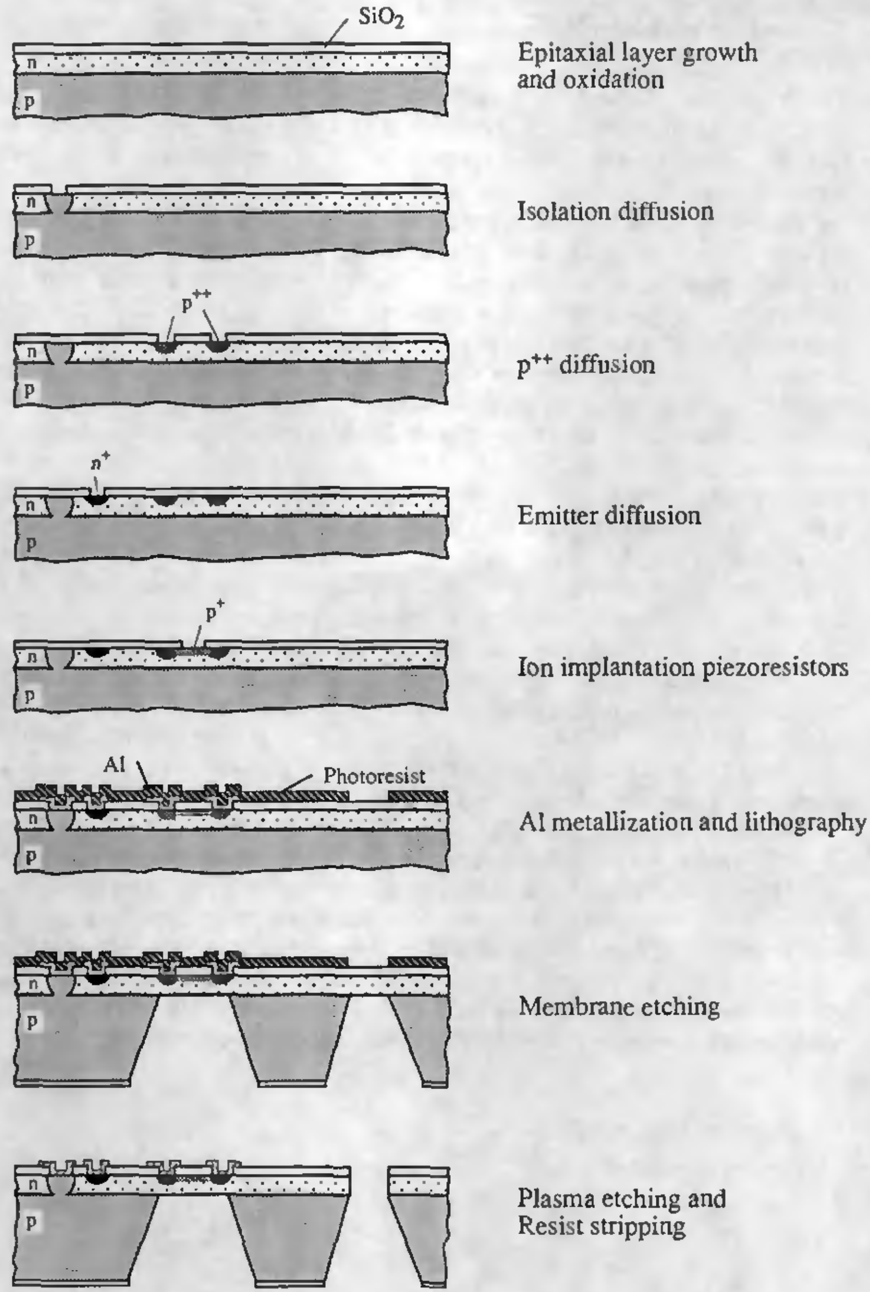

Fig. 3.19 Fabrication sequence of the second prototype

3.5 CONCLUSIONS

The fabrication of the first prototype showed that a PECVD silicon nitride layer as an aluminum protection against KOH was insufficiently reliable and that for good control and reproducibility of the beam thickness the electrochemical etch stop is mandatory. In order to replace the wet etching of the silicon membrane a dry etching process using SF_6/O_2 or C_2ClF_5/SF_6 gas mixtures was developed. The pure fluorine gas mixture showed a rather isotropic etch behaviour whereas vertical steps were etched with the chlorine/fluorine gas combination. Both gas mixtures exhibited a selectivity to photoresist good enough to pierce through the approximately 12 μm thick silicon membrane. This process and also the electrochemical etch-stop were applied for the second prototype. This small design required an investigation of etch compensation structures against the etching of the convex corners of the seismic mass. A combination of two different large bands in the <010> direction was optimized and resulted in an adequate corner quality.

Since the peak stress regions of a beam of a bridge-type accelerometer occur on each end of the beam with opposite signs (sections 2.3 and 2.4), longitudinally oriented piezoresistors allow a full Wheatstone bridge to be formed. Furthermore in order to eliminate theoretically completely the cross-acceleration sensitivity the four sensing resistors of the bridge-type design were interconnected in an appropriate manner. Not only electrical means, but also the mechanical design helps to reduce the transverse sensitivity, e.g. large spacing between two beams on each side of the four-beam bridge-type accelerometer rises the resonance frequencies of the unwanted higher modes much above the sensitive mode. By contrast, to reduce the more important transverse sensitivity of a cantilever-type the die must be canted by an angle of 3 to 8° or an additional mass has to be added to the top. To see the consequences of the different types of accelerometers, two bridge-type with two or four beams and a cantilever-type accelerometer were fabricated. The four-beam bridge-type accelerometer of the second generation was designed for a range of 50 *g* having a high resonance frequency. The whole second generation was fabricated at ASCOM Microelectronics. The measured characteristics compared to simulated results are discussed in the next chapter.

Chapter 4

Characterization of the Sensor Chip and Comparison with Simulation

A sensor chip has to be characterized before encapsulation in order to control the reproducibility of the micromachining and to compare its performance with theoretically expected data. The easiest way to test both the mechanical and electric functioning is to turn the accelerometer in the gravitational field. Further data such as resonance frequency and acceleration range can be determined using a vibrating table. For these measurements the sensor chips were mounted on a Dual-in-Line package. The different measurement apparatus are described in section 4.2. In section 4.4 the results of three different accelerometer designs are discussed and compared to simulated results.
Parts of this chapter have previously been published in [64].

4.1 INTRODUCTION

In integrated circuit production, every step of the process is well controlled. In sensor technology it is much more difficult to control the mechanical functioning and the electronic part of the device. At least before encapsulation of the sensitive element, it has to be thoroughly tested to avoid high costs and to control the reproducibility of the micromachining. Turning the sensor chip upside down in the gravitational field corresponds to an acceleration of ± 1 g. This simple setup allows the simultaneous mechanical and electrical testing of the chip. A voltage change at the output and a small offset confirm homogeneous doping of the piezoresistors, correct metal interconnections and the integrity of the beams. Similar sensitivities of sensor chips from different wafers indicate well controlled micromachining. A further control parameter, the resonance frequency, can be measured electrically or optically using a vibrating base. Small cracks in the beams can be discovered by optical inspection. Since an accelerometer is a very stress sensitive device, the sensor chip has to be carefully mounted in order to avoid stress on the frame being introduced.

4.2 EXPERIMENTAL

All physical dimensions of the sensor chip except the thickness of the beams were controlled using an optical microscope with an integrated, calibrated ruler. As the maximum step height of our surface profiler (Alphastep 200) is 160 μm, the beam could only be scanned from the back with respect to the underlying support. This turned out not to be reproducible enough, because the roughness of the chip's front surface could not guarantee a precise reference level. Thus the only reliable way to determine precisely (± 0.1 μm) the beam's thickness was a SEM picture.

Since the voltage change of the piezoresistor's wheatstone-bridge can be directly measured with a standard voltmeter, no further electronic circuitry was needed. Thus a commercially available amplifier was only used to transform the relative voltage output into a value relative to the ground. For all measurements a constant DC voltage of 5 V was applied.

4.2.1 Static Measurements

Turning the device in the gravitational field allows the linearity and sensitivity in all 3 axes to be measured and hysteresis effects in the ± 1 *g* acceleration range to be detected. The setup of the inclination table consisting of two high precision stepper motors (Microcontrôle; RT 200 PP one step = 1/1000° and RT 120 PP 1 step = 1/100°, power supply TL 78) is shown in Fig. 4.1. The pins of the DIL 24, on which the sensor chip was mounted (see section 4.3), were clamped through the slits of a metallic plate into a Textool socle. The metallic plate was directly screwed on one stepper motor, and thus the metallic surface became the reference plane. The horizontal starting position with respect to that plane was fixed using a water gauge (precision ± 0.0023°). In a first step the device was turned 360° around the x-axis (orientation of the coordinate system see Figs. 3.16 or 4.4) measuring at angles which corresponded to an acceleration step in the sensitive axis direction of 0.2 *g*. Back in the horizontal position, the device was turned around the z-axis by 90° and the same measurements were performed with the new chip orientation (rotation around y-axis). For temperature measurements in the range of -40°C up to +120°C a thermally isolating cap and a Thermostream® system

Fig. 4.1 Setup to rotate the device in the gravitational field (1 = stepper motor RT 120 with the mounted (encapsulated) accelerometer, 2 = stepper motor RT 200, 3 = power supply TL 78, 4 = voltmeter Keithley 199 scanner, 5 = power supply Dr. K. Widmer)

(cooled/heated nitrogen) could be added. The whole setup and the data acquisition was computer controlled.

4.2.2 Dynamic Measurements

All devices were tested on a vibrating table in order to determine their dynamic characteristics. Additional optical measurements on the sensitive devices using a Mach-Zehnder interferometer [120] allowed us to determine the resonance frequencies, the modes of vibration and the displacement of the mass in function of the acceleration. For the optical detection, the sensor chip was mounted on a piezoceramic disc. Therefore only extremely small displacements and accelerations could be applied. In spite of the small, applied accelerations, the high resolution of the interferometer (in the order of Angströms) allows the determination of the amplitude of the movements of the mass. The mode of vibration was obtained by scanning the surface of the vibrating mass and thus finding the axis of rotation, which is characterized by its zero amplitude of displacement.

In contrast to the interferometer measurements, the accelerations on the vibrating table (Fig. 4.2) were large enough to produce a detectable output voltage change of the Wheatstone bridge. The system could be driven in two

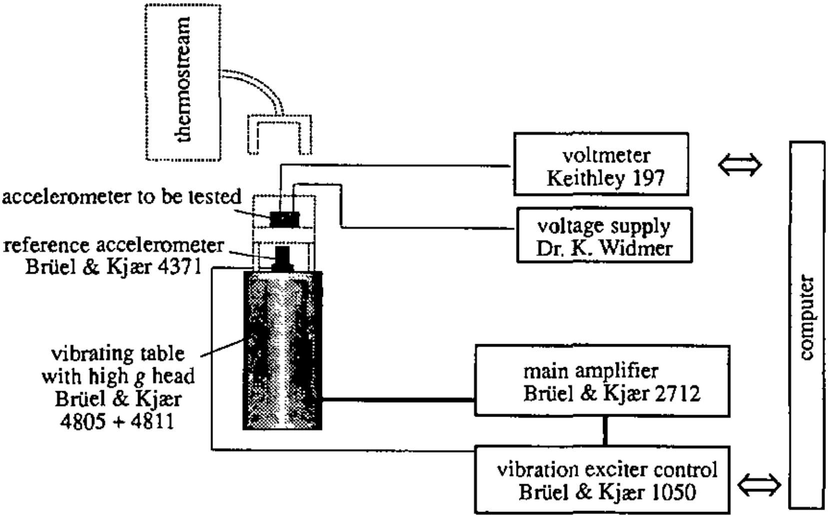

Fig. 4.2 Schematic drawing of the dynamic measurement setup

basic configurations, in a open or a closed loop configuration, respectively. In the latter case, a reference accelerometer mounted on the vibrating table fed back the vibration exciter control. This digital instrument allowed, for instance, scanning over the frequency range at constant acceleration. In the open configuration, the table could be excited by a noise source directly coupled onto the main amplifier. Thus the frequency response was given by the transfer function of the response of the reference accelerometer and the fabricated device. The reference accelerometer used was a piezoelectric Brüel&Kjær type 4371. Its frequency and acceleration range was 0.1 Hz - 12 kHz and 0.3 m*g* - 5100 *g*, respectively. The charge amplifier for the reference accelerometer was integrated into the preamplifier (Brüel&Kjær 1050). The vibrating table consisted of a Brüel&Kjær body type 4805 with a high *g* head 4811, which had a maximum acceleration of 65 *g* for a load of 200 g.

Nitrogen in the temperature range of -40° to 120°C, supplied by the Thermostream$^{®}$ system, and a thermally isolating cap were used to determine the temperature dependence of sensitivity and offset (see section 7.4). To avoid distortion of the exciter, the mechanical supports mounted on the table were fabricated as axissymmetric as possible, and in addition they had a high resonance frequency (> 10 kHz). At frequencies below 20 Hz, the amplifier could not guarantee a sinusoidal displacement of the vibrating table. So at very low frequencies in the closed loop configuration the output of the reference accelerometer and the sensor chip had to be individually measured using an oscilloscope. The whole apparatus and the data acquisition was computer controlled.

4.3 MOUNTING FOR CHARACTERIZATION

It is important to characterize the sensor chip before encapsulation in order to control the fabrication process and to determine the influence of the packaging. For these measurements the sensitive die was mounted in the following manner. Since accelerometers are very stress sensitive devices, only the side of the frame with the contact pads on it was glued on a Dual-in-Line package (DIL 24). Two small stripes of Kapton film tape No. 5413 with a thickness of 40 µm under two opposite sides of the accelerometer frame guaranteed the distance between the base of the DIL and the seismic mass. The glue was hardened at 120°C. Wire bonds connected the chip with the DIL 24 (see Fig. 4.3).

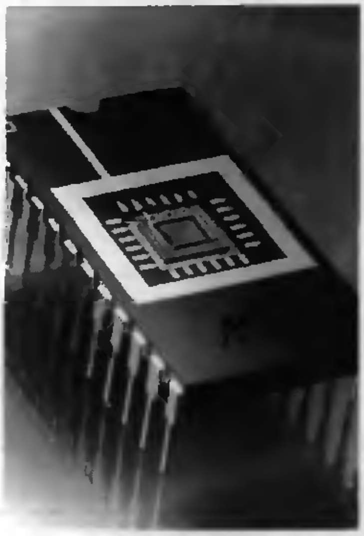

Fig. 4.3 Sensor chip mounted on a DIL 24

4.4 RESULTS AND DISCUSSION

The sensitive devices mounted as described above were characterized statically by turning them in the gravitational field and dynamically by using a vibrating table and the interferometer. All three different designs realized on 3 inch wafers, namely two bridge-type designs with two or four beams and a two-beam cantilever-type accelerometer were tested. All these devices had no passivation layer on their beams, since the grown oxide during the anneal of the piezoresistors was entirely etched away. Investigations on the influence of a passivation layer on the characteristics of the sensor chip will be presented below. Furthermore the back of the wafer was not protected by photoresist during plasma etching of the membrane. This missing protection which was added to the fabrication sequence of 4 inch wafers (process step 27 in Table 3.IV), caused the beams to be thinned from the back. This occured after the membrane was pierced through during plasma overetching and led often to beams of uncontrolled thickness. Due to inhomogeneities of the plasma process an increased variation of the beam thickness was observed compared to that expected from the electro-chemical etchstop. The results presented in Table 4.I were measured on devices having beams with a thickness of about 8.5 µm, less than the epitaxial layer thickness (12 µm). As the devices were undamped, special care was taken to avoid breakage during dynamic measurements. At resonance, the applied acceleration of the vibrating table was lowered by a factor of at least 10. Higher modes of vibration were determined electrically by measuring the changes of only one piezoresistor. The results of theoretical calculations and measurements are summarized in Table 4.I.

For the three different designs presented in Table 4.1, the four-beam bridge-type accelerometer has the lowest transverse sensitivity and highest first mode resonance frequency, whereas the cantilever-type is more sensitive but has a smaller usable frequency range. This shows well the trade-off between sensitivity and resonance frequency (see chapter 2). As the separation between the two beams on each side of the four-beam bridge-type accelerometer becomes larger, the second mode is harder to initiate (higher frequency) and

Table 4.I Comparison of calculated values based on analytical formulae and finite-element modeling with experimental data from manufactured devices (the units µV/V *g* refer to the output of a Wheatstone bridge per applied voltage and per terrestrial acceleration *g*)

	analytical formulae	finite element modeling [ANSYS]	measured data	
			vibrating table	interferometer
4 beam accelerometer :				
sensitivity	579 µV/V *g*	514 µV/V *g*	460 µV/V *g*	-
resonance frequencies:				
1. mode (transversal)	2810 Hz	2760 Hz	2520 Hz	2690 Hz
2. mode (rocking y)	-	4430 Hz	4120 Hz *	4370 Hz
3. mode (rocking x)	-	5700 Hz	5330 Hz *	5710 Hz
displacement per acceleration	31 nm/*g*	34 nm/*g*	-	40 ± 10 nm/*g*
2 beam accelerometer :				
sensitivity	638 µV/V *g*	533 µV/V *g*	530 µV/V *g*	-
resonance frequencies:				
1. mode (transversal)	2670 Hz	2470 Hz	2480 Hz	2320 Hz
2. mode (rocking y)	-	560 Hz	-	440 Hz
3. mode (rocking x)	-	5110 Hz	5170 Hz *	4850 Hz
displacement per acceleration	35 nm/*g*	37 nm/*g*	-	54 ± 14 nm/*g*
cantilever :				
sensitivity	1.68 mV/V *g*	1.41 mV/V *g*	1.19 mV/V *g*	-
resonance frequencies:				
1. mode (on an arc)	370 Hz	360 Hz	400 Hz	400 Hz
2. mode (rocking y)	-	6800 Hz	6960 Hz *	6920 Hz
3. mode (rocking x)	-	13420 Hz	-	14140 Hz

* measurements performed by connecting only one of the piezoresistors of the wheatstone bridge

hence the sensitivity in that direction decreases, which is highly desirable. The totally opposite case occurs when the two beams are brought completely together. This is the case of the two-beam accelerometer, with a second mode frequency that is lower than the first.

The difference in the optically and dynamically measured resonance frequencies is due to beam thickness variations in the devices fabricated on the 3 inch wafers. For example, a small variation in the thickness of the beams greatly affects both the sensitivity and the resonance frequency. With a beam thickness of 8.5 µm a small increase of 0.5 µm in the thickness of the beams changes the sensitivity values by 12% and the resonance frequency by 9%.

The main feature of the data presented in Table 4.I is that the values of the resonance frequencies and sensitivities calculated using analytical formulae are higher than the measured values. This may be because the analytical method assumes the ends of the beams to be clamped. In FEM analysis, however, the base of the chip was fixed, a boundary condition which corresponded rather closely to the experimental setup, and it can be seen that the values obtained using this technique are in better agreement with the observed values. The whole finite element simulation was done on a pure silicon structure.

As mentioned above the beams of the devices presented in Table 4.1 had not been passivated, since we expected that the stress which occurs at the interface between silicon dioxide and silicon [127-129] would greatly affect the performance of the sensor chip. In order to investigate the influence of passivation layers on the sensitivity and resonance frequency of sensor chips, different passivation layers were deposited on their beams. These devices were four-beam bridge-type accelerometers fabricated on 4 inch wafers with the process sequence described in subsection 3.4.3, e.g. these samples had a beams' thickness of 12.5 µm ± 0.4 µm silicon corresponding to the epitaxial layer thickness. The sensitivity and resonance frequency of devices which had no passivation on the beams, a 6000 Å thick thermal oxide or a 3000 Å thick plasma deposited Si_xN_y passivation layer are listed in Table 4.II. The samples of each passivation type were taken randomly from the same wafer. It can be seen that the passivation layer does not greatly affect the performance of the sensor chip, since the sensitivities are within the range 186 µV/V *g* ± 10%. The small standard deviation of the sensitivities proves the effectiveness of the electrochemical etch-stop and also of the protection of the back during the

Table 4.II Measured sensitivities of sensor chips of the 4 inch design with different passivation layers (four-beam bridge-type accelerometer) (mean values of 7 samples per passivation type)

passivation	mean sensitivity	standard deviation	resonance freq.
none	196 µV/V *g*	9 µV/V *g*	5000 Hz
therm. SiO_2	187 µV/V *g*	8 µV/V *g*	5000 Hz
PECVD Si_xN_y	174 µV/V *g*	4 µV/V *g*	5200 Hz

plasma etching of the membrane.

A typical static response of a four-beam bridge-type accelerometer of the 4 inch design can be seen in Figs. 4.4 and 4.5. The rotation around y resulted in the expected linear response whereas the rotation around x shows a hysteresis. This effect can be caused either by the cross-axis sensitivity or by a mounting error. Although our Wheatstone bridge configuration should compensate all cross acceleration as discussed in section 3.4.2, a cross-axis sensitivity can not be excluded a priori. Inhomogeneities of the resistors might affect the output, but the low offset of the bridge indicated a well controlled fabrication process. Thus a cross-axis sensitivity should be small. On the other side the measured hysteresis in Fig. 4.5 would correspond to an important transverse sensitivity of 2.3%. In addition, the hysteresis is mainly observed during rotation around x-axis. In that axis the mounting has no symmetry, since the device is only glued on one side and could either push that side up or pull it down after its hardening (see section 4.3). Indeed, if the surface of the chip deviates from the expected orientation, a hysteresis effect is measured. Furthermore, the horizontal starting position of the table was determined with respect to the metallic plate and consequently to the back of the DIL 24. Assuming the surface of the chip not parallel to the back of the DIL this procedure does not guarantee the right starting position. However, the angular error, which would correspond to the hysteresis in Fig. 4.5 was calculated and found a value of 1.32°. To see that the hysteresis can be eliminated the starting position was changed by 1.32° and the same device again rotated around x. The newly oriented sensor exhibited a linear response as can be seen in Fig. 4.6.

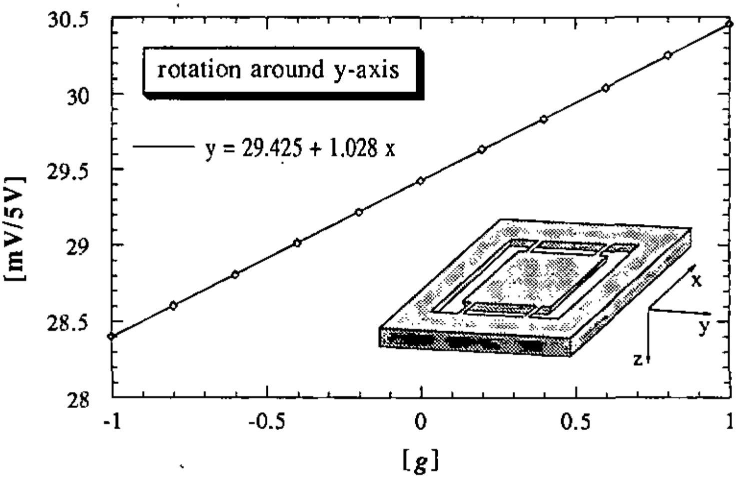

Fig. 4.4 Output of a four-beam bridge-type accelerometer rotated around y

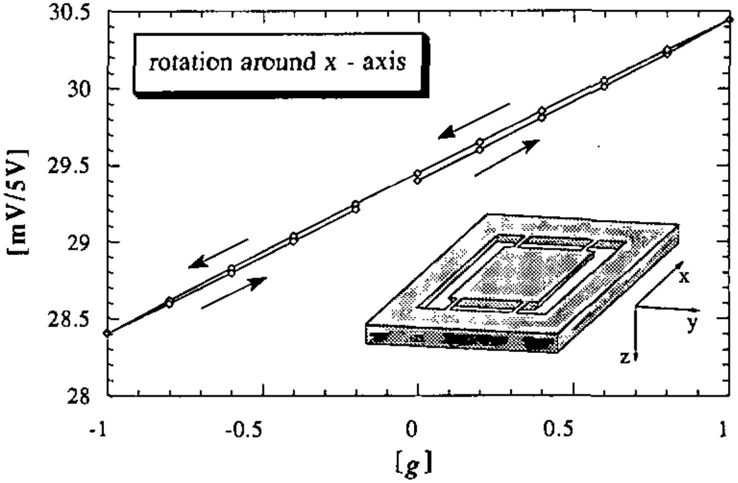

Fig. 4.5 Output of a four-beam bridge-type accelerometer rotated around x

We have calculated that a transverse sensitivity of 1.8% could be compensated by a mounting error of 1° or vice versa. However, the only means to determine the real cause of this hysteresis is to measure the starting orientation of the chip surface with a precision of better than 0.1°; a condition which could not be guaranteed by our mounting technique.

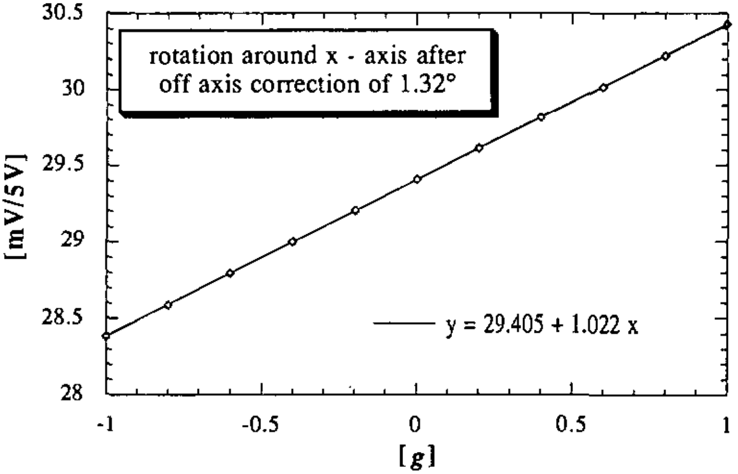

Fig. 4.6 Output of the same device as in Fig. 5.5 after an off axis correction of 1.32°

4.5 CONCLUSIONS

Relatively simple mass-beam configurations have been compared in Table 4.I, and the correspondence between theoretical predictions and measured values is within 18 %. The finite element modeling was in better agreement with the observed values than the analytical formulae. This may be because in FEM analysis the base of the chip was fixed, a boundary condition which corresponds rather closely to the experimental setup. This emphasizes the need for, and the powerful potential of, FEM analysis for detailed predictions of the characteristics of silicon micromachined structures, although analytical formulae allow the dependence of the characteristics on the device dimensions to be clearly seen. Since the mechanical transverse sensitivity should be kept as low as possible, the four-beam bridge-type accelerometer design is more advantageous than the two-beam device. In addition these measurements have shown the importance of the most critical fabrication parameter, the thickness of the beams. Therefore the electrochemical etch-stop and the protection of the back during plasma etching of the membrane are mandatory for reproducible characteristics.

The small standard deviation of the sensitivities on samples from the 4 inch design, where the back of the beam had been protected during plasma etching, have proven the effectiveness of the electrochemical etch-stop. Devices with thermal oxide, plasma silicon nitride or without any passivation layer on the beams exhibited quite similar sensitivities and resonance frequencies. Thus their influence on the characteristics is quite small. The variation of the measured data might not only be due to the passivation layer but also to the different thicknesses of the wafer and epitaxial layers.

The static measurements have shown that not only a cross sensitivity but also a small mounting error can cause a hysteresis-like response. The measured hysteresis is thought to be caused by a mounting error, since cross-axis sensitivity is theoretically electrically compensated. The chosen mounting technique was not accurate enough to guarantee parallelism of the chips surface to the Dual-In-Line package and thus to exclude the possibility of a badly aligned sensor chip.

In order to control the fabrication process these measurements were done on non encapsulated devices. Although the distance between the seismic mass and the DIL socle was only 40 μm, the air film did not damp the device at all. In the next two chapters different encapsulation techniques and parameters which determine the damping are discussed.

Chapter 5
Aspects of Damping

Every accelerometer sensor chip is a resonant structure and therefore has to be damped in order to increase its useful frequency range. This is mostly achieved by enclosing the moving mass into a small cavity. As a damping medium either liquid or gas layers can result in a flat response over a wide frequency range. The viscosity of the damping fluid as well as the thickness of the damping layer determine the damping characteristics. In section 5.2 the previously published damping and encapsulation methods for accelerometers are summarized. Since all the damping methods are mainly based on viscous damping, the main formulae are summarized in section 5.3. In the following sections the consequences of liquid and gas damping are discussed. The theory of squeeze film damping is applied for both types of damping in order to describe the dynamic response.
Parts of this chapter have been published in [130, 131].

5.1 INTRODUCTION

Damping of proof mass oscillations is a fundamental consideration in the design of accelerometers, because it is needed to achieve a flat response over a wide frequency range. A common way to damp an accelerometer is to enclose the sensitive device entirely in a small cavity by bonding (preetched) wafers to both sides of the sensor chip. This encapsulation technique creates on both sides of the moving seismic mass thin layers of the damping fluid. When two plates in close proximity and with a fluid trapped in between approach one another pressures are developed which resist the motion of the surfaces to come together. The resulting pressure forces are sometimes called "squeeze" forces. Thus the thin layers provide damping through viscous dissipation. Not only the thickness of the damping layer but also the viscosity of the fluid determine the damping. Either liquids or gases can be used to achieve critical damping of the accelerometer, but their influence on the static, dynamic and temperature behaviour are quite different.

Since thin damping films are very important the squeeze film theory will be applied to silicon accelerometers and developed for gases and liquids. Based on that theory and on the characteristics of our sensor chip it will be shown that both damping mediums display a viscous damping behaviour. Therefore the main formulae of a viscous damped spring mass system are recapitulated in section 5.3. In its second part the temperature and pressure dependence of the viscosities of these fluids are shown.

The influence of liquid damping on the static and dynamic performance of an accelerometer is quite different to that of a thin gas layer. Thus for both damping mediums the effects on the characteristics are separately discussed in sections 5.4 and 5.5. In addition the loss of sensitivity and the shift of the resonance frequency of liquid-damped devices are explained.

Further requirements of the encapsulation and also already published damping and encapsulation methods of accelerometers are described in section 5.2. The technological background of the encapsulation is given in chapter 6, where different mounting methods are discussed. In addition, the formulae developed in this chapter allow the cavity size required for critical damping to be calculated for both oil and air-damped accelerometers. In chapter 7 these calculations are done and compared to the measured performance.

5.2 ENCAPSULATION AND DAMPING

In general, sensor packaging has to deliver reliable, economical and application-oriented solutions by choosing optimal technologies and material combinations. Unlike integrated circuits, silicon sensors must operate in harsh environments such as humidity, salt-water, body fluids, fuels, hydraulic fluids and gases. While the classic IC package seeks to isolate and hermetically separate the chip from the environment, the sensor package must appropriately protect the die while transmitting the mechanical force to the sensor. Thus the prime goal of the packaging technology is to provide good transfer of the mechanical variable of interest from the environment to the sensor whilst eliminating the effects of environmental contaminants and corrosives. Typically, the sensor is interfaced to a force through the use of an appropriate mechanical fitting, tubulation or other connection. The sensor package must incorporate convenient low cost means for such interface while isolating the very sensitive silicon die from undesirable mechanical stresses. While modem silicon sensors incorporate calibration and compensation on the silicon chip itself, often analog or active compensation employing hybrid or component resistors are used. The package must provide appropriate means of incorporating and protecting these additional components.

The special requirements for the packaging of silicon accelero-meters are

Table 5.I Requirements for the encapsulation of silicon accelerometers

- protection from the environment
- economical mounting, interconnection and packaging techniques
- interference free mounting, interconnection and packaging techniques
- critical damping of the device
- protection against overload
- integration of a confidence checking on the device

given in Table 5.I. To keep the price of the end product low, the encapsulation has to be either a batch process or fully automated. As an accelerometer is a spring mass system, it needs to be (critically) damped in order to avoid breakage and to increase its useful bandwidth. Damping of the structure is determined by the viscosity of the damping fluid as well as by the size of the cavity in which the seismic mass is enclosed. The cavity is often realized by bonding two wafers to both sides of the sensitive element. The different characteristics of several bonding methods are discussed in section 6.2. The bonding technique has to be chosen to give a low temperature sensitivity to the mounting. Furthermore the encapsulation should be as stress-free as possible because an accelerometer is an extremely stress sensitive device.

Additionally, the overforce protection can be integrated as mechanical stoppers in the cavity. Since the distance between the electrodes (e.g. mass and cap) of a capacitive accelerometer is of several microns, the counter electrodes become at the same time the stoppers against overload. Due to the extremely small cavity's size, the air pressure of critically air-damped capacitive accelerometers needs to be reduced to some Torr's. Moreover since no electrode is needed in the cavity of piezoresistive accelerometers, the cavity can be increased to achieve critical damping with gas at atmospheric pressure. Liquids may also be used for damping the sensitive element. Unfortunately their viscosity shows a much higher temperature-dependence than gases, and additionally the buoyant force, which acts on the vibrating structure immersed in the liquid, leads to an important loss of sensitivity.

A variety of encapsulation techniques have been used with piezoresistive accelerometers. In 1977 Roylance [25] anodically bonded pre-etched pyrex-glass on both sides of the sensitive element to create a 70 μm deep cavity. No mechanical stoppers were integrated. Since due to the size of the cavity, air damping was insufficient, Roylance filled the cavity with liquids which critically damped the device at room temperature. Honeywell [132] used the same glass-Si-glass sandwich for the encapsulation of their g-switch. This mounting technique is advantageous because the glass plates are transparent which facilitates wafer to wafer alignment. Tsugai et al. from Mitsubishi [29] published a sensitive device mounted on a thin layer of a damping material, which partly filters the unwanted frequency range. Nakamura et al. from Nissan Motor Co. [30] presented at Transducers' 87 a silicon-silicon-silicon sandwich in a ceramic package with oil as a damping material.

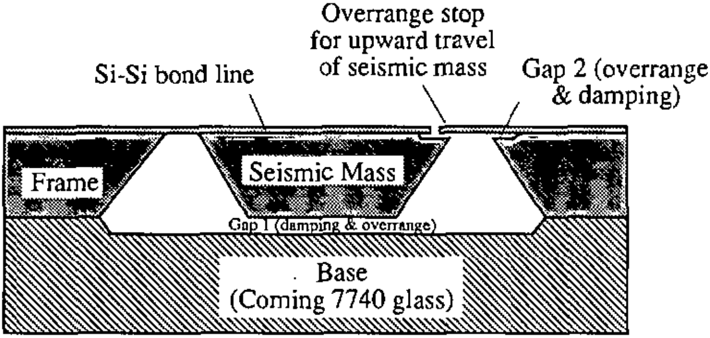

Fig. 5.1 Schematic cross-section of an encapsulated cantilever-type accelerometer as proposed by NOVA Sensor [6]

The only two successfully commercially realized encapsulations are those proposed by Nova Sensor [6] and ICSensors [133]. Nova Sensor (see Fig. 5.1) incorporated the overrange stops directly into the sensor at the wafer level. The overrange protection in this chip is provided by a series of interdigitated tabs which extend over underlying shelves, and prevent the mass from moving upward past a preset limit. Similarly, a tab on the seismic mass extending over a shelf on the supporting frame prevents the mass from moving downward past a preset limit. The tabs itself are thin enough to be somewhat flexible, so that they do not shatter when they hit the stopping shelf. The damping is realized by air (squeeze film) using controlled gaps in the chip structure. Beneath the seismic mass, the gap between the glass base and silicon constitutes one air-damping area (Gap 1) whilst the gap between the overrange protection elements constitutes another (Gap 2), as is shown in Fig. 5.1.

The ICSensors design is based on a hermetically sealed cavity (Si-Si-Si) with small air-gaps for critical damping of the device and integrated overforce stops (Fig. 5.2). The bonding between the three different silicon wafers is (probably) achieved by an eutectic metal bond. In addition ICSensors proposed a self test configuration [36,134] which allows the verification of the function of the accelerometer without subjecting it to dynamic acceleration loads. It is very important to check the operation of a device in many high reliability applications such as automotive safety and munitions. A unique feature of silicon accelerometers is the relatively ease by which the light mass can be deflected with small electrostatic forces. This feature has been implemented on the accelerometer package shown in Fig. 5.2. A voltage is applied between the mass and the top cap which in turn causes the mass to deflect upward. Because

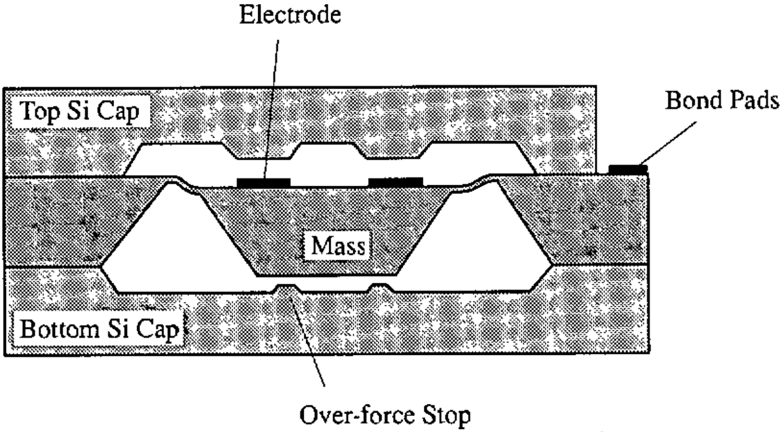

Fig. 5.2 Schematic cross-section of an encapsulated bridge-type accelerometer as published by ICSensors [36]

the gap is accurately controlled and because the mass cannot differentiate between force due to acceleration and force due to electrostatics, it is possible to both verify that the mass is free by moving and to calibrate the device in the field repeatedly and/or over a temperature range. The piezoresistive sensor has typically a negative temperature coefficient of sensitivity (TCS) (i.e. sensitivity decreases as temperature increases) and fairly complex compensation algorithms have been developed to provide a temperature independent sensitivity (see section 7.4). The self-test capability allows confirmation that the sensitivity has changed. Further by taking the ratio of the sensitivity measured versus the sensitivity under self-testing, the sensor system can be compensated for temperature changes giving a reduction in temperature sensitivity of a factor of 10 to 20. The self-test feature also allows scanning of the part at wafer-level probing to determine sensitivity and thereby reduces the cost of manufacturing.

5.3 VISCOUS DAMPING

The squeeze film theory, described in the next two sections, applied to our accelerometer design will show that for both gas and liquid films the damping force is proportional to the velocity of the moving body (= $c\dot{x}$). This condition is called viscous damping. In order to calculate the cavity size for critical damping with both damping fluids the main and well-known characteristics of a viscous damped spring - mass system are recapitulated in this section. Based on these basic formulae and on the squeeze film theory the cavity size will be calculated in chapter 7 and compared to measured devices.

The differential equation of motion for forced vibrations of a viscous damped spring - mass system is

$$m\ddot{x} + c\dot{x} + kx = Q\cos(\omega t) \tag{5.1}$$

where k = spring constant, c = coefficient of viscous damping, m = mass, Q = amplitude of the forced vibration, ω = angular velocity of the forced vibration.

Since the development of the solution can be found in many fundamental books on mechanics (see e.g. [80] or [135]), we will only discuss the solution of eq. 5.1.

The general solution of eq. 5.1 is

$$x = e^{-dt}\,(C_1 \cos p_d t + C_2 \sin p_d t) \tag{5.2}$$

where $b^2 = \frac{k}{m}$, $d = \frac{c}{2m}$, $p_d{}^2 = b^2 - d^2$, C_1 and C_2 are constants determined from the initial conditions.

A particular solution of eq. 5.1 is

$$x = \frac{Q}{k}\,\beta\cos(\omega t - \theta) \tag{5.3}$$

in which β is the magnification factor, θ the phase angle and γ the damping ratio given by

$$\gamma = \frac{d}{b} = \frac{c}{2\sqrt{km}} \tag{5.4}$$

$$\beta = \frac{1}{\sqrt{\left(1 - \omega^2/b^2\right)^2 + (2\gamma\omega/b)^2}} \tag{5.5}$$

$$\theta = \tan^{-1}\left(\frac{2\gamma\omega/b}{1 - \omega^2/b^2}\right) \qquad (5.6)$$

The total solution of eq. 5.1 is obtained by adding the particular solution (eq. 5.3) to the general solution (eq. 5.2). The general solution represents damped free vibrations, whereas the particular solution represents damped forced vibrations. The free vibrations have a frequency p_d, whereas the forced vibrations have a frequency ω, which is identical to the period of the disturbing force that produces them. We see that due to the factor e^{-dt} the free vibrations gradually subside, leaving only the steady forced vibrations represented by the particular solution. Thus, we see that steady-state forced vibration with viscous damping is a simple harmonic motion having constant amplitude $\beta\, Q/k$, phase angle θ and period $^{2\pi}/_{\omega}$.

We see from eq. 5.3 that the amplitude of the steady-state forced vibration is obtained by multiplying the static-load displacement Q/k by the magnification factor β. This factor depends not only upon the frequency ratio ω/b, but also upon the damping ratio γ. Figure 5.3 shows the magnification factor β plotted against the ratio ω/b for various levels of damping. From these curves we see that when the impressed angular frequency ω is small compared with the natural angular frequency b, the value of the magnification factor is not greatly different from unity. Thus, during vibration the displacements x of the suspended mass are approximately those which would be produced by the static

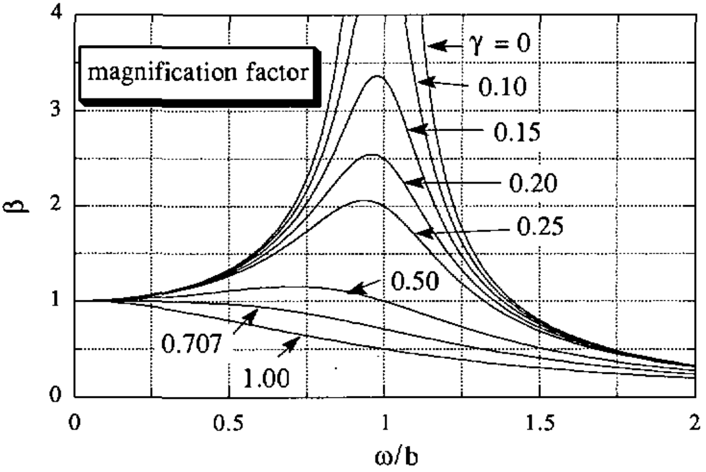

Fig. 5.3 Magnification factor β plotted against the ratio ω/b for various levels of damping

action of the disturbing force Q cos ωt. When ω is large compared with b, i.e. when the impressed frequency is much greater than the natural frequency, the value of the magnification factor tends toward zero, regardless of the amount of damping. This means that a high-frequency disturbing force produces practically no forced vibrations of a system that has a low natural frequency. In both extreme cases ($\omega \ll b$ and $\omega \gg b$) we note that damping has only a secondary effect on the magnitude of the magnification factor β. Thus, in these two cases of forced vibrations it is justifiable to neglect the effect of damping entirely and to use the equations of an undamped system.

As the value of ω approaches that of b, i.e. as ω/b approaches unity, the magnification factor grows rapidly, and its value at or near resonance is very sensitive to changes in the amount of damping. It will also be noted that the maximum value of β occurs for a value of ω/b slightly less than unity for $\gamma > \sqrt{2}/2$. Setting the derivative of β with respect to ω/b equal to zero, we find that the maximum β occurs when

$$\frac{\omega}{b} = \sqrt{1 - 2\gamma^2} = \sqrt{1 - \frac{c^2}{2mk}} \qquad (5.7)$$

If $\gamma = \sqrt{2}/2$, the system is called critical damped and β becomes maximal for $\omega = 0$, i.e. the magnification factor is ≤ 1 for any frequency. For $\gamma > \sqrt{2}/2$ the spring mass system is overdamped, for $\gamma < \sqrt{2}/2$ it is under damped.

The phase relationship between the steady-state vibrations and the disturbing force is represented by the phase angle θ in eq. 5.3. The curves in Fig. 5.4

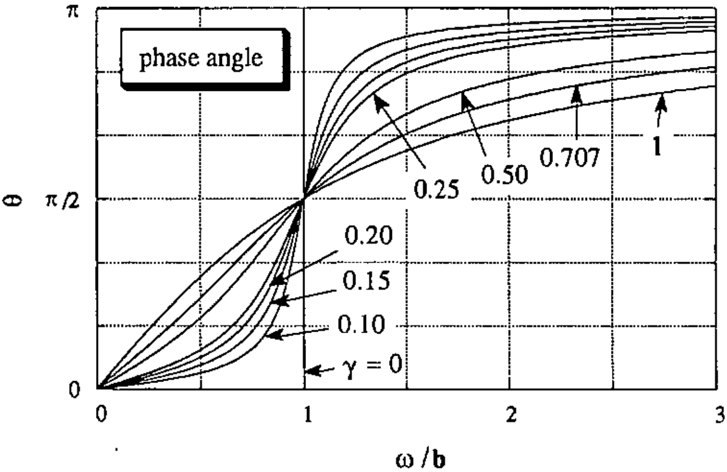

Fig. 5.4 Phase angle θ plotted against the ratio ω/b for various levels of damping γ

show the variation in the phase angle θ with the ratio ω/b for several levels of damping γ. When damping is present, we note a continual change in θ as the ratio ω/b increases. Also, regardless of the amount of damping, we find θ = π/2 at resonance. For values of ω/b either well below or well above resonance, we see that a small damping ratio has only a secondary effect upon the phase angle. That is, well below resonance the angle θ is practically zero, while well above resonance it is practically π.

The encapsulation of an accelerometer aims to achieve critical damping (realized by the cavity's size and viscosity of the damping fluid) since such devices exhibit the widest, usable frequency range. The moving seismic mass of an accelerometer feels a damping force proportional to the fluid's viscosity (see sections 5.4 and 5.5). Hence the damping characteristics depend on pressure and temperature.

Basically two viscosities can be distinguished:

a) dynamic viscosity η [Pa s]
b) kinematic viscosity ν [m^2/s], defined as the dynamic viscosity divided by the density, e.g. $\nu = \eta/\rho$, where ρ = density.

Temperature dependence of the viscosity :

The dynamic viscosity of liquids decreases with increasing temperature due to the temperature dependence of the intramolecular adhesion forces, which act between the different liquid particles. However, the dynamic viscosity of gases and vapors increases with increasing temperature, because the impulse exchange between the molecules increases with increasing temperature (see Fig. 5.5). There are no formulas for the description of the viscosity's temperature dependence, only some empiric have been proposed [136]. Furthermore the viscosity in liquids is in general more temperature dependent than in gases (compare Fig. 5.6 with Fig. 5.7).

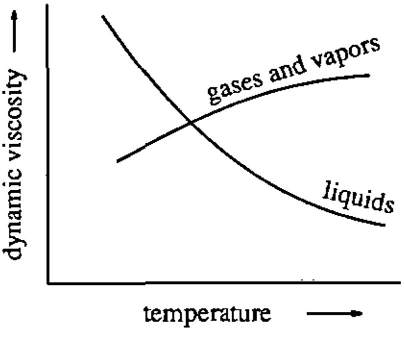

Fig. 5.5 Temperature dependence of the viscosity

Pressure dependence of the viscosity :

The pressure dependence of the dynamic viscosity is only noticeable at high pressures. Fluids, whose dynamic viscosity has a high temperature dependence, show in general an important pressure dependence. For most liquids, the dynamic viscosity increases nearly exponentially with the pressure. The viscosity of gases is pressure independent, if the mean free path of a molecule

is small compared to the distances of the moving body in the gas.
Figures 5.6 and 5.7 show the kinematic viscosity of several liquids and the dynamic viscosity of air, respectively, for different temperatures and pressures.

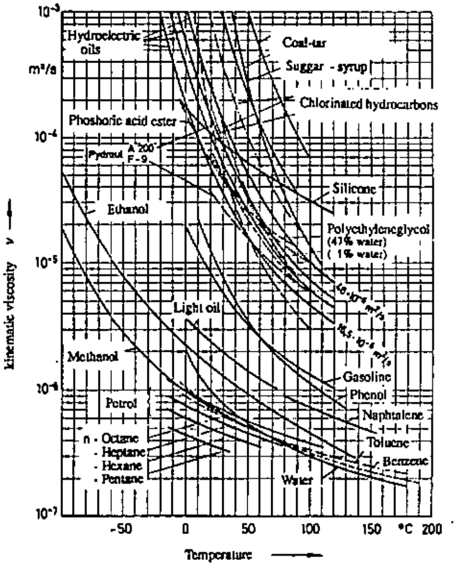

Fig. 5.6 Kinematic viscosity of several liquids [136]

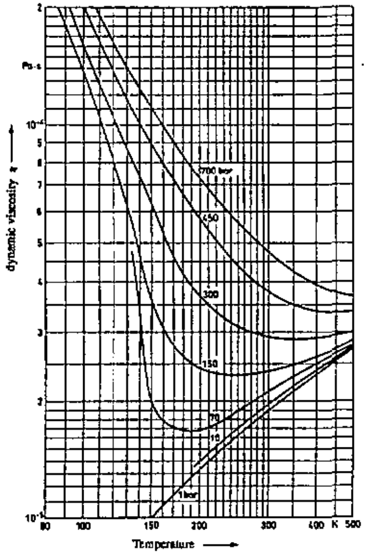

Fig. 5.7 Dynamic viscosity of air [136]

5.4 LIQUID-DAMPED ACCELEROMETER

The characteristics of an accelerometer sensor chip immersed in a liquid compared to the device in vacuum are quite different. The sensitivity of the sensor in the liquid is lowered due to the buoyant force acting on the seismic mass. The dynamic response is affected by two facts:

- The damping coefficient of the "squeezed" liquid film depends on the viscosity of the liquid, on the size of the moving mass and of the "squeeze film" thickness. Thus the **size of the cavity,** the **liquid's viscosity** and its **temperature dependence** determine mainly the damping characteristics of a liquid-damped accelerometer.
- The **resonance frequency is much lower** compared to the undamped device, which is due to
  - buoyancy
  - added mass
  - viscous damping.

5.4.1 Static Response

The static behaviour of a silicon accelerometer immersed in a liquid is changed in comparison to a device in vacuum, because the effective mass is lowered due to the buoyant force. This leads to a reduction of sensitivity. The resulting ratio of the sensitivity in a liquid to that in vacuum is proportional to $(\rho_{si} - \rho_{liquid})/\rho_{si}$, which is for most liquids about 60%. In gas this effect is neglectable as the gas' density at ambient pressure is much less than one tenth of a percent of that of silicon.

5.4.2 Dynamic Response

In the first part of this subsection the moving seismic mass of the accelerometer in close proximity to an underlying cap having a thin layer of liquids squeezed between them will be approximated by two moving plates with an incompressible film squeezed in between. The damping force is calculated for this setup based on the squeeze film formulae developed by Blech [139]. In the second part, the causes of the resonance frequency shift of a liquid damped accelerometer compared to the device in vacuum are explained.

Incompressible squeeze film :
To our knowledge the only work applying the theory of squeeze film to the design of the damping of accelerometers has been published by J. Starr from Honeywell in 1990 [137]. He discusses the limitations of the application of the squeeze film formulae and compares the results with finite element modeling. This work is based on the article published by Langlois on isothermal squeeze films [138]. In this section we recapitulate the main formulae of the squeeze film theory as published by J. Blech [139, 140]. This rough approach allows the viscous damping force to be seen as well as the cavity size needed for critical damping to be calculated (see chapter 7).
An oil-encapsulated accelerometer has a very thin layer of liquid "squeezed" between its seismic mass and the cavity. When the device is exposed to any acceleration the seismic mass approaches the cavity. Thus forces are developed which resist the motion. The equation governing the pressure distribution in the fluid is the well known Reynolds equation. To solve the equation, the following assumptions are taken :

- laminar flow
- isothermal process
- most of the motion perpendicular to the plates' surfaces.

When the motion is of the nature just described above, this equation reduces to the form [141] :

$$\frac{\partial}{\partial x}\left(\frac{\rho\, h^3}{12\,\eta}\frac{\partial p}{\partial x}\right)+\frac{\partial}{\partial y}\left(\frac{\rho\, h^3}{12\,\eta}\frac{\partial p}{\partial y}\right)=\frac{\partial}{\partial t}(\rho\, h) \tag{5.8}$$

with h = film thickness, p(x,y) = pressure, ρ = density and η = dynamic viscosity.

For an incompressible fluid (ρ = constant), eq. 5.8 reduces to :

$$\frac{\partial}{\partial x}\left(h^3\frac{\partial p}{\partial x}\right)+\frac{\partial}{\partial y}\left(h^3\frac{\partial p}{\partial y}\right)=12\,\eta\,\frac{\partial h}{\partial t} \tag{5.9}$$

We define the ambient pressure as the zero pressure level. Thus, the boundary condition for eq. 5.9 is :

$$p = 0 \quad \text{on the plate boundary} \tag{5.10}$$

Consider two rectangular flat parallel plates having length l and width w as shown in Fig. 5.8. The plates are moving one towards the other in a squeeze motion. Equation 5.9 reduces to :

$$\frac{\partial^2 p}{\partial x^2}+\frac{\partial^2 p}{\partial y^2}=-\frac{12\,\eta}{h^3}\frac{\partial h}{\partial t} \tag{5.11}$$

For the setup shown in Fig. 5.8, the boundary conditions are :

$$p\left(\pm\frac{l}{2}, y\right)=0 \ \text{ and } \ p\left(x, \pm\frac{w}{2}\right)=0 \tag{5.12}$$

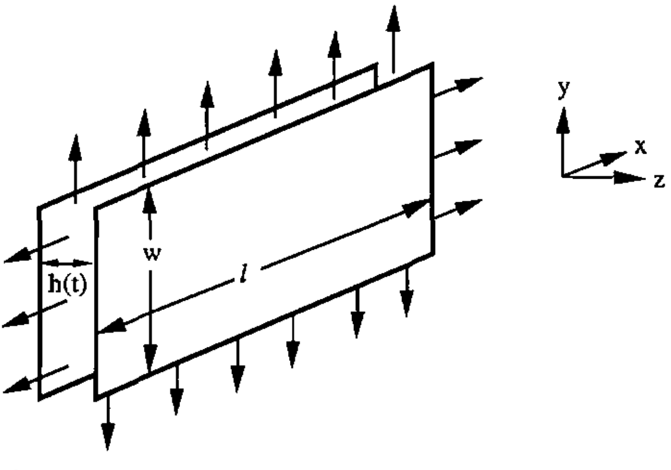

Fig. 5.8 Parallel plate, rectangular squeeze film damper

Equation 5.11 has the following solution which fulfills the boundary conditions of eq. 5.12 [139]

$$p(x,y) = \frac{3}{2}\frac{\eta\, l^2}{h^3}\frac{\partial h}{\partial t}\left(\frac{32}{\pi^3}\sum_{m\,\mathrm{odd}}\frac{(-1)^{1/2(m-1)}}{m^3}\left(1-\frac{\cosh\left(m\pi\frac{y}{l}\right)}{\cosh\left(\frac{m\,\pi\,\alpha}{2}\right)}\right)\cos\left(m\pi\frac{x}{l}\right)\right) \tag{5.13}$$

where $\alpha = \frac{w}{l}$.

The force acting on each surface is obtained from the integration of the pressure over the plate area, which yields an expression for the force F:

$$F = F_\infty\, \kappa_s\, \frac{\partial h}{\partial t} = c_{lsq}\, \frac{\partial h}{\partial t} \tag{5.14}$$

where F_∞ is the pressure force on an infinitely wide plate ($l \ll w$). F_∞ and κ_s are given by :

$$F_\infty = \frac{\eta\, l^3\, w}{h^3} \tag{5.15}$$

$$\kappa_s = \left(1 - \frac{192}{\alpha\,\pi^5}\sum_{m\,\mathrm{odd}}\frac{\tanh\left(\frac{m\pi\alpha}{2}\right)}{m^5}\right) \tag{5.16}$$

The factor κ_s is plotted versus α in Fig. 5.9. This factor is less than unity for

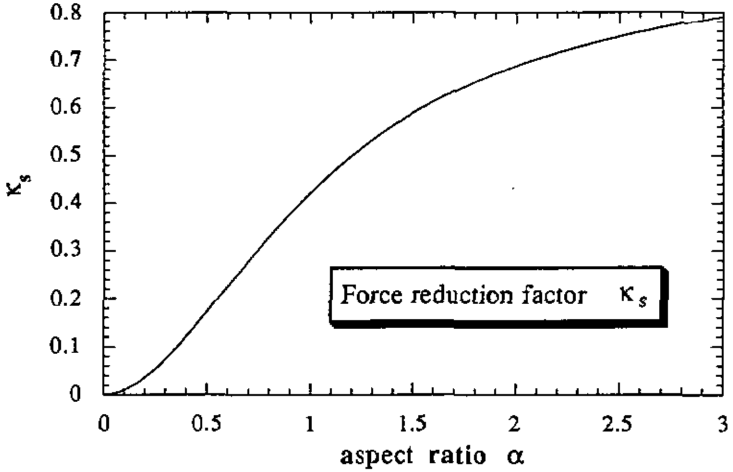

Fig. 5.9 Force reduction factor κ_s in function of the plate aspect ratio α for incompressible squeeze film

any width to length ratio and tends to unity when the plate width tends to infinity. Thus κ_S can be thought of as a force reduction factor in the case of the infinitely wide plate. This behaviour of κ_S is clear since finite plates posses more fluid escape area than infinite strips, thus the resistance to out-flow of fluid is smaller, resulting in a smaller damping capacity.

Equations 5.14 and 5.15 show the temperature dependence of the liquid damping. It depends linearly on the viscosity changes as a function of temperature.

Equation 5.14 clearly indicates that the damping force is proportional to the velocity of the moving plate. Thus we conclude that an oil-damped accelerometer behaves like a viscous damped spring - mass system. In section 7.2 the squeeze film thickness for a critically oil-damped accelerometer is calculated based on these formulae.

Shift of the resonance frequency:

Let us consider the causes and influences of the resonance frequency's shift mentioned above in more details :

1. The effective mass is lowered due to the buoyant force, as explained above. Since a piezoresistive accelerometer acts like a mass-spring system, its resonance frequency is inversely proportional to the square root of the mass. Assuming a reduced effective mass of 60% this would lead to an increase of the resonance frequency by a factor of about 1.3 compared to the undamped device.
2. We follow the development as proposed by Blevins [142] for the effects of a vibrating structure in a fluid. As the seismic mass accelerates, the fluid surrounding the structure must accelerate as well. The inertia of the entrained fluid is the added mass. The primary effects of the surrounding oil on the vibrations of a symmetric structure in a still fluid are the increase of the effective mass and the damping of the structure. Therefore added mass always decreases the natural frequency of the structure compared to that of a structure measured in a vacuum. The importance of added mass in the dynamic analysis of a particular structure can be estimated from the ratio of the density of the surrounding fluid to the average density of the structure. Since the density of oil is about one third of the density of silicon, added mass plays a large role in the dynamic analysis of oil-encapsulated microstructures. Experiments have generally shown [142], that the added mass of a structure vibrating in a still fluid is a function of
   - the geometry of the surface of the structure, including the geometry and relative position of proximate structures and the location of the free surface
   - the amplitude and direction of vibration and

- a Reynolds-number-like parameter

$$m^*_{\text{still fluid}} = \rho\ F\left(\text{geometry}, \frac{Q}{D_o}, \frac{f\ D_o^2}{\nu}\right) \tag{5.17}$$

where ρ is the density of the fluid, Q is the amplitude of vibration in a given direction relative to the structure, D_o is a characteristic diameter, f is the frequency of vibration, and υ is the kinematic viscosity of the fluid.

It can be shown that added mass, unlike fluid drag or fluid damping, can exist in an incompressible, inviscid, irrotational fluid (i.e. ρ = constant, υ = 0) [142]. This opens the possibility of evaluating added mass through the mathematical application of potential flow theory. The added mass which is predicted from potential flow theory depends only on the geometry of the structure's surface :

$$m^*_{\text{potential flow}} = \rho\ F\left(\text{geometry}, f\right) \tag{5.18}$$

Comparison of experimental and theoretical results [143, 144] suggests that the potential flow theory prediction is within about 10% of the experimentally measured value if the Mach number of the oscillation is small, if the amplitude of vibration is small compared with a characteristic diameter of the structure and if the Reynolds-number-like parameter is large i.e. :

$$\frac{Q\left(2\pi f\right)}{c_s} << 1 \tag{5.19}$$

$$\frac{Q}{D_o} < 1 \tag{5.20}$$

$$\frac{2\pi f D_o^2}{\nu} > 10\,000 \tag{5.21}$$

where c_s is the speed of sound in fluid.

These three conditions are fulfilled in the case of the liquid-damped silicon accelerometer.

For a rectangular plate accelerated transversely in a incompressible fluid, the virtual mass is given by [145]

$$m^* = \frac{1}{4}\rho\ \pi\ l\ w^2 \tag{5.22}$$

with w and l being the width and length of the plate respectively.

3. For the calculation of the added mass, we assume an ideal fluid, i.e. without friction. As most liquids are viscous, we have to take into account the effect of the viscous damping on the resonance frequency. Viscous damping theory [146, 147] indicates that a damping force, which is proportional to the velocity of the mass, lowers the resonance frequency by

$$\frac{f_{res}(\text{liquid})}{f_{res}(\text{vacuum})} = \sqrt[4]{1-1/\beta^2} \tag{5.23}$$

   where f_{res} is the resonance frequency and β is the magnification factor. The magnification factor is defined as the ratio of the sensitivity at the resonance frequency to the DC sensitivity.

A combination of these three effects mainly influences the resonance frequency of a liquid-damped accelerometer. In section 7.2 the theoretically expected shift of an oil-damped accelerometer, based on these formulae, will be compared to the measured value.

5.5 GAS-DAMPED ACCELEROMETER

Instead of liquid damping, an accelerometer, which is basically a spring-mass system, may also be damped by a very thin gas layer. Fortunately, micromachining is well controllable so facilitating the formation of very thin fluid layers that serve as an excellent means of viscous dissipation, even when the fluid medium is a gas. The extent of damping becomes less temperature dependent because of the smaller relative change in viscosity of gases compared to liquids. A typical cross section of an air-damped accelerometer is shown in Figs. 5.1 and 5.2. As for the liquid-damped accelerometer we approximate again the seismic mass in close proximity to the cap as two rectangular plates moving one with respect to the other. Based on the formulae of a compressible squeeze film as published by J. Blech [139] we will calculate the spring and viscous damping forces of a thin air-film for our fabricated accelerometer. The theory will show that the spring force is neglectable compared to the viscous damping force. In subsection 7.3.1 the theoretically expected dynamic response will be compared to that of some measured devices. In addition the cavity size for critical damping is calculated using the formulae developed in this chapter.

In contradiction to an accelerometer immersed in a liquid, the buoyant force acting on the device in gas is neglectable, since the density of gas at ambient pressure is less than one tenth of a percent of that of silicon. Thus the sensitivity is not reduced compared to a device in vacuum.

For the development of formulas for better understanding of the damping effects of a very thin gas layer, we consider a compressible fluid which is squeezed between two plates moving one with respect to the other (see Fig. 5.8). If film conditions are steady, the momentum equations may be combined with the continuity relation, to give the Reynolds equation, a single differential equation relating pressure, density, surface velocities and film thickness. The combination of momentum and continuity equations allows the distributed film velocity to be eliminated and replaced by the film surface velocities. Unless slip is present, these velocities are identical to the velocities of the adjacent surfaces. Slip flow (i.e. a difference between surface velocity and average fluid velocity at the surface) can become important only with gas films. The Knudsen number, $Kn = \lambda/h$ (where λ is the mean free molecular path and h is the film thickness), is a measure of the average number of molecular collisions in a given length. When $Kn < 0.01$, flow may be treated as a continuum; when $0.01 < Kn < 15$, slip flow becomes significant, and for $Kn > 15$ fully developed molecular flow results. The mean free path of air molecules at room temperature and atmospheric pressure is about 0.07 µm. Thus for a film thickness of < 7 µm, slip-flow is not quite negligible. Recall that the molecular mean free path varies inversely with pressure. As the measurements on air-damped (air at 1 bar) accelerometers have shown that the squeeze film thickness is greater than 10 µm, the flow can be treated as a continuum.

To solve the Reynolds equation, the following assumptions are taken :

- The surfaces of the plates are substantially parallel and most of the motion is perpendicular to the plates' surfaces.
- The gas flow between the plates is assumed to be laminar and primarily viscous. This assumption implies low Reynolds numbers and parabolic velocity distributions across the gas film.
- The relationship between pressure p and density ρ at any point in the gas film is assumed to be described by a polytropic process with exponent n: i.e. $\frac{p}{\rho^n}$ = constant (since in our case the film is (nearly) isothermal, we assume $n \approx 1$).
- The separation h of the plates is very small compared with the linear dimensions of the plates.
- The variation of plate spacing is assumed to be small compared with the mean spacing h_o

$$h = h_o + e \text{ where } e << h_o.$$

When the motion is of the nature just described above, we get from eq. 5.8 using the third assumption in order to eliminate ρ (see eq. 1.49 in Ref. [138] or eq. 2.6.10 in Ref. [141])

$$\frac{h^3}{12\,\eta}\left(\frac{\partial}{\partial x}\left(p\,\frac{\partial p}{\partial x}\right)+\frac{\partial}{\partial y}\left(p\,\frac{\partial p}{\partial y}\right)\right)=\frac{\partial}{\partial t}(p\,h) \tag{5.24}$$

where p = pressure, h = film thickness, t = time and η = fluid viscosity.
The boundary condition for eq. 5.24 is

$$p = P_a \quad \text{on the plates boundary} \tag{5.25}$$

Equation 5.24 is a nonlinear partial differential equation which can be solved only for special cases by numerical methods. However, by virtue of the fifth assumption, the variations in p will be small compared with the ambient pressure level P_a :

$$p = P_a + \delta p \tag{5.26}$$

where $\delta p \ll P_a$.
When eq. 5.26 is substituted into eq. 5.24 and second-order terms are neglected, a linear equation results. This equation, written in nondimensional form, yields :

$$\Delta\psi - \sigma\,\frac{\delta\psi}{\delta\tau} = \sigma\,\frac{\delta\xi}{\delta\tau} \tag{5.27}$$

where $\psi = \delta p/P_a$ nondimensional pressure perturbation, σ = squeeze number defined in eq. 5.36, $\xi = e/h_o$ nondimensional plate displacement and $\tau = \omega t$ nondimensional time.
We compute the film response to a simple harmonic motion excitation. Assume, therefore, that the variation of the plate spacing is given by

$$e = e_o \cos\tau \tag{5.28}$$

where e_o may vary over the plate surface, but is not a function of time. Equation 5.28 is in nondimensional form

$$\xi = \chi \cos\tau\,; \qquad \chi = \frac{e_o}{h_o} \tag{5.29}$$

Equation 5.27 then becomes

$$\Delta\psi - \sigma\,\frac{\partial\psi}{\partial\tau} = -\,\sigma\,\chi\,\sin\tau \tag{5.30}$$

Assume the solution has the form

$$\psi = \psi_1 \cos \tau + \psi_o \sin \tau \tag{5.31}$$

i.e., the pressure distribution has a component $\psi_1 \cos\tau$ which is in phase with the film thickness disturbance $e_o\cos\tau$, and a second component which is "out of phase" with the film thickness disturbance, but in phase with the squeeze velocity $e_o\sin\tau$. Another interpretation of eq. 5.31 is that the fluid film acts as a spring ψ_1 and as a viscous damper ψ_o. Insert eq. 5.31 into eq. 5.30 and equate coefficients of $\cos\tau$ and $\sin\tau$ separately :

$$\Delta\psi_1 - \sigma\psi_o = 0 \tag{5.32}$$

$$\Delta\psi_o + \sigma\psi_1 = -\sigma \tag{5.33}$$

with trivial boundary conditions on both ψ_o and ψ_1.

The cutoff frequency is that frequency where the spring and damping force amplitudes are equal in magnitude, or, in terms of our notation

$$f_o = f_1 \tag{5.34}$$

where f_o and f_1 are the nondimensional damping and spring pressure force amplitudes. The forces themselves are obtained by multiplying f_o and f_1 by P_aA.

$$f_i = (-1)^{-i} \frac{1}{A}\int_A \psi_i \, dA \quad ; \qquad i = 0 , 1 \tag{5.35}$$

Let us consider the solutions for a rectangular plate in parallel motion. The squeeze number of a rectangular plate of dimensions l x w is defined as

$$\sigma = \frac{12\, \eta\, l^2}{P_a\, h_o^2}\, \omega \tag{5.36}$$

The solutions of eqs. 5.32 and 5.33 are [140]

$$\psi_o = \chi \sum_{\substack{m,n \\ \text{odd}}} a_{mn} \cos m\pi x \cos \frac{n\pi y}{\alpha} \tag{5.37}$$

$$\psi_1 = \chi \sum_{\substack{m,n \\ \text{odd}}} b_{mn} \cos m\pi x \cos \frac{n\pi y}{\alpha} \tag{5.38}$$

where

$$\alpha = \frac{w}{l} = \text{plate aspect ratio}$$

$$a_{mn} = \frac{16\sigma\,(-1)^{\frac{m+n}{2}}\left[(m\pi)^2 + \left(\frac{n\pi}{\alpha}\right)^2\right]}{\pi^2 mn\left\{\left[(m\pi)^2 + \left(\frac{n\pi}{\alpha}\right)^2\right]^2 + \sigma^2\right\}}$$

$$b_{mn} = \frac{16\sigma^2\,(-1)^{\frac{m+n}{2}}}{\pi^2 mn\left\{\left[(m\pi)^2 + \left(\frac{n\pi}{\alpha}\right)^2\right]^2 + \sigma^2\right\}}$$

The nondimensional damping and spring force amplitudes for a rectangular plate are obtained by eq. 5.35

$$f_o = \frac{64\,\sigma\,\chi}{\pi^6}\sum_{\substack{m,n\\ \text{odd}}}\frac{m^2 + (n/\alpha)^2}{(mn)^2\left\{\left[m^2 + (n/\alpha)^2\right]^2 + \sigma^2/\pi^4\right\}} \tag{5.39}$$

$$f_1 = \frac{64\,\sigma^2\,\chi}{\pi^8}\sum_{\substack{m,n\\ \text{odd}}}\frac{1}{(mn)^2\left\{\left[m^2 + (n/\alpha)^2\right]^2 + \sigma^2/\pi^4\right\}} \tag{5.40}$$

Equating the force amplitudes gives an algebraic equation for the cutoff frequency. If only one term is maintained in the summations of this equation, the cutoff squeeze number yields

$$\sigma_c = \pi^2\left(1 + \frac{1}{\alpha^2}\right) \tag{5.41}$$

Solving for ω_c, cutoff frequency is obtained

$$\omega_c = \frac{\pi^2\,P_a\,h_o^2}{12\,\eta}\left(\frac{1}{l^2} + \frac{1}{w^2}\right) \tag{5.42}$$

For the case of an infinitely wide plate ($w \gg l$), we get the same result as obtained by the approximation in Ref. [148]. However for the case of our accelerometer we have to consider a quadratic plate.

The nondimensional spring and damping forces are plotted in Fig. 5.10 versus the squeeze number σ with the plate aspect ratio α as a parameter. The damping force reaches its maximum value approximately (but not exactly) at the cutoff frequency. Excitation above or below this frequency results in a

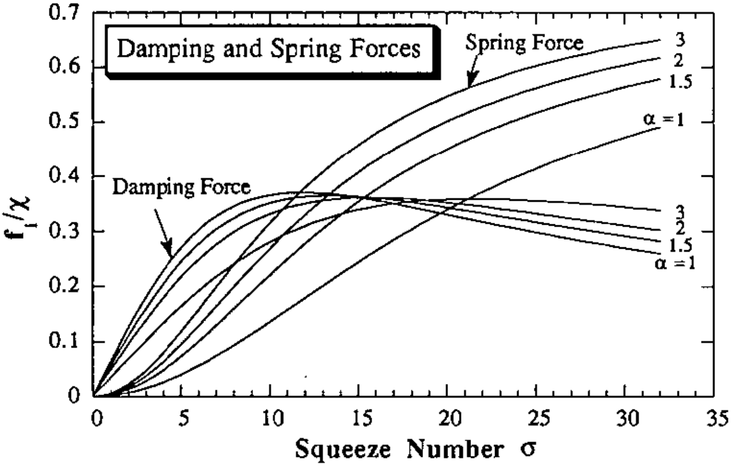

Fig. 5.10 Nondimensional forces on a rectangular plate in function of the squeeze number and plate aspect ratio

decreased damping force.

When the relative velocity between the plates is low, the film is effectively incompressible and has ample time to escape from in-between the plates. At high velocities, the film approaches a purely compressible state with no fluid flow, and the situation may be compared to a piston and cylinder. Consequently, at low velocities, viscous damping forces are predominant whereas at high velocities spring forces take over.

If the frequency ω is much below the cutoff frequency $\omega \ll \omega_c$, only first order terms of σ have to be considered as the squeeze number is then $\sigma < 1$. Thus with eqs. 5.39 and 5.40 and in the first term approximation we find

$$f_o = \frac{64\,\sigma\chi}{\pi^6}\,\frac{1}{1+\left(\frac{1}{\alpha}\right)^2} \tag{5.43}$$

$$f_1 \approx 0 \tag{5.44}$$

Thus the squeeze plates at frequencies much below the cutoff-frequency act as a viscous damper having the following damping constant c_{sq}

$$c_{sq} = \frac{768\,\eta\,l^3\,w}{h_o^3\,\pi^6}\,\frac{1}{1+\left(\frac{1}{\alpha}\right)^2} \tag{5.45}$$

which is pressure independent [148].

So the cutoff frequency for our accelerometer design of the second generation (see section 3.4) encapsulated in a cavity at air pressure can be calculated as follows. Although the device is damped by a squeeze film on both sides of the mass, formula 5.42 remains unchanged. Because both forces f_0 and f_1 are twice the value of one damping layer, equating them results in the same eq. 5.42 for the cutoff frequency.

We find for the cutoff frequency with the following dimensions $l = w = 2131$ µm, $P_a = 1$ bar $= 10^5$ Pa, $h_o \approx 10 - 30$ µm, $\eta_{\text{air at 1 bar at 25 °C}} = 18.2\ 10^{-6}$ Pa s

$$\omega_c\ (h_o{=}10\ \mu m) \approx 200\ \text{kHz}.$$

Hence the cutoff frequency is much higher than the first resonance frequency of our piezoresistive accelerometer design. Consequently, the squeeze film acts like a viscous damper for any cavity > 7 µm (= continuum limit for the gas) with the damping constant c_{sq}.

5.6 CONCLUSIONS

The accelerometer sensor chip, a resonant structure, has to be damped in order to avoid breakage and to have an increased usable frequency range. To achieve damping most accelerometer devices are enclosed in a cavity by bonding pre-etched wafers on both sides of the sensor chip. Either liquids or gases can be used for damping. For both damping mediums the squeeze film theory as developed by J. Blech [139] was applied. Not only the damping film thickness and thus the size of the cavity but also the viscosity and the dimensions of the moving mass determine the damping characteristics. It has been shown that in gases and liquids for film thicknesses greater than 7 µm and for frequencies much less than 200 kHz, the damping force is proportional to the velocity of the moving mass. Furthermore the viscous damping factor is proportional to the viscosity of the damping fluid, and also dependent on the damping film thickness and on the dimensions of the seismic mass. Thus, assuming the dimensions of mass and cavity to be temperature independent, the only temperature dependence results from that of the viscosity. It can be concluded that the damping of a liquid-damped accelerometer is much more temperature dependent than that of an air-damped device. In addition the viscous damping force of a liquid-damped sensor chip decreases for increasing temperature, e.g. the accelerometer is less damped at elevated temperatures. The opposite case is expected for an air-damped accelerometer. A sensor chip immersed in a liquid shows severe disadvantages over a device in gas, since both sensitivity and resonance frequency are greatly reduced.

In the next chapter methods for encapsulation of accelerometers are discussed. In chapter 7 results of oil- and air-damped devices are compared with theoretically expected data based on formulae developed in this chapter.

Chapter 6

Encapsulation of the Sensor Chip

The encapsulation of the sensor chip has to guarantee adequate damping and overrange protection. Typically the chip is enclosed from both sides by two pre-etched caps with integrated mechanical stoppers. If this procedure is performed on the wafer level, a reliable wafer to wafer bonding process is required which is compatible to the fabrication sequence of the sensor chip wafer. In section 6.2 different bonding techniques are briefly summarized and discussed with regard to an application for accelerometers. Based on a chip-by-chip mounting technique into a metallic housing two mounting configurations for both liquid and gas damping are described in section 6.3.
Parts of this chapter have been published in [130, 131].

6.1 INTRODUCTION

The encapsulation of the sensor chip has to guarantee not only adequate damping but also overrange protection. Typically the damping is achieved by enclosing the sensitive device entirely in a small cavity by bonding wafers to both sides of the sensor chip. The overrange protection can be realized by integrating mechanical stoppers into the cavity. Thus at high accelerations the deflection of the mass is limited and the beams do not break. Such an encapsulated sensor has been published by ICSensors and is schematically drawn in Fig. 5.2. This chapter mainly deals with the technological background whereas the different published approaches of the encapsulation of accelerometers are summarized in section 5.2.
Two main encapsulation techniques can be distinguished, the encapsulation on the wafer level defined here as microencapsulation and the chip-by-chip encapsulation defined here as macroencapsulation. Microencapsulation is advantageous because hundreds of sensors can be packaged at the same time. However, this technique needs a reliable wafer to wafer bonding process with

good alignment possibilities as well as a technique for the subsequent attachment of the encapsulated chip to a mechanical support. Different wafer to wafer bonding methods are discussed in the next section with a view to their application for gas-damped piezoresistive accelerometers.

We have chosen the chip-by-chip mounting technique since this method is based on already existing experience from the encapsulation of piezoresistive pressure sensors and their hermetic sealing [149]. This technique easily allows the damping medium to be changed, e.g. to fill the housing with a liquid in the place of gas. The advantages and disadvantages of the macroencapsulation are described in section 6.3.

6.2 MICROENCAPSULATION

This section briefly overviews the main bonding techniques and discusses their compatibility with the encapsulation of piezoresistive accelerometers. The microencapsulation of accelerometers requires a reliable wafer to wafer bonding process to both sides of the processed sensor chip wafer. Adhesion can be obtained by means of gluing, eutectic bonding, soldering, glass bonding, silicon fusion bonding or anodic bonding.

Because the packaging of air-damped accelerometers requires high precision (the size of the cavity must be within ± 1 μm for air-damped devices), low process temperature (< 450°C, Al metallization) and bipolar compatibility (Al as metallization), silicon fusion bonding, eutectic bonding, epoxy, polymer bonding or soldering can not be considered for the packaging of silicon, piezoresistive accelerometers fabricated by a bipolar compatible process. Since some of these techniques have been applied by several research groups [6, 36] for the successful encapsulation of their accelerometers, they are briefly described below.

- **Silicon Direct Bonding (SDB) or Silicon Fusion Bonding (SFB)**
  This method makes possible to bond bare Si Wafers and/or oxidized silicon wafers. It is well described in the literature [150-155]. The wafers must be mirror-grade polished and the surfaces must be made hydrophilic prior to the bonding. The direct bonding is based on a chemical reaction between OH-groups, which are present at the surface. This reaction occurs already at 200°C. At higher temperatures the number of OH-groups involved in the reaction increases, which results in an increasing bond strength. At temperatures of more than 1000°C the bond strength may approach the strength of the bulk. The bonding is hermetic, has a high yield strength and does not require any intermediate bonding layers. An additional applied voltage during bonding (30 - 50 V) seems to improve the yield and quality

[156, 157]. But the process is rather sensitive to impurities. This method is often used for silicon-on-insulator (SOI) applications [158, 159]. Furthermore, it has been demonstrated, that p-n junctions with low leakage and sharp breakdown voltages can be formed by bonding a wafer with a p-type diffusion to a n-type wafer [160].

- **Eutectic Bonding:** The compatibility to the already existing industrial bipolar production line forced us to resign from using a Si/Au eutecticum. Its eutectic temperature is only 363°C, which is well below the eutectic temperature of Si/Al [161]. The major problem of this technique is to obtain complete bonding of large areas. Even native oxides prevent the silicon gold bonding to take place. In addition some mechanical motion could be required during bonding to enhance the alloying process. As most materials for eutectic bonding are quite ductile, it may result in a long term mechanical drift. In spite of all this problems, ICSensors applies successfully this bonding process for the encapsulation of their piezoresistive accelerometers [37].
  An interesting combination is also the reaction of titanium with silicon [162-165]. We achieved a hermetic seal between silicon wafers using a titanium intermediate layer [166]. The bonding was performed at 700°C in an oxygen ambient. As the whole metallization was oxidized and thus became an insulator, titanium can not be used for both metallization and bonding layer at the same time.

- **Epoxy, Polymer Bonding** [167] or **Soldering** seem never achieve the precision needed for the size of the cavity (± 1 μm).

The following low-temperature bonding techniques might be suitable for the encapsulation of accelerometer chips :

- fusion bonding of silicon wafers with low melting temperature glass
- anodic bonding
- silicon to silicon bonding via a sputtered pyrex glass layer
- direct bonding using a spin-coated thin layer of sodium silicate, aluminum phosphate or ammonia-silica solutions.

Their main characteristics are summarized in Table 6.1.

Silicon fusion bonding with low melting temperature glass

This technique allows bonding at temperatures ~450°C using a layer of boron glass between the wafers [168, 169]. The silicon wafers are heated until the glass layer melts and forms a bond with the silicon surfaces. The bonding

Table 6.I Main characteristics of low-temperature bonding processes [170, 171]

	silicon bonding with low melting glass	anodic bonding	bonding via a thin sputtered layer of pyrex glass	bonding via a intermediate thin layer of sodium silicate
adhesion material	Boron glass	Pyrex #7740	sputtered Pyrex #7740	OH-groups
required thickness	1 μm	substrate	1 - 5 μm	36 nm
thermal expansion coefficient	$0.5\ 10^{-6}\ K^{-1}$	$2.9\ 10^{-6}\ K^{-1}$	$2.9\ 10^{-6}\ K^{-1}$	-
bonding temperature	450°C	180°-500°C	350°-500°C	200 °C
applied voltage	-	200 - 500 V	50 V	-

shows a high mechanical strength at the seal and furthermore it is compatible with planar processing. At least one layer of boron glass deposited at 1075°C is required to make a bond between two wafers. An important constrain of the low-temperature boron-glass bonding process is that the processing must be completely phosphorus free. If phosphorus is in the system, the temperature must exceed 900°C in order for a liquid phase to exist for the $B_2O_3/P_2O_5/SiO_2$ system [172].

Experiments performed at ASCOM using the process parameters given by Field and Muller [168, 173] have lead to very promising results. One major problem remains the bonding difficulties after a plasma process and hard baking of photoresist. The high sensitivity of the process to the history of wafers did not allow the sensor chip wafers to be bonded to the encapsulation wafers. It seems, that a lot of process parameters need to be adapted for this bonding process.

Anodic Bonding

Anodic bonding is an electrostatic bonding process which can be accomplished on a hot plate at temperatures between 180°C and 500°C (well below the softening point of pyrex glass). It can be performed in most atmospheres or in vacuum. Mostly Pyrex glass #7740 is used since its thermal expansion matches well that of silicon. The anodic bonding process is widely used for bonding of absolute piezoresistive pressure sensors. This process shows good reliability and even allows bonding to a silicon surface with thermally grown oxide up to 4600 Å thick. The bonding set-up is shown schematically in Fig. 6.1. The polished Pyrex glass is placed against the polished surface of the silicon. A

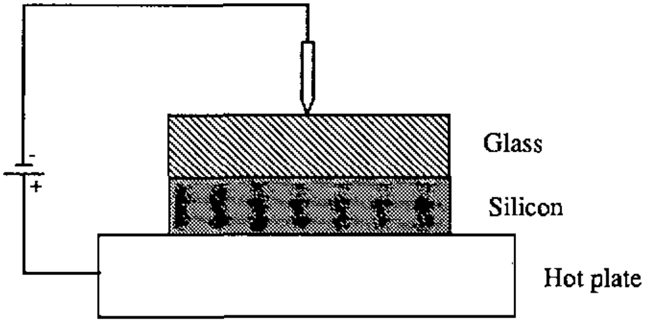

Fig. 6.1 Schematic setup for anodic bonding [174]

cathode electrode is held against the outer surface of the glass wafer and the whole assembly is heated on a hot plate, which also serves as an anode. A 200 - 1000 V potential is then applied between the two wafers. The electric potential between the two wafers causes them to be pulled into close contact and they bond almost instantly.

The electrostatic attraction between the glass and silicon wafers is developed as follows. At elevated temperatures (yet below the softening point of Pyrex), the positive sodium ions in the glass become quite mobile and they are attracted to the negative electrode on the glass surface. The more permanently bound negative ions in the glass are left, forming a space charge layer in the glass adjacent to the silicon surface. After the Na^+ ions have drifted toward the cathode, most of the potential drop in the glass occurs at the surface next to the silicon. The two wafers then act as a parallel plate capacitor with most of the potential being dropped across the several micron wide air gap between them. The resulting E-field between the surfaces serves to pull them into contact. Once in contact, almost all of the applied potential is dropped across the space charge layer in the glass. The extremely high fields which develop in that region transport oxygen out of the glass to bond with the silicon surface. The seal appears to be chemical in nature, possibly a very thin layer of grown SiO_2 makes the process irreversible [174].

The wafers which enclose the sensitive accelerometer chip have to be pre-etched in order to form thin damping layers on both sides of the moving mass. Thus an etch process for Pyrex glass #7740 was developed [175]. The following parameters have given the best, reproducible results :

- metallization Cr (500 Å) + Au (5000 Å)
- photolithography and metal etching
- spinning of thick photoresist 5 µm (as a metal protection) + lithography
- etching BHF (15/1) at 60°C (etch rate ≈ 8 µm/h)

The lateral etch rate was about 6 times higher than the vertical one. This effect can be compensated by an adapted mask design. Furthermore the lateral dimensions of the cavity is not of great importance for the encapsulation of sensor chips. Since pyrex glass is transparent, it is easy to align the sensor chip to the glass. We bonded successfully single sensor chips to preetched Pyrex glass cavities with no integrated mechanical stoppers. The electrostatic attraction of the seismic mass was sometimes so strong that the mass was bonded to the bottom of the cavity, which broke the beams. This problem can be solved by coating the surface of the mass with Aluminum to avoid bonding and by integrating overrange stoppers into the cavity.

Silicon to silicon anodic bonding via a sputtered pyrex glass layer

In the last years several research groups worked on the bonding via a sputtered pyrex glass #7740 layer [176 - 178] or via a sputtered low softening Iwaki #7570 glass layer [179]. This bonding technique has found a great field of application [180, 181]. The surfaces of the silicon to be bonded should be polished. One of the silicon wafers needs to be coated with a thin, sputtered Pyrex film of thickness 1 to 5 µm. To perform the electrostatic bonding the Si wafer with coated Pyrex is placed on another bare silicon surface to which it will be bonded. The negative electrode of the DC power supply is applied to the coated Si member. A maximum voltage of 50 V is adequate for the bonding. The whole assembly must be heated up to 350° to 500°C. The voltage should be applied for a time period long enough to allow the current to settle at steady state leakage current to complete the bonding process, typically 10 minutes for a 3 inch wafer. In order to have a successful bonding, the two members to be bonded should be in intimate contact over the whole bonding area. Since the applied voltage is low, the electrostatic force which will pull the two wafers together is also small. Thus any small contamination will cause a bonding failure.

A major problem of this process is the crack-free sputtering of the several µm thick Pyrex glass layer. The sputter rate is very low (0.1 - 0.3 µm/h) which results in a long deposition time. Thus an industrial application is not yet feasible. On the other hand the silicon-to-silicon anodic bonding method has proved to result in lower temperature coefficient for the offset in pressure sensors compared to pyrex bonded or solder glass bonded devices [182]. Therefore this technique could be very promising for the encapsulation of piezoresistive accelerometers.

Direct silicon bonding using a spin-coated sodium silicate layer

In 1991 Quenzer and his coworkers from the Fraunhofer-Institute in Berlin published a low temperature silicon wafer bonding technique using an intermediate spin-coated sodium silicate layer [183]. After a treatment to make the surfaces hydrophilic, a diluted solution of sodium silicate in water was

spun on one of the wafer surfaces. In a next step, the wafers were brought together and were heated up to 200°C for two hours to reach the seals highest mechanical strength. The silicate layer (2%) had a thickness of only 300 Å. The strongest bonds (30 N/mm^2) were found by Quenzer et al. for bonding two silicon dioxide surfaces (thickness 3000 Å each) together. A further increase of the temperature did not result in a higher surface energy. The bonding mechanism is assumed to be based on the following principle. After the wafers are brought into contact, the attraction force between the absorbed hydroxyl groups and water molecules on both surfaces brings the two surfaces into close contact with each other. During the final annealing step, the gel layer loses residual water. A further condensation reaction in the silicate gel layer results in strong bonds between the two surfaces. The surrounding silicon oxide layers absorb all the water if the total amount of water does not exceed a critical value. Quenzer et al. expanded his work on aluminium phosphate and ammonia-silicate solutions [171]. The aluminum-phosphate needs an annealing temperature of 400°C to reach its strongest bond. To achieve full IC compatibility Quenzer tested also layers of ammonia-silica solutions. He measured a surface energy of 1.5 J/m^2 after an anneal at 300°C.
The low temperature process described above seems to be a very promising technique for the encapsulation of sensor chips. However, long term stability and temperature behaviour still remain to be investigated.

The preliminary work has shown that the fabrication process of the sensor chip wafer has to be adapted with regard to the chosen bonding technique. Although some unprocessed wafers have been successfully bonded by either SFB with low melting glass, anodic bonding or a spin-coated sodium silicate layer, a successful and reliable microencapsulation using one of the bonding methods described above still needs much further investigation.

6.3 MACROENCAPSULATION

In view of the above our main effort was performed on the chip-by-chip encapsulation into a metallic housing, so-called macroencapsulation. This technique is based on a similar industrial process used for the encapsulation of piezoresistive pressure sensors. The whole mounting technique was developed in close collaboration with KELLER AG, Winterthur, where all the devices were packaged. As most of their pressure sensors are mounted into an oil-filled stainless steel package, it was obvious to start with liquid damping of accelerometer chips.

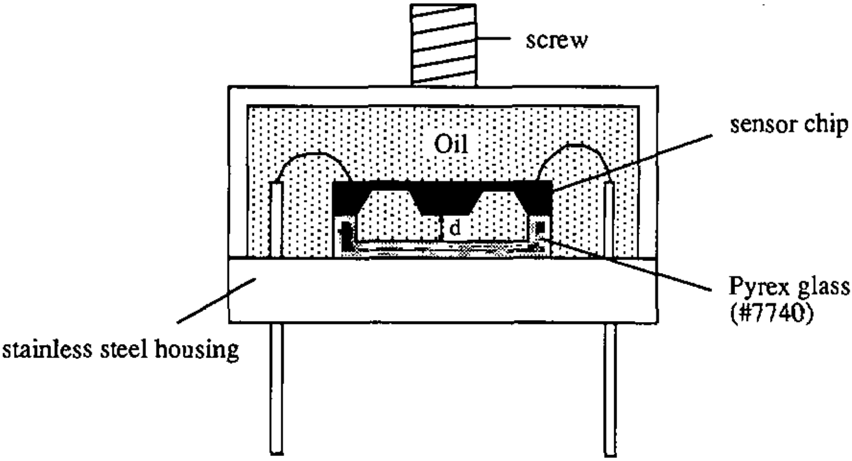

Fig. 6.2 Cross section of an oil-damped accelerometer

The chosen chip-by-chip mounting requires the wafer to be diced prior to mounting. Since the sensitive devices are not yet neither overrange protected nor damped, the yield of this step was rather poor. A cross sectional view of a packaged, oil-damped accelerometer is shown in Fig. 6.2. The u-like cavity was either mechanically machined or chemically etched out of Pyrex glass (# 7740). The chip was glued on only one side of the frame to the glass which in turn was glued to the base. After wire bonding the stainless steel housing was filled up with silicon oil (AK 100) and hermetically sealed. The screw at the top allowed the device to be directly mounted onto the object which had to be measured.

This simple mounting technique easily allows devices with different damping film thickness' to be investigated (results see section 7.2). But the missing overrange protection and the difficulties to machine the glass with sufficient accuracy were important disadvantages. Thus the encapsulation technique was changed and resulted in a Si-Si-Si sandwich mounted in a metallic housing as schematically drawn in Fig. 6.3. It can be seen that the Pyrex glass chip was replaced by two pre-etched silicon caps on either side of the sensitive device. This was used since silicon can be easily etched and with high precision. Furthermore overforce stops were integrated into both silicon caps. The unique feature of this encapsulation is that the whole Si-Si-Si structure is only clamped by a piece of rubber and the metallic housing. No glue or any bonding techniques were used. A ceramic ring facilitated to build up the Si-Si-Si structure. Since this mounting might have an industrial application, no further details can be given. A photograph of an overrange protected and air-

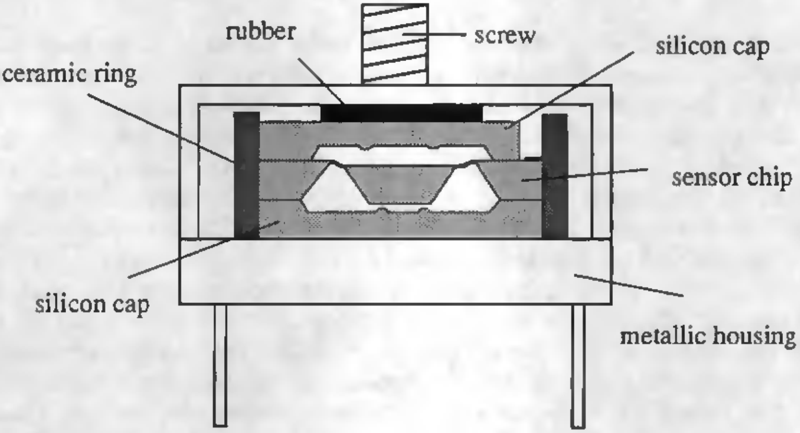

Fig. 6.3 Schematic drawing of an encapsulated, overrange protected and air-damped accelerometer (developed in collaboration with KELLER AG)

damped accelerometer is shown in Fig. 6.4. The whole package is 5 mm high (without the screw) and has an external diameter of 12 mm. Results with this device will be given in section 7.3.

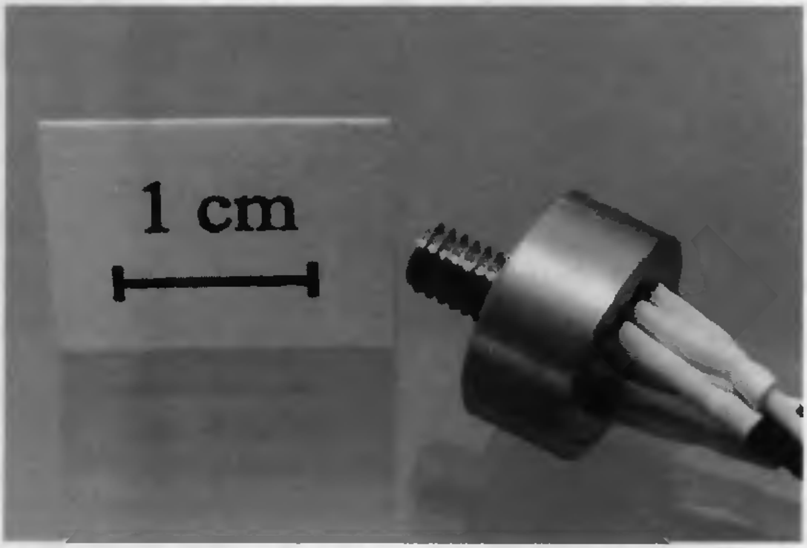

Fig. 6.4 Housing of an air-damped silicon piezoresistive accelerometer (packaged by KELLER AG)

6.4 CONCLUSIONS

Basically two methods of encapsulation can be distinguished, at the wafer level (microencapsulation) and chip-by-chip encapsulation (macroencapsulation). The wafer level technique is advantageous since hundreds of sensor chips are packaged in one process step, which keeps production costs low. In addition the overrange protected structures do not suffer while sawing the bonded wafers. However, it is difficult to find a reliable low temperature wafer to wafer bonding process by which the sensor wafer, after a 10 mask fabrication sequence, can be hermetically enclosed on both sides. Preliminary work on several low temperature bonding techniques have shown the need for individually adapting the fabrication process of the sensor wafer to the corresponding bonding process. Thus for example if the bipolar compatibility of the process is given up, eutectic bonding or high temperature processes could be considered. However, only a thorough investigation on the different bonding techniques including the adaptation of the fabrication process will lead to a reliable microencapsulation.

We have chosen the chip-by-chip encapsulation in a metallic housing since it is simple and easily adaptable. The high flexibility of this encapsulation technique required only a low number of sensor chips in order to determine the optimal size of the cavity. Its unique feature is that the Si-Si-Si structure is only clamped. This makes the mounting straightforward and thus competitive to the microencapsulation. Furthermore it is suitable for both gas and liquid damping. Additional advantages are a hermetic seal, electromagnetic shielding by the metallic housing and for air-damped devices the well controllable gas pressure within the metallic housing. This chip-by-chip mounting would also allow accelerometers with a surrounding mass to be encapsulated [39, 184]. This can not be realized on the wafer level.

A major drawback of this technique is the sawing of the sensitive device wafer prior to mounting. Although there were accelerometer chips with a range of 50 *g*, many devices broke during sawing. Thus this step might become crucial for very sensitive sensor chips and needs further investigation.

This simple mounting technique allow us to investigate the effect of the damping medium, the damping film thickness and the temperature on the performance of accelerometers. This is described in the next chapter.

Chapter 7

Characterization of Encapsulated Devices

The characterization of the encapsulated sensor chip allows the final performance of the device to be determined. In addition to the measurements on the not encapsulated sensor chip the damping, an important factor which defines the usable frequency range, and the overrange protection can be tested. Since the damping behaviour depends mainly on the damping film thickness and the viscosity of the damping fluid, different configurations of oil- and air-damped devices are tested. Furthermore, the device characteristics, e.g. offset, sensitivity and damping were strongly temperature dependent. These effects and their consequences are discussed in this chapter.
Parts of this chapter have previously been published in [130, 131].

7.1 INTRODUCTION

Due to production problems and imperfections every single encapsulated and mounted device has to be thoroughly tested. Furthermore with increasing implementation of sensors into computerized control systems most of the electrical imperfections and non-linearities can be dealt with means of a microprocessor to give a temperature independent and linear output (see for instance the signal processor "SENSO-BRAIN" by KELLER AG). Thus a simple characterization cycle will be needed to allow electronic adjustments.
The major parameters that characterize a piezoresistive accelerometer are given in Table 7.I. Static and dynamic (sinusoidal) measurements at different temperatures as well as shock tests are used to determine these parameters. The offset and sensitivity of a device are controlled by turning the device in the gravitational field. On a vibrating table, the linearity of the sensitivity up to full scale (FS) and the frequency response are checked. Both, static and dynamic measurements are performed over the whole temperature range in order to examine the temperature dependence of both, sensitivity and offset.

Table 7.I Main performance specifications of an accelerometer

- Acceleration range	[*g*]
- Frequency response (range of frequencies over which device sensitivity is within ± 5% of the DC value)	[Hz]
- Resonance frequency	[Hz]
- Sensitivity	[mV/V *g*]
- Offset at zero acceleration	[mV/V]
- Transverse sensitivity [% of Sensitivity]	[%]
- Temperature coefficient of offset (TCO)	[%/ °C]
- Temperature coefficient of sensitivity (TCS)	[%/ °C]
- Acceleration limits (any direction)	[x FS]
- Supply voltage	[V]
- Operating temperature	[°C]

Also shock tests are performed to test the overforce protection and the perfect mechanical condition of the device.

7.2 OIL-DAMPED ACCELEROMETERS

All the results presented below were obtained on sensor chips of the second prototype mounted as described in section 6.3 and shown in Fig. 6.2. The damping medium was silicon oil (WACKER AK 100) having a viscosity at room temperature of 100 mm^2/s (or 0.096 Pa s). In this section the influences of oil-damping, damping film thickness and temperature on the device performance are investigated and compared to the theoretically expected values based on formulae developed in section 5.4. The frequency responses were experimentally obtained using the setup described in subsection 4.2.2.

7.2.1 Results and Discussion

Figure 7.1 shows the frequency responses of the same accelerometer, when the housing is filled with air at atmospheric pressure and when it is filled with silicon oil AK 100. The distance between the bottom of the mass and the top of the underlying pyrex glass chip was 300 μm. It can immediately be seen, that the air film did not damp the device at all, whereas the silicon oil film of the same thickness achieved nearly critical damping. In addition the oil-damped device displayed a 61% loss of sensitivity, and the resonance frequency dropped from 3340 Hz measured in air down to 1620 Hz. As explained in subsection 5.4.1, the loss of sensitivity is due to the buoyant force acting on the mass immersed in a fluid. The calculated reduction for a device in silicon oil is

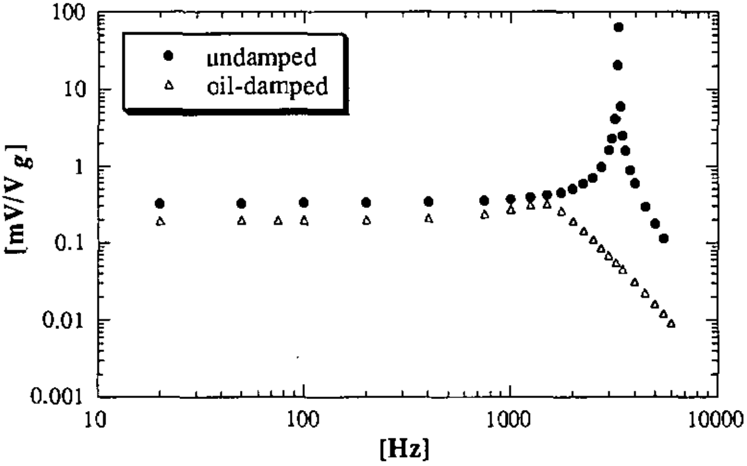

Fig. 7.1 Measured frequency response of an undamped and an oil-damped accelerometer recorded at room temperature

$(\rho_{Si} - \rho_{oil})/\rho_{Si} = 0.59$ ($\rho_{AK\ 100\ at\ 25°C} = 0.96\ g/cm^3$), which agrees well with the measured value of 0.61.

A combination of three effects caused the shift of the resonance frequency : the reduced effective mass, an added virtual mass and viscous damping (for a detailed explanation see section 5.4.2). Bearing in mind that the resonance frequency is inversely proportional to the square root of the mass, the influence of each effect is individually calculated with regard to the undamped device. The buoyancy reduces the effective mass, as calculated above by 59%, which in turn increases the resonance frequency by a factor of 1.3. Using eq. 5.22 the added mass by the fluid surrounding the vibrating seismic mass is calculated to be four times the effective mass. This reduces the resonance frequency by a factor of 0.45. Since viscous damping shifts the resonance frequency as given by eq. 5.23, we calculate a shift of 0.9 for the measured magnification factor β of 1.64. Taking into account all three effects we obtain a theoretical shift of the resonance frequency of 53%, which corresponds within 10% to the measured data.

The theory on incompressible squeeze film has shown that damping of the device is determined by the thickness of the damping film, by the viscosity of the fluid and by the dimensions of the moving mass (eqs. 5.14 - 5.16 in subsection 5.4.2). In order to investigate these dependences bridge-type accelerometers with different spacings d between the seismic mass of the sensing element and the underlying glass cap (distance d in Fig. 6.2) were measured. Figure 7.2 clearly shows that for increasing damping film thickness the device becomes less damped.

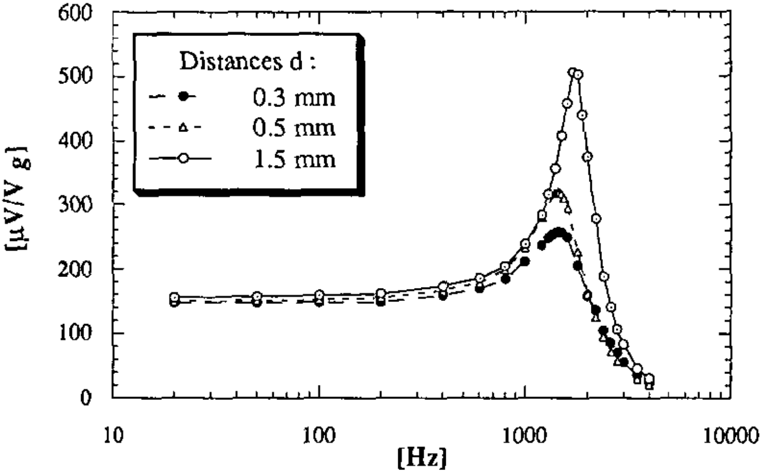

Fig. 7.2 Measured frequency response of accelerometers with different spacings d between the seismic mass and the underlying cap recorded at room temperature (note: linear vertical scale)

Based on the formulae developed in sections 5.4 and 5.5 the approximate oil film thickness needed for critical damping at room temperature is calculated. We see from Fig. 7.2 that the device has a resonance frequency of about 1650 Hz. Since in our mounting the damping fluid is only squeezed on the back of the sensor chip, the effective surface of the moving quadratic mass ($m = 2.4\ 10^{-3}$ g) is the square of 1863 μm. For a quadratic plate the force reduction factor κ_s in eq. 5.16 becomes 0.422. Thus the viscous damping factor c_{lsq} in eq. 5.14 has to fulfil eq. 5.4, e.g.

$$\gamma = \frac{c_{lsq}}{2\sqrt{mk}} = \frac{\sqrt{2}}{2} \tag{7.1}$$

where $k = m\ (2\pi f_{res})^2$.

Introducing eq. 5.14 into eq. 7.1 and solving it for h, we obtain for a silicon oil-damped (AK 100) accelerometer a film thickness h of

$$h = \sqrt[3]{\frac{0.422\ \eta\ l^3\ w}{m\ (2\pi f_{res})\ \sqrt{2}}} = 240\ \mu m \tag{7.2}$$

for critical damping at room temperature. Although the configuration, on which the squeeze film theory is based, does not exactly correspond to our

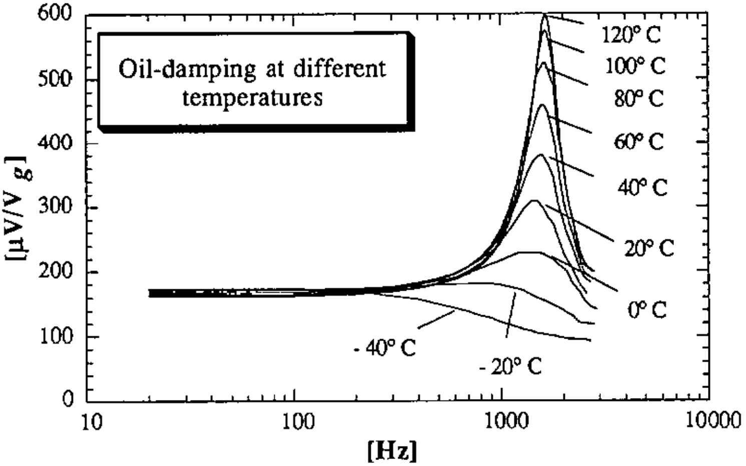

Fig. 7.3 Measured variation in frequency response with temperature (note : linear vertical scale)

setup, the calculated film thickness for critical damping is of the same magnitude as the measured one.

As can be seen in eq. 5.14 the only temperature dependent factor of the viscous damping factor is the viscosity of the damping fluid. Since the viscosity of liquids decreases with increasing temperature, the oil-damped device becomes less damped for increasing temperature as shown in Fig. 7.3. Whereas the device is critically damped at -20°C, it shows at 120°C a resonance peak about 4 times the DC sensitivity (12 dB).

7.2.2 Conclusions

The measurements have shown that the sensor chip immersed in oil exhibits a 60% loss of sensitivity and a 50 % reduction of the resonance frequency compared to the undamped device in air. Since oil has a much higher viscosity than air, an oil film 300 µm thick, damped the device nearly critically whereas an air film of the same thickness did not damp at all. Not only the thickness of the damping film, but also the viscosity of the damping fluid determine the damping factor. In agreement with the squeeze film theory the damping factor increases for decreasing film thickness and decreases for decreasing viscosity. The latter effect resulted in a 12 dB variation of the amplitude at the resonance frequency over a temperature range of 140°C, which makes oil-damped devices only useful for a restricted temperature range or for applications with a small frequency range.

7.3 AIR-DAMPED ACCELEROMETERS

All the results presented below were obtained on four-beam bridge-type accelerometers of the second prototype mounted as described in section 6.3 and shown in Fig. 6.3. The metallic housings were sealed in air under atmospheric pressure at room temperature. In this section the influences of the damping film thickness and temperature on the frequency response are measured and compared to the theoretically expected data based on formulae developed in section 5.5. In addition the functionality of the mounting and the mechanical overrange stoppers are investigated by crash tests.

7.3.1 Frequency Response

All the measured frequency responses were obtained using the experimental setup as described in subsection 4.2.2. As in the case of oil-damped accelerometers, the damping film thickness determined the damping behaviour. Figure 7.4 shows the frequency response of air-damped devices with different sizes of the cavity. The solid lines are measured data, and the dashed curves are calculated based on the squeeze film formulae developed in section 5.5. We note that the smaller the size of the cavity the better the damping. The device is critically damped at room temperature for a measured damping film thickness of 14 μm on both sides of the seismic mass. The

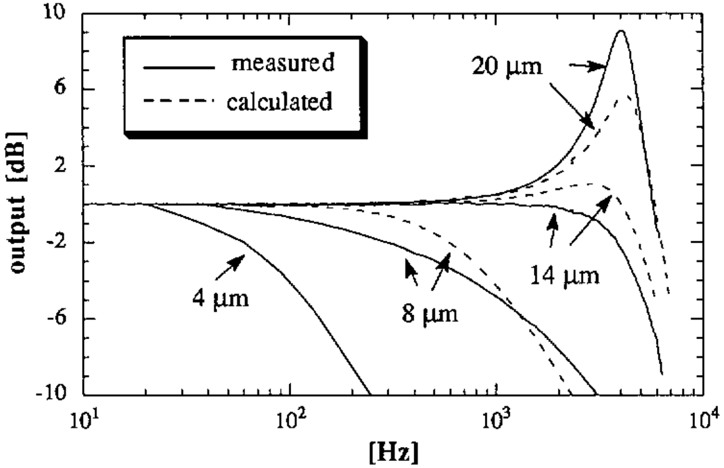

Fig. 7.4 Measured and calculated frequency responses of air-damped accelerometers for different sizes of the cavity

theoretical expected thickness can be calculated in the following manner.
As it was shown in section 5.3, for critical damping γ needs to be $\sqrt{2}/2$. Taking into account squeezed air films on both sides we find using eq. 5.4

$$\gamma = \frac{c}{2\sqrt{mk}} = \frac{c_{sq}}{\sqrt{mk}} = \frac{\sqrt{2}}{2} \qquad (7.3)$$

where $k = m\,(2\pi f_{res})^2$. The encapsulated four-beam bridge-type sensor chip had a resonance frequency of about 4200 Hz and a quadratic seismic mass of 4 mg with a mean side length of 2130 µm. At room temperature and at 1 bar the viscosity of air is 18.2 10^{-6} Pa s. Thus introducing eq. 5.45 in eq. 7.3 and solving for h_o we get

$$h_o = \sqrt[3]{\frac{768\,\eta\, l^3\, w}{\pi^6 \sqrt{2}\, m\,(2\pi f_{res})}} = 13\ \mu m \qquad (7.4)$$

This value is in good agreement to the experimental value of 14 µm.
In order to investigate the influence of the gas pressure on the damping, a hole was drilled through the screw into the metallic housing. A mechanical setup allowed the pressure in the housing to be changed over the range of 1 to 20 bar. At a gas pressure of 20 bar, the device was slightly more damped than at atmospheric pressure, i.e. the sensitivity at high frequencies (> 1 kHz) was 1-2 % smaller at 20 bar than at 1 bar. This indicates that the damping and thus

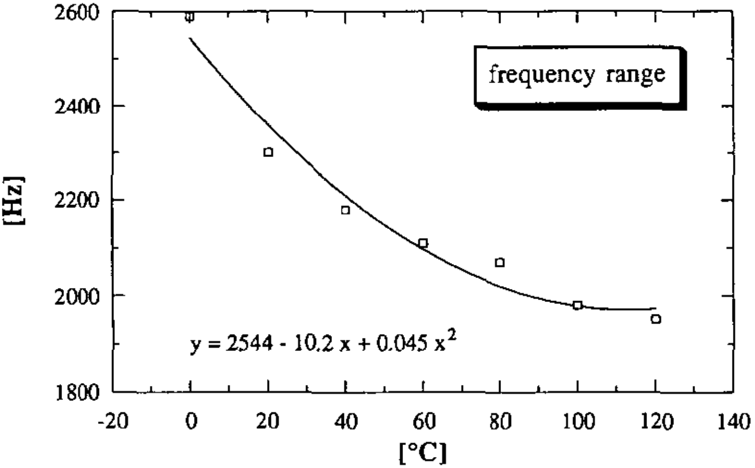

Fig. 7.5 Measured frequency range (± 5%) of an air-damped accelerometer at different temperatures

the viscosity is nearly pressure independent in the pressure range of 1 to 20 bar. This agrees with the theoretically expected pressure independence of damping as shown in eq. 5.45.

The temperature does not only affect the sensitivity and offset (see section 7.4) but also the viscosity of the air film. Figure 7.5 shows the frequency range for different temperatures. The useful bandwidth is defined as the range of frequencies over which the device's sensitivity is within ± 5% of the DC value. We see that for increasing temperature the frequency range decreases, which is due to the increasing viscosity of gases for increasing temperature (see section 5.3). The useful bandwidth dropped from 0-2600 Hz at 0°C down to 0-2000 Hz at 120°C.

7.3.2 Shock Test

Since an encapsulated accelerometer should withstand being dropped onto a concrete floor (corresponding to a shock of about 500 *g*), shock tests play an important role in the characterization of accelerometers. Both, the overforce

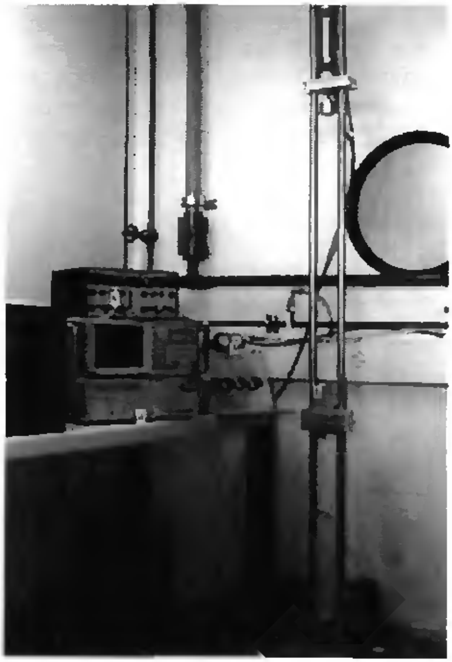

Fig. 7.6 Setup for shock tests (1 = aluminium block with integrated reference accelerometer and with the accelerometer to be tested screwed on it, 2 = pneumatic piston to imply a starting acceleration, 3 = pressure control of the piston, 4 = digitizing oscilloscope, 5 = voltage supply)

protection and the mechanical condition of the device can be tested.

The setup for crash tests can be seen in Fig. 7.6. An aluminium block, on which the device was mounted, was vertically guided by two metal rods and fell onto the base plate. In order to increase the maximum achievable acceleration, a pneumatic piston at a height of 2 m implied a starting acceleration. Depending on the material of the base plate, the frequency spectrum of the rebounds changed. A soft material led to a constant amplitude in the frequency space up to 500 Hz, whereas a hard material showed a constant amplitude in the frequency space up to 3 kHz. Accelerations of several thousands of *g* were possible. The reference accelerometer (Kistler Typ 8642 A5, 1.053 mV/*g*) was mounted at the center of the metal block. A digitizing oscilloscope stored the data and allowed a fourier transformation of the measured signal peak to be made online.

Shock tests performed on air-damped devices have proved the effectiveness of the integrated overrange stopper. A typical result of a shock test in the direction of the z-axis can be seen in Fig. 7.7. The response curve of the encapsulated air-damped accelerometer indicates, that the seismic mass touches the stoppers at an acceleration of about 300 *g* and can not be deflected more. This avoids breakage of the device although it was exposed to a peak acceleration of more than 1000 *g*. Since the overrange stoppers were at a distance of 3.5 µm from the surface of the mass at zero acceleration, the deflection per acceleration was about 12 nm/*g*. The theoretical calculated value using analytical formulae is 10 nm/*g*.

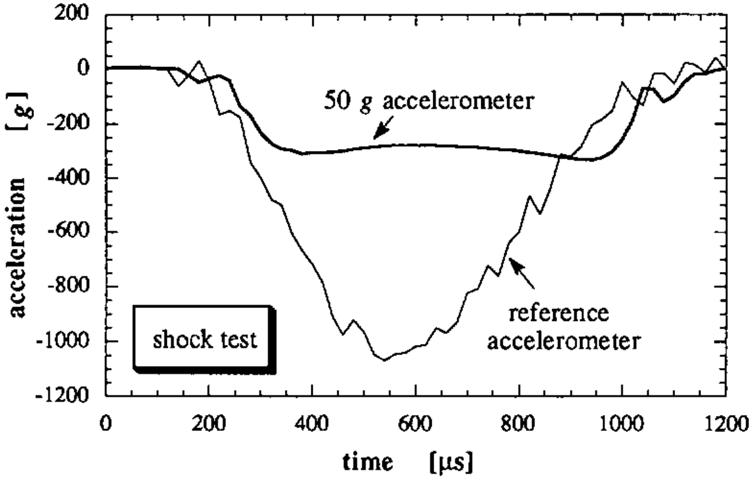

Fig. 7.7 Output of the accelerometer measured at a shock test

7.3.3 Conclusions

The measurements have shown that the damping of air films depend on the film thickness and on temperature. The damping factor increased for decreasing film thickness, which is in agreement with the squeeze film theory. Since the viscosity of gases increases for increasing temperature, the damping increases which results in a smaller usable frequency range at elevated temperatures. The calculated film thickness needed for critical damping was within 10% of the measured value. Thus the squeeze film theory is suitable to evaluate the size of the cavity. Since the typical film thickness was about 14 μm, the encapsulation requires high precision of the cavity in order to have a reproducible damping behaviour.
Crash test proved the effectiveness of the mechanical stopper and the mounting. As the mass touched the stopper only at about 300 *g*, the device could even be used for an acceleration range greater than 50 *g*. Although the whole Si-Si-Si structure was only clamped, it survived shocks of more than 1000 *g*.

7.4 TEMPERATURE RESPONSE OF OFFSET AND SENSITIVITY

In this section, the measured temperature dependence of air-damped piezoresistive accelerometers and basic concepts of compensation circuits for piezoresistive sensors [185 - 188] will be discussed.
First we define the temperature coefficient (TC) of a parameter X. Denoted TCX it is calculated by dividing the derivative of the parameter X with respect to temperature by the value of X at that temperature. Often the temperature coefficient is quoted at room temperature (25°C). The mathematical description is as follows

$$\mathrm{TCX} = \frac{\left(\frac{\partial X(T)}{\partial T}\right)_{T=25^\circ C}}{X(25^\circ C)}\ 100\% \tag{7.5}$$

Figures 7.8 and 7.9 show the measured temperature dependence of the offset O and sensitivity S of an encapsulated accelerometer. The sensors of the final series have typically a TCO of ± 0.3%/°C and a TCS of -0.2%/°C. With an offset of 4 mV/V and an acceleration sensitivity of 180 μV/V *g* the TCO is equivalent to 0.067 *g*/°C. It is apparent, that the temperature sensitivity of piezoresistive sensors is important. But there is the possibility to compensate

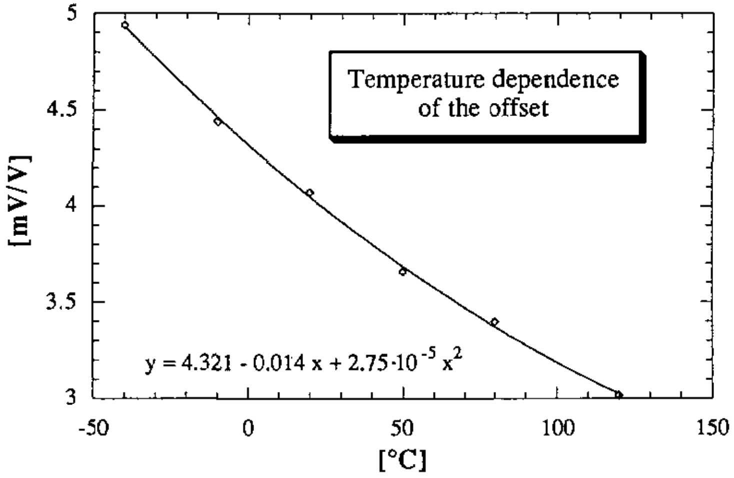

Fig. 7.8 Typical measured temperature dependence of the offset of a piezoresistive accelerometer with a constant voltage applied

partially for it by exact control of the TCS and TCR of the piezoresistors during fabrication and by adding a compensation circuit.

For a better understanding of the temperature coefficients, we consider first the temperature dependence of the sensitivity and resistivity of the piezoresistors. Figure 7.10, taken from Ref. [189], shows the TCR/55°C,

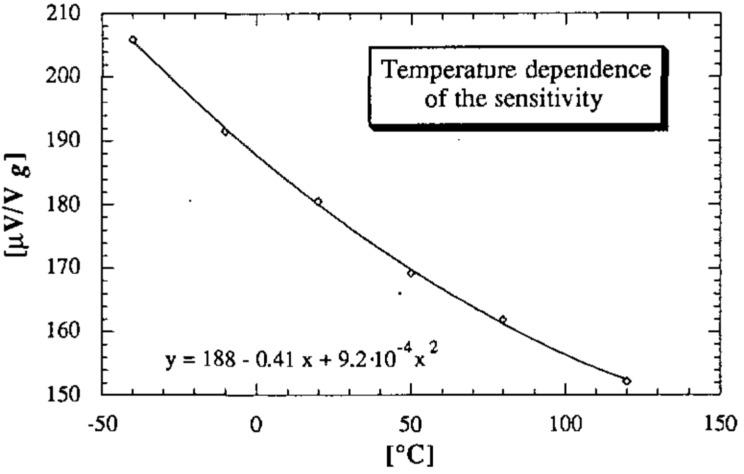

Fig. 7.9 Typical measured temperature dependence of the sensitivity of a piezoresistive accelerometer with a constant voltage applied

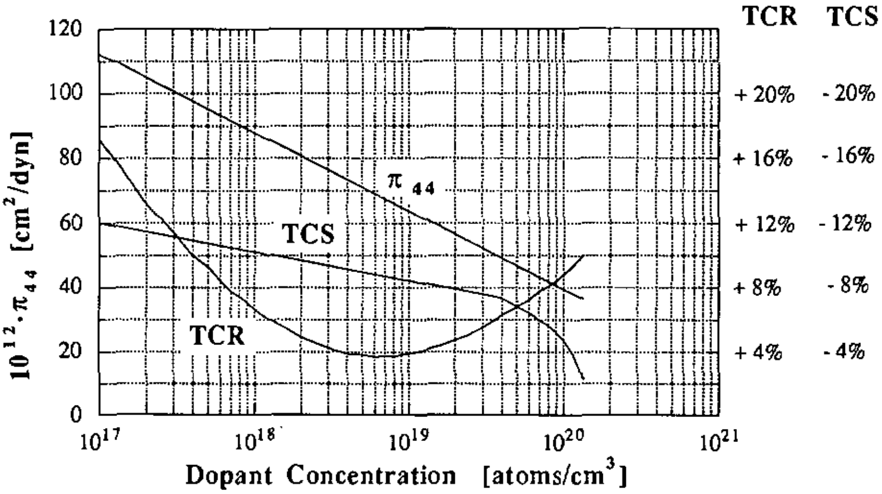

Fig. 7.10 TCR/55°C, TCS/55°C and π_{44} as a function of dopant concentration [189] (note that TCR and TCS are given for the temperature range of 55°C)

TCS/55°C and π_{44} as a function of dopant concentration of piezoresistors [189]. In section 1.5 we have seen that the sensitivity of a [110] orientated p-type piezoresistor is mainly the product of the piezoresistive coefficient π_{44} and the longitudinal stress. Thus both factors contribute to the temperature dependence of the sensitivity.

Figure 1.3 of section 1.5 indicates a decreasing piezoresistance factor for increasing temperatures. For a dopant concentration of $5\cdot10^{17}$ atoms/cm^{3}, which corresponds to that of our piezoresistors, we find from Fig. 7.10 a TCS of about -0.2%/°C which corresponds to the measured value. Thus we conclude that the influence of thermal stress on the TCS is minimal. However, the temperature dependence of the stress can not be neglected a priori, since passivation layers having different expansions coefficients than silicon can affect the stress distribution in the beams at different temperatures.

Theoretically, the Wheatstone bridge output at zero acceleration is independent of temperature if the four resistors have equal (not necessarily zero) temperature coefficients. Indeed, in this ideal case, temperature variations have a common-mode effect but do not influence the differential output of the bridge. In reality, however, the offset is temperature dependent, partly because the temperature coefficients of the resistors are not equal and partly because stress is introduced by thermal expansion of the different layers that constitute the suspensions of the seismic mass.

For the piezoresistive accelerometers developed in this work no compensation circuit was foreseen, since such concepts are well known from the fabrication of compensated piezoresistive pressure sensors, and furthermore such a circuit could be easily added using thick film and hybrid technology. However the basic ideas of compensation circuits, as mainly used for piezoresistive sensors, are briefly discussed below.

In most cases an additional circuit compensates for four parameters of the sensor output : offset of the Wheatstone bridge (O), normalization of full scale output (FSO) and temperature compensation of both sensitivity (TCS) and offset (TCO). The circuit might include resistors, thermistors, diodes and transistors for compensation and some amplifiers for signal amplification [83]. A more effective means is the use of a microprocessor to store the performance related parameters for an individual sensor and to compensate for temperature effects by an appropriate algorithm. Since all compensation techniques are based on the same background, we will only discuss the passive compensation for a constant voltage supply. As can be seen in Fig. 7.11, several resistors are added to the Wheatstone bridge. It should be noted that all the external resistors are assumed to have zero temperature coefficient of resistance. Hence only the sensor responds to temperature. Resistors R_1 and R_1' allow to balance the bridge. Resistor R_3 provides calibration of full scale output since it decreases the bridge voltage. As it was discussed previously the accelerometer chip exhibits a negative temperature coefficient of sensitivity. To compensate for this the bridge voltage which is proportional to the sensitivity has to increase with temperature. This requires insertion of a resistor (R_4) in series with the sensor bridge. A series and a shunt resistor in a given arm will affect the offset in opposite directions while affecting TCO in

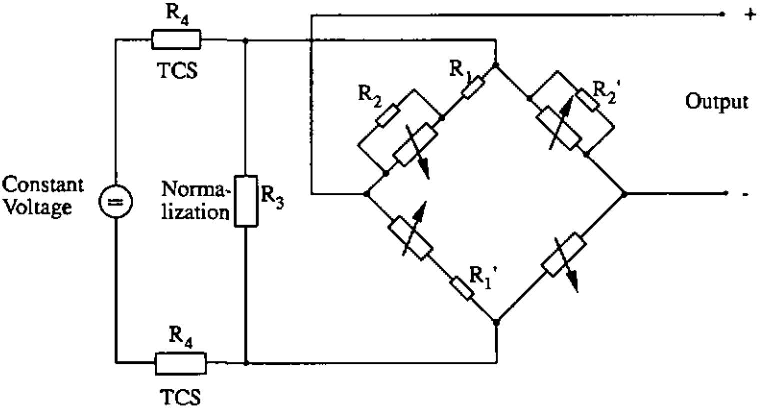

Fig. 7.11 Compensation circuit for constant voltage supply

the same direction. In general, a unique combination of a series (R_1) and a shunt resistor (R_2) in an appropriate arm exists which will both compensate the TCO and set the offset to zero at room temperature.

The constant current supply of a piezoresistive sensor provides a possibility for a simple temperature compensation. In this case the full scale output is the product of current, sensitivity and bridge resistance. As can be seen in Fig. 7.10, for a given dopant concentration of $3 \cdot 10^{17}$ atoms/cm^3 TCR and TCS are approximately equal with opposite sign. Thus bridge resistance and hence bridge voltage increases with temperature and partially compensates a decrease in sensitivity, providing a simple temperature compensation technique.

All the parameters which are compensated for do not depend linearly on temperature. Therefore using passive elements delivers only a two point temperature compensation, where the parameter has the same value at two different temperatures. Thus a linear compensated response cannot be achieved with a passive circuitry.

7.5 CONCLUSIONS

The preceding results have shown that critical damping of the accelerometer can be achieved by oil or air films. For both fluids the damping force depends on the film thickness as well as on the viscosity. Due to the much greater viscosity of oil over gas distances for critical damping are about one order of magnitude larger for oil. Thus the encapsulation of oil-damped devices does not require a high degree of precision, whereas an increase of 2 µm of the cavity's size strongly affects the frequency response of air-damped devices. The major drawback of oil as a damping medium compared to gas is the reduction of both resonance frequency and sensitivity which are mainly due to the buoyant force and a virtual added mass because the fluid surrounding the moving structure must also be accelerated. Since the viscosity of liquids decreases for increasing temperature, the device becomes less damped at elevated temperatures. In addition, the dependence of the viscosity on temperature is quite large. On the other hand the liquid increases the thermal mass of the accelerometer and makes it less susceptible to small fluctuations in temperature. It may also, depending on its thermal conductivity, help keep the sensing resistor and the temperature compensation circuit at the same temperature. Therefore liquid-damped devices might be useful for small temperature and small frequency range applications.

As the effect of the buoyant force and added mass on gas-damped devices is negligible, air-damped accelerometer are advantageous. Furthermore the viscosity of air is less temperature dependent than that of oil. The increasing viscosity of gases for increasing temperature reduces the usable frequency range of a gas-damped accelerometer for increasing temperature, an effect which is in opposition to liquid damped devices. Since air damping has shown a negligible influence on pressure, the damping behaviour of hermetically sealed accelerometers will not be affected by the increasing pressure caused by increasing temperature. The mounting with the unique feature that the air-damped sensor chips were only clamped in the metallic housing withstood shocks up to 1000 *g*. The deflection of the mass was limited by mechanical stoppers integrated into the silicon caps below and above the sensor chip.

For both damping mediums the squeeze film theory allowed the dependence of the damping on the viscosity, damping film thickness and dimensions of the moving mass to be investigated. The calculated film thickness needed for critical damping corresponded well with the measured data. Therefore this theory is suitable to give a first estimate of the cavity size for newly designed devices and different damping mediums.

The temperature dependence of offset and sensitivity corresponds to that expected from a piezoresistive sensor. It is caused by the asymmetry of the resistors and by the temperature dependence of the piezoresistive coefficients. Passive or active circuits can be used to compensate for the temperature dependence.

As a summary of this chapter the main specifications of an air-damped four-beam bridge-type accelerometer are summarized in Table 7.II.

Table 7.II Main specifications of an air-damped four-beam bridge-type accelerometer

Range	± 50 *g*
Sensitivity	170 - 200 μV/V *g*
Zero Acceleration Output	4 - 7 mV/V
Non-Linearity	± 1 % FS
Useful Frequency Range	0 - 1200 Hz
Input & Output Resistance	3 - 3.5 kΩ
Acceleration Limits	1000 *g*
Supply Voltage	5 V
Operating Temperature	-40°C to + 120°C
Temperature Coefficient of Sensitivity (uncompensated)	-0.2%/°C
Temperature Coefficient of Offset (uncompensated)	± 0.3%/°C

7.6 COMPARISON WITH COMMERCIAL DEVICES

Table 7.III shows a comparison of piezoresistive accelerometers, which are commercially available from three different manufacturers. All these low cost devices have an acceleration range of 50 *g*, but they are neither temperature compensated nor amplified. This allows their main parameters to be compared with the device developed in this work. It can be seen that all sensitivities are similar, but the device developed in this work exhibits a much higher resonance frequency. Since this air-damped device is critically damped its useful frequency range is much greater than that of the other accelerometers. On the other hand it is very difficult to judge the different approaches since no detailed information about the commercial devices are available. Factors such as size of the sensor chip as well as the mass-beam configuration have to be taken into account for a valuation of the different products.

Table 7.III Comparison of piezoresistive accelerometers from different manufacturers, without any amplification circuit and temperature compensation

Manufacturer	Kulite	SensoNor	ICSensors	This work
Type	GY-155	SA20	Model 3021	four-beam bridge-type
Range	± 50 *g*	± 50 *g*	± 50 *g*	± 50 *g*
Sensitivity	170 µV/V *g*	200 µV/V *g*	200 µV/V *g*	190 µV/V *g*
Resonance Frequency	2 kHz	1.5 kHz	1.8 kHz	5 kHz

Chapter 8
Conclusions

The goal of this thesis was the simulation, design and characterization of piezoresistive silicon accelerometers fabricated by a bipolar-compatible process. This type of sensor has an enormous market potential due to its excellent price/performance ratio. The work presented in this thesis aimed to produce a silicon accelerometer with a 50 *g* range (1 *g* = 9.81 ms^{-2}), being protected against an overload of 1000 *g* and having a usable frequency range greater than 1 kHz. In this final chapter the major conclusions of the previous chapters are recapitulated. At the end some improvements are suggested and future development trends are shown.

The sensor chip was fabricated entirely out of monocrystalline silicon, e.g. the silicon seismic mass is suspended by thin silicon beams. Basically two mass-beam configurations can be distinguished - the bridge-type having its mass suspended from opposite sides and the cantilever-type with its mass suspended from only one side. We fabricated one cantilever-type and two bridge-type accelerometers. These sensitive elements were simulated using classical formulae and finite element modeling. The chosen bipolar compatible process implied an epitaxial layer thickness of 12 µm which in turn fixed the thickness of the beams. Since a high sensitivity is advantageous, the width of the beams should be minimized. Its minimum is defined by the lateral size of the piezoresistors. Thus for a given overall chip size (sum of the side length of the mass and twice the length of the beam) the only free parameter of a quadratic four-beam bridge-type accelerometer design remains the length of the beams. We developed an analytical formulae for the beam length leading to the maximum possible sensitivity for a given chip size taking into account the dimensions of the piezoresistors. Results of analytical calculations were in good agreement with finite element analysis. However, the latter simulation technique allows more detailed prediction of the characteristics of the device since boundary effects, additional layers, temperature effects and nonlinearities might be taken into account. The transverse sensitivity of the bridge-type accelerometer can, in principle, be eliminated by electrical means, e.g. by positioning the four sensing resistors of the Wheatstone bridge in an appropriate manner on the beams.

Moreover, the compatibility with a bipolar fabrication process required aluminum as interconnection material. This restriction necessitated dry etching for the definition of the beams out of the membrane. The plasma process parameters for two gas mixtures (C_2ClF_5/SF_6 and SF_6/O_2) was optimized with regard to a good selectivity towards IC compatible masking material and an etch rate of ≈ 1 μm/min. Both gas mixtures exhibited a selectivity to standard photoresist high enough to pierce through a 12 μm thick silicon membrane using a photoresist mask. The fluorine/oxygen process (SF_6/O_2) showed a rather isotropic etch behaviour. However, given prior knowledge to the reproducible undercut, these effects can be compensated for by an appropriate design. Vertical walls were obtained using a C_2ClF_5/SF_6 plasma. Furthermore the fabrication of the first prototype in our laboratory has shown the importance of etch compensation structures to avoid undercutting of the convex corners of the silicon proof mass by KOH (40% at 60°C). Five different compensation designs were simulated and compared with etched samples. The most promising was optimized and resulted in a sharp convex corner of the silicon mass of the second prototype.

Based on these developments the second generation of the sensor chip was completely fabricated at ASCOM, maintaining full bipolar process compatibility. In addition the four electrode electrochemical etch-stop was used to obtain a well controlled beam thickness. This parameter is of greatest importance for the sensor performance, since a variation of 1 μm in the thickness affects the sensitivity by 17%.

One of the key processes is the critical damping of the sensor chip and its overrange protection. This was achieved by enclosing the device in a small cavity formed by under- and overlying wafers and having integrated stoppers. Either liquids or gases can be used as damping fluids. Since the viscosity of liquids is more temperature dependent than that of gases, the gas damped devices exhibited less dependence of damping on temperature. Further disadvantages of liquid damping compared to a device in vacuum were the about 60% loss of sensitivity due to the buoyant force and the about 50% reduction of the resonance frequency, which resulted in a reduced usable frequency range for the device. The theory of squeeze film was applied to simulate the damping of encapsulated accelerometers. For both damping mediums (air and silicon oil) the theoretically predicted thickness of the damping film for critical damping corresponded within 10% to that of measured devices. The theoretical considerations have shown, that a thin air film in the frequency range below 10 kHz acts only as a viscous damper on the moving mass. In our case the spring force is so small that it can be neglected. Thus no loss of sensitivity is caused by the air-damping. Since liquids exhibit a much higher viscosity than gases, oil-damped devices require a damping film 10 times larger than air-damped devices.

As mentioned above, in order to achieve damping and overrange protection the sensitive die can be enclosed from both sides by pre-etched parts which form the cavity. However, the reliable low temperature (< 450°C) wafer-to-wafer bonding is not straightforward. We have chosen a chip-by-chip mounting technique since it uses an adapted industrial process from the company KELLER well-known for the encapsulation of piezoresistive pressure sensors. The sensitive dies of air-damped accelerometers were enclosed by two pre-etched silicon chips with integrated mechanical stoppers. The mounting, with the unique feature that the sensor chips were only clamped in the metallic housing, withstood shocks up to 1000 *g*. Such encapsulated devices had a usable frequency range of 2.4 kHz at room temperature. Their sensitivity was about 190 µV/V *g* having a 50 *g* range of acceleration. Measurements on oil-encapsulated accelerometers showed a large temperature dependence of the damping, reduced sensitivity and resonance frequency compared to air-damped devices. Most of the important parameters of an accelerometer have also been calculated theoretically. These results were in good agreement with the measured values.

The work on accelerometers has shown that two steps are of greatest importance : precise control of the beam thickness and a reliable encapsulation technique. The control of the beam thickness was realized by applying the electrochemical etch-stop. To encapsulate the sensor chip we have chosen the time consuming chip-by-chip mounting technique, but for industrialization this step should be either fully automated or replaced by a bonding technique on the wafer level. A reliable low-temperature wafer-to-wafer bonding technique with a wafer which has passed through a 10 masks process has still to be developed. However, such a technique might result in a loss of the bipolar compatibility. This is not very important since micromachined accelerometers will not have the electronic circuitry integrated on the same chip in the near future due to the poor yield of a complete integration. A thorough investigation and statistical analysis should also be done on the long term stability of these devices including the influence of the encapsulation and of different passivation layers on the device performance.

The comparison to commercial piezoresistive accelerometers with the same acceleration range has shown that the developed four-beam bridge-type accelerometer exhibits a similar sensitivity but a much higher resonance frequency. However it is very difficult to judge the different approaches since no detailed information about the commercial devices and their fabrication technology are available. Factors such as size of the sensor chip as well as the mass-beam configuration have to be taken into account for a valuation of the different devices.

This work shows a systematic analysis of every development step of a piezoresistive accelerometer. Design rules for optimized sensitivity, a bipolar compatible fabrication process, formulae to calculate the cavity size for critical

damping and an encapsulation technique allow piezoresistive accelerometers with application specific characteristics to be fabricated.
The trend of accelerometers is towards higher mechanical symmetry and arbitrarily formed beams, which might have a potential for higher sensitivity from the same chip size. Another trend is for further integration, e.g. for surface micromachined accelerometers with integrated detection circuitry. All these developments are only possible due to thorough finite element modeling and some new fabrication technologies. Nevertheless the small size and the low cost potential of batch fabrication render the piezoresistive silicon accelerometer extremely attractive for a huge number of applications.

Acknowledgments

For my involvement and education in silicon sensors I am indebted to Prof. Dr. N. de Rooij, who offered me the chance to write this thesis. I am very grateful to him for his guidance, stimulation and advice. The Institute of Microtechnology (IMT) of the University of Neuchâtel has been a stimulating research environment. I would like to thank all members for the many bits of help. In particular, I acknowledge the collaboration with Christian Linder to develop the plasma etching. I liked the improvements on the text proposed by Philippe Arquint and Jürgen Brugger. I am very much indebted to David J. Strike, who corrected the whole manuscript with great care and devotion, and who is a very kind person.

The devices described in this thesis were fabricated at ASCOM, and I would like to express my appreciation to its staff members. Special thanks I owe to Stéphane Ansermet, Jörg Berthoud, Alex Bezinge, Hu Bo and Gérard Rossier.

The encapsulation of the devices was developed in collaboration with KELLER AG, Winterthur. The stimulating interest and fruitful discussions were very motivating. I would like to thank Heinz Krauer, Markus Schnyder and Rolf Müller for their careful and precise work. The sessions with H.W. Keller have shown me the business part of sensor development.

Further I thank Dr. J. Knutti from Silicon Microstructures Inc. California, Dr. H. Seidel from MBB Munich, and Prof. Dr. A. Shah from the Institute of Microtechnology of the University of Neuchâtel for kindly agreeing to be examiners.

I highly appreciated the help and exchange of information from the members at CSEM Neuchâtel in particular B. Duvanel, P. Balmer, J. Bergqvist and M. Bogdanski. The nice pictures have been taken by C. Ketterer (CSEM), M. Perdrix (CSEM), G. Racine (IMT) or M. Grétillat (IMT).

I especially acknowledge the financial support of the Committee for the Promotion of Applied Scientific Research, Switzerland.

Not only the help on my work, but also the free time I spent with very kind persons was of great importance. Many unmentioned nice persons contributed to my psychological equilibrium. Special thanks I owe to Jessica Herschkowitz for improving the English of some publications as well as for her friendship and support during the past two years.

References

[1] Prognos Weltreport *Sensortechnik 2000* (Sept. 1988)

[2] bp informiert, *Enormes Wachstum bei Sensoren*, Informationsbrief Nr. 80, Burster Präzisionsmesstechnik, Gernsbach, Dez. 1990

[3] J. Bryzek, K. Petersen, J. Mallon, L. Christel, F. Pourahmadi, *Silicon Sensors and Microstructures*, published by NOVA Sensors (1990)

[4] Fachbeilage Mikroperipherik, Bd. 5 Heft 1 (1991) pp. IV-V

[5] S. Middelhoek, A. Hoogerwerf, *Smart Sensors : When and Where ?* Sensors and Actuators, 8 (1) (1985) pp. 39-48

[6] P. Barth, F. Pourahmadi, R. Mayer, J. Poydock, K. Petersen, *A Monolithic Silicon Accelerometer with Integral Air Damping and Overrange Protection*, Tech. Digest of IEEE Solid-State Sensor and Actuator Workshop, Hilton Head Island, USA (1988) pp. 35-38

[7] H. Schlaak, F. Arndt, A. Steckenborn, H. Gevatter, L. Kiesewetter, H. Grethen, *Micromechanical Capacitive Acceleration Sensor with Force Compensation*, Proceedings of MICRO SYSTEM Technologies, Berlin (1990) pp. 617-622

[8] F. Rudolf, A. Jornod, P. Bencze, Silicon Microaccelerometer, Tech. Digest of 4th Int. Conf. Solid-State Sensors and Actuators (Transducers '87) Tokyo, Japan (1987) pp. 395-398

[9] H. Seidel, H. Riedel, R. Kolbeck, G. Mück, W. Kupke, M. Königer, *Capacitive Silicon Accelerometer with Highly Symmetrical Design*, Sensors and Actuators, A21 - A23 (1990) pp. 312-315

[10] S. McArthur, I. Holm-Kennedy, *Air Loading Effects on a Capacitively Sensed Membrane Supported Silicon Accelerometer*, Tech. Digest of IEEE Solid-State Sensor and Actuator Workshop, Hilton Head Island, USA (1986)

[11] R. Buckhorst, B. Hosticka, H. Seidel, *CMOS Readout Electronics for Capacitive Acceleration Sensors*, Proceedings of MICRO SYSTEM Technologies, Berlin (1990) pp. 636-641

[12] M. van Paemel, *Interface Circuit for Capacitive Accelerometer, Sensors and Actuators*, 17 (1989) pp. 629-637

[13] H. Leuthold, F. Rudolf, *An ASIC for High-resolution Capacitive Microaccelerometers*, Sensors and Actuators, A21 - A23 (1990) pp. 278-281

[14] ICSensors, Brochure on Silicon Accelerometers

[15] F. Rudolf, A. Jornod, J. Bergqvist, H. Leuthold, *Precision Accelerometers with μg Resolution*, Sensors and Actuators, A21 - A23 (1990) pp. 297-302

[16] W. Mason, *Piezoelectric Crystals and Their Application to Ultrasonics*, New York, Van Nostrand (1950)

[17] P. Chen, R. Muller, R. Jolly, G. Halac, R. White, A. Andrews, T. Lim, *Integrated Silicon Microbeam PI-FET Accelerometer*, IEEE Trans. on Electron Devices, ED-29 (1982) pp. 27-33

[18] P. Chen, R. Muller, A. Andrews, *Integrated Silicon Pi-FET Accelerometer with Proof Mass*, Sensors and Actuators, 5 (1984) pp. 119-126

[19] B. Puers, L. Reynaert, W. Snoeys, W. Sansen, *A New Uniaxial Accelerometer in Silicon Based on The Piezojunction Effect*, IEEE Trans. on Electron Devices, ED-35 (1988) pp. 764-770

[20] J. Neumeister, G. Schuster, W. von Münch, *A Silicon Pressure Sensor Using MOS Ring Oscillator*, Sensors and Actuators, 7 (1985) pp. 167-176

[21] D. Satchell, J. Greenwood, *A Thermally-Excited Silicon Accelerometer*, Sensors and Actuators, 17 (1989) pp. 241-245

[22] S. Chang, M. Putty, D. Hicks, C. Li, R. Howe, *Resonant-bridge Two-axis Micro-accelerometer*, Sensors and Actuators, A21 - A23 (1990) pp. 342-345

[23] R. Hiratsuka, D. van Duyn, T. Otaredian, P. de Vries, *A Novel Accelerometer Based on a Silicon Thermopile*, Tech. Digest of 6th Int. Conf. Solid-State Sensors and Actuators (Transducers '91) San Francisco, USA (1991) pp. 420-423

[24] M. Ohkawa, M. Izutsu, T. Sueta, *Integrated Optic Accelerometer Employing a Cantilever on a Silicon Substrate*, Jpn. J. Appl. Phys., 28 (1989) pp. 287-288

[25] L. M. Roylance, J. Angell, *A Batch-Fabricated Silicon Accelerometer*, IEEE Trans. on Electron Devices, ED-26 (1979) pp. 1911-1917

[26] K. Petersen, A. Shartel, N. Raley, *Micromechanical Accelerometer Integrated with MOS Detection Circuitry*, IEEE Trans. on Electron Devices, ED-29 (1982) pp. 23-27

[27] F. Rudolf, *A Micromechanical Capacitive Accelerometer with a Two-Point Inertial-Mass Suspension*, Sensors and Actuators, 4 (1983) pp. 191-198

[28] W. Benecke, L. Csepregi, A. Heuberger, K. Kühl, H. Seidel, *A Frequency-Selective, Piezoresistive Silicon Vibration Sensor*, Tech. Digest of 3rd Int. Conf. Solid-State Sensors and Actuators (Transducers '85) Philadelphia, USA (1985) pp. 105-108

[29] M. Tsugai, M. Bessho, *Semiconductor Accelerometer for Automotive Controls*, Tech. Digest of 4th Int. Conf. Solid-State Sensors and Actuators (Transducers '87) Tokyo, Japan (1987) pp. 403-405

[30] M. Nakamura, K. Murakami, H. Nojiri, T. Tominaga, *Novel Electrochemical Micro-Machining and its Application for Semiconductor Acceleration Sensor IC*, Tech. Digest

of 4th Int. Conf. Solid-State Sensors and Actuators (Transducers '87) Tokyo, Japan (1987) pp. 112-115

[31] H. Sandmaier, K. Kühl, E. Obermeier, *A Silicon Based Micromechanical Accelerometer with Cross Acceleration Sensitivity Compensation,* Tech. Digest of 4th Int. Conf. Solid-State Sensors and Actuators (Transducers '87) Tokyo, Japan (1987) pp. 399-402

[32] J. Knutti, *Silicon Microstructure Sensors,* publication of ICSensors Europe Headquarters

[33] D. Olney, *Acceleration Measurement Using Variable Capacitance,* Proceedings of Sensor 88, Nürnberg, F.R.G (1988) pp. 149-160

[34] S. Terry, D. de Bruin, H. Allen, *Self-testable Accelerometer Microsystem,* Proceedings of MICRO SYSTEM Technologies, Berlin (1990) pp. 611-616

[35] H. Allen, S. Terry, D. de Bruin, *Accelerometer Systems with Self-testable Features,* Sensors and Actuators, A21 - A23 (1990) pp. 153-161

[36] H. Allen, S. Terry, D. de Bruin, *Accelerometer Systems with Built-in Testing,* Sensors and Actuators, A21 - A23 (1990) pp. 381-386

[37] W. Henrion, L. DiSanza, M. Ip, S. Terry, H. Jerman, *Wide Dynamic Range Direct Digital Accelerometer,* Tech. Digest of IEEE Solid-State Sensor and Actuator Workshop, Hilton Head Island, USA (1990) pp. 153-157

[38] S. Suzuki, S. Tuchitani, K. Sato. S. Ueno, Y. Yokota, M. Sato, M. Esashi, *Semiconductor Capacitance-type Accelerometer with PWM Electrostatic Servo Technique,* Sensors and Actuators, A21 - A23 (1990) pp. 316-319

[39] K. Yamada, K. Higuchi, H. Tanigawa, *A Novel Silicon Accelerometer with a Surrounding Mass Structure,* Sensors and Actuators, A21 - A23 (1990) pp. 308-311

[40] W. Dunn, *Accelerometer Design Considerations,* Proceedings of MICRO SYSTEM Technologies, Berlin (1990) pp. 131-136

[41] R. Sulouff, *Silicon Sensors for Automotive Applications,* Tech. Digest of 6th Int. Conf. Solid-State Sensors and Actuators (Transducers '91) San Francisco, USA (1991) pp. 170-176

[42] *Analog Devices Combines Micromachining and BiCMOS,* Semiconductor International (17) (October 91) p. 17

[43] J. Cole, *A New Sense Element Technology for Accelerometer Subsystems,* Tech. Digest of 6th Int. Conf. Solid-State Sensors and Actuators (Transducers '91) San Francisco, USA (1991) pp. 93-96

[44] B. Kloeck, *Design, Fabrication and Characterization of Piezoresistive Pressure Sensors, Including the Study of Electrochemical Etch-Stop,* Dissertation, University of Neuchâtel (1989)

[45] C. Smith, *Piezoresistance Effect in Germanium and Silicon,* Phys. Rev., 94 (1) (1954) pp. 42-49

[46] W. Mason, R. Thurston, *Use of Piezoresistive Materials in the Measurement of Displacement, Force and Torque,* J. Acoust. Soc. Am., 29 (1957) pp. 1096-1101

[47] F. Morin, T. Geballe, C. Herring, *Temperature Dependence of the Piezoresistance of High-Purity Silicon and Germanium,* Phys. Rev., 105 (2) (1957) pp. 525-559

[48] R. Keyes, *The Effects of Elastic Deformation on the Electrical Conductivity of Semiconductors,* in Solid State Physics, vol. 11, F. Seitz and D. Turnbell, Eds., New York, Academic Press (1960) pp. 149-221

[49] W. Pfann, R. Thurston, *Semiconducting Stress Transducers Utilizing the Transverse and Shear Piezoresistance Effects,* J. Appl. Phys., 32 (10) (1961) pp. 2008-2019

[50] O. Tufte, P. Chapman, D. Long, *Silicon Diffused-Element Piezoresistive Diaphragms,* J. Appl. Phys., 33 (11) (1962) pp. 3322-3327

[51] O. Tufte, E. Stelzer, *Piezoresistive Properties of Silicon Diffused Layers,* J. Appl. Phys., 34 (2) (1963) pp. 313-318

[52] D. Kerr, A. Milnes, *Piezoresistance of Diffused Layers in Cubic Semiconductors,* J. Appl. Phys., 34 (4) (Part 1) (1963) pp. 727-731

[53] O. Tufte, E. Stelzer, *Piezoresistive Properties of Heavily Doped n-Type Silicon,* Physical Review, 133 (6A) (1964) pp. A1705-A1716

[54] L. Kurbatov, I. Froimson, S. Shakhidzhanov, *Total Piezoresistance Tensor of p-Type Silicon in a Wide Temperature Range,* Sov. Phys. Semicond., 11 (5) (1977) pp. 586-587

[55] K. Yamada, M. Nishihara, S. Shimada, M. Tanabe, M. Shimazoe, Y. Matsuoka, *Nonlinearity of the Piezoresistance Effect of p-Type Silicon Diffused Layers,* IEEE Trans. on Electron Devices, ED-29 (1) (1982) pp. 71-77

[56] Y. Kanda, *A Graphical Representation of the Piezoresistance Coefficients in Silicon,* IEEE Trans. on Electron Devices, ED-29 (1) (1982) pp. 64-70

[57] F. Khan, P. Allen, *Temperature Dependence of the Elastic Constants of* p^+ *- Silicon,* Phys. stat. sol. (b), 128 (31) (1985) pp. 31-38

[58] D. Schubert, *Piezoresistive Properties of Polycrystalline and Crystalline Silicon Films,* Sensors and Actuators, 11 (1987) pp. 145-155

[59] Y. Wang, M.H. Bao, L.Z. Yu, *The Effect of Shear Stress on the Piezoresistance of Silicon,* Sensors and Actuators, 18 (1989) pp. 221-231

[60] K. Matsuda, Y. Kanda, K. Yamamura, K. Suzuki, *Nonlinearity of Piezoresistance Effect in p- and n- Type Silicon,* Sensors and Actuators, A21 - A23 (1990) pp. 45-48

[61] K. Petersen, *Silicon as a Mechanical Material,* Proceedings of the IEEE, 70 (5) (1982) pp. 420-457

[62] H. Seidel, L. Csepregi, *Three-Dimensional Structuring of Silicon for Sensor Applications,* Sensors and Actuators, 4 (1983) pp. 455-463

[63] C. Herring, *Transport Properties of a Many-Valley Semiconductor,* Bell System Technical Journal, 34 (2) (1955) pp. 237-290

[64] T. Tschan, N. de Rooij, A. Bezinge, S. Ansermet, J. Berthoud, *Characterization and Modelling of Silicon Piezoresistive Accelerometers Fabricated by a Bipolar-compatible Process,* Sensors and Actuators, A25 - A27 (1991) pp. 605-609

[65] T. Tschan, N. de Rooij, A. Bezinge, *Analytical and FEM Modeling of Piezoresistive Silicon Accelerometers: Prediction and Limitation with Respect to Experiments,* Sensors and Materials, Vol. 3, No. 4 (1992) pp. 189-203

[66] H. Baltes, *Design and Simulation of Sensors,* Proceedings of MICRO SYSTEM Technologies, Berlin (1990) pp. 117-123

[67] O. Zienkiewicz, *The Finite Element Method in Engineering Science,* McGraw-Hill (1971)

[68] B. Puers, E. Peeters, W. Sansen, *CAD Tools in Mechanical Sensor Design,* Sensors and Actuators, 17 (1989) pp. 423-429

[69] M. Mirza, F. Abdullah, L. Finkelstein, *Analysis and Design of Piezoresistive Pressure Sensors using The Finite-Element Method,* Transactions of the Institute of Measurement and Control ,13 (1) pp. 36-40

[70] F. Pourahmadi, P. Barth, K. Petersen, *Modeling of Thermal and Mechanical Stresses in Silicon Microstructures,* Sensors and Actuators, A21 - A23 (1990) pp. 850-855

[71] H. Seidel, L. Csepregi, *Design Optimization for Cantilever-Type Accelerometers,* Sensors and Actuators, 6 (1984) pp. 81-92

[72] H. Reimann, *New Mechanical Structures to Achieve Low Pressure Silicon Sensors and Accelerometers,* Proceedings of Sensor 88, Nürnberg, F.R.G (1988) pp. 265-280

[73] S. Timoshenko, J. Goodier, *Theory of Elasticity,* Third Edition, McGraw-Hill Book Company (1970)

[74] R. Roark, W. Young, *Formulas for Stress and Strain,* Fifth Edition, McGraw-Hill International Edition (1986)

[75] R. Blevins, *Formulas for Natural Frequency and Mode Shape,* R. Krieger Publishing Company (1979)

[76] S. Timoshenko, *Strength of Materials Part I and II,* Robert E. Krieger Publishing Company, Malabar, Florida (1956)

[77] I. Bronstein, K. Semendjajew, *Taschenbuch der Mathematik,* Verlag Harri Deutsch, Thun u. Frankfurt/Main (1983) pp. 640-643

[78] S. Timoshenko, *Strength of Materials Part I,* Robert E. Krieger Publishing Company, Malabar, Florida (1956) p. 186, eq. 111

[79] A. Heuberger, *Mikromechanik,* Springer Verlag (1989)

[80] S. Timoshenko, D. Young, W. Weaver, *Vibration Problems in Engineering*, Fourth Edition, John Wiley & Sons (1974)

[81] I. Szabo, *Höhere Technische Mechanik*, Springer-Verlag (1977) pp. 83-85

[82] A. Kayal, N. Rauch, *Anwendungsspezifische intelligente Sensoren ("ASIS"): Silizium-Drucksensor mit integrierter Signalauswertung*, Elektronik, Heft 9 (1988)

[83] S. Ansermet, D. Otter, R. Craddock, J. Dancaster, *Cooperative Development of a Piezoresistive Pressure Sensor with Integrated Signal Conditioning for Automotive and Industrial Applications*, Sensors and Actuators, A21 - A23 (1990) pp. 79-83

[84] A. Heuberger, *Mikromechanik*, Springer Verlag (1989) pp. 366-369

[85] D. Moser, P. Sigg, S. Ansermet, H. Baltes, *Finite-Element Simulation of Silicon Accelerometers*, Proceedings of MICRO SYSTEM Technologies, Berlin (1990) pp. 125-130

[86] W. Germer, G. Kowalski, *Mechanical Decoupling of Monolithic Pressure Sensors in Small Plastic Encapsulations*, Sensors and Actuators, A21 - A23 (1990) pp. 1065-1069

[87] T. Tschan, C. Linder, N. de Rooij, *Dry Etching Techniques for Silicon Micromachining*, Proceedings of MME '90, Micromechanics Europe, Berlin (1990) pp. 253-260

[88] C. Linder, T. Tschan, N. de Rooij, *Deep Dry Etching Techniques as a New IC-compatible Tool for Silicon Micromachining*, Tech. Digest of 6th Int. Conf. Solid-State Sensors and Acutators (Transducers' 91) San Francisco, USA (1991) pp. 524-527

[89] C. Linder, T. Tschan, N. de Rooij, *Deep Dry Etching of Silicon - a Novel Micromachining Tool*, accepted for publication (Feb. 92) in Sensors and Materials

[90] S. Sze, *Semiconductor Devices, Physics and Technology*, John Wiley & Sons (1985) pp. 372-376

[91] G. Delapierre, *Micro-Machining: A Survey of the Most Commonly Used Processes*, Sensors and Actuators, 17 (1989) pp. 123-138

[92] R. Buser, B. Stauffer, N. de Rooij, *Realization of a Mesa Array in (001) Oriented Silicon Wafers for Tactile Sensing Applications*, Extended Abstracts, Electrochem. Soc., 86-2 (1986) pp. 879-880

[93] C. Mogab, *VLSI Technology* (ed. S.M. Sze, McGraw-Hill, New York, 1983) Chap. 8

[94] M. Zdeblick, P. Barth, J. Angell, *Microminiature Fluidic Amplifier*, Tech. Digest of IEEE Solid-State Sensor and Actuator Workshop, Hilton Head Island, USA (1986)

[95] K. Eisele, *SF_6, A Preferable Etchant for Plasma Etching Silicon*, J. Electrochem. Soc., 128 (1981) pp. 123-126

[96] Z. Zhang, N. MacDonald, *An RIE Process for Submicron, Silicon Electromechanical Structures*, Tech. Digest of 6th Int. Conf. Solid State Sensors and Actuators (Transducers' 91) San Francisco (1991) pp. 520-523

[97] R. Buser, J. Brugger, C. Linder, N.F. de Rooij, *Micromachined Silicon Cantilevers and Tips for Bidirectional Force Microscopy*, Tech. Digest of 6th Int. Conf. Solid State Sensors and Actuators (Transducers' 91) San Francisco (1991) pp.249-252

[98] R. Pinto, K. Ramanathan, R. Babu, *Reactive Ion Etching in SF_6 Gas Mixtures*, J. Electrochem. Soc., 134 (1987) pp. 165-175

[99] J. McVittie, C. Gonzalez, *Anisotropic Etching of Si Using $SF_6.C_2ClF_5$*, Extended Abstracts, Electrochem. Soc., 84-2 (1984) pp. 584-585

[100] M. Seel, P. Bagus, *Ab Initio Cluster Study of the Interaction of Fluorine and Chlorine Wwth the Si(111) Surface*, Phys. Rev. B, 28 (4) (1983) pp. 2023-2038

[101] L. Clark, D. Edell, *$KOH:H_2O$ etching of (110) Si, (111) Si, SiO_2 and Ta: an Experimental Study*, Proceedings of the IEEE Micro Robots and Teleoperators Workshop. An Investigation of Micromechanical Structures, Actuators and Sensors (1987) pp. 5/1 - 6

[102] H. Seidel, *The Mechanism of Anisotropic Silicon Etching and its Relevance for Micromachining*, Tech. Digest of 4th Int. Conf. Solid-State Sensors and Actuators (Transducers' 87) Tokyo, Japan (1987) pp. 120-125

[103] U. Schnakenberg, W. Benecke, B. Löchel, *NH_4OH-based Etchants for Silicon Micromachining*, Sensors and Actuators, A21 - A23 (1990) pp. 1031-1035

[104] H. Seidel, L. Csepregi, A. Heuberger, H. Baumgärtel, *Anisotropic Etching of Crystalline Silicon in Alkaline Solutions: I. Orientation Dependence and Behavior of Passivation Layers*, J. Electrochem. Soc., 137 (1990) pp. 3612-3626

[105] H. Seidel, L. Csepregi, A. Heuberger, H. Baumgärtel, *Anisotropic Etching of Crystalline Silicon in Alkaline Solutions: II. Influence of Dopants*, J. Electrochem. Soc., 137 (1990) pp. 3626-3632

[106] R. Jolly, R. Muller, *Miniature Cantilever Beams Fabricated by Anisotropic Etching of Silicon*, J. Electrochem. Soc., 127 (1980) pp. 2750-2754

[107] K. Bean, *Anisotropic Etching of Silicon*, IEEE Trans. on Electron Devices, ED-25 (10) (1978) pp. 1185-1193

[108] K. Bean, W. Runyan, *Dielectric Isolation: Comprehensive, Current and Future*, J. Electrochem. Soc., 124 (1977) pp. 5C-12C

[109] R. Buser, N. de Rooij, *Monolithisches Kraftsensorfeld*, VDI Berichte Nr. 677 (1988) pp. 115-118

[110] B. Puers, W. Sansen, *Compensation Structures for Convex Corner Micromachining in Silicon*, Sensors and Actuators, A21 - A23 (1990) pp. 1036-1041

[111] X. Wu, W. Ko, *Compensating Corner Undercutting in Anisotropic Etching of (100) Silicon*, Sensors and Actuators, 18 (1989) pp. 207-215

[112] X. Wu, W. Ko, *A Study on Compensating Corner Undercutting in Anisotropic Etching of (100) Silicon*, Tech. Digest of 4th Int. Conf. Solid-State Sensors and Actuators (Transducers' 87) Tokyo, Japan (1987) pp. 126-129

[113] H. Sandmaier, H. Offereins, K. Kühl, W. Lang, *Corner Compensation Techniques in Anisotropic Etching of (100)-Silicon using Aqueous KOH*, Tech. Digest of 6th Int. Conf. Solid-State Sensors and Actuators (Transducers '91) San Francisco (1991) pp. 456-459

[114] G. Mayer, H. Offereins, H. Sandmaier, K. Kühl, *Fabrication of Non-Underetched Convex Corners in Anisortopic Etching of (100)-Silicon in Aqueous KOH with Respect to Novel Micromechanic Elements*, J. Electrochem. Soc., 137 (1990) pp. 3947-3951

[115] H. Offereins, K. Kühl, H. Sandmaier, *Methods for the Fabrication of Convex Corners in Anisotropic Etching of (100) Silicon in Aqueous KOH*, Sensors and Actuators A, 25 - 27 (1991) pp. 9-13

[116] S. Linder, H. Baltes, P. Roggwiller, J. Voboril, *High-Index-Plane Etch Rates and Micromachining of Power Devices*, Tech. Digest of Micromechanics Europe, Berlin (1990) pp. 25-31

[117] G. Gerlach, *A Novel Mask Compensation Pattern for Etched Microstructures with Several Convex Corners*, Proceedings of MICRO SYSTEM Technologies 90, Berlin (1990) pp. 545-550

[118] R. Buser, N. de Rooij, *From the Mask Layout to the Performance of a Device : A Complete CAD System for Micromachined Monocrystalline Silicon Structures*, Tech. Digest Micromechanics Europe, Berlin (1990) pp. 7-13

[119] R. Buser, N. de Rooij, *ASEP : a CAD Program for Silicon Anisotropic Etching*, Sensors and Actuators A, 28 (1991) pp. 71-78

[120] R. Buser, *Theoretical and Experimental Investigations on Silicon Single Crystal Resonant Structures*, Thesis, University of Neuchâtel (1989)

[121] B. Kloeck, *Design, Fabrication and Characterization of Piezoresistive Pressure Sensors, Including the Study of Electrochemical Etch-stop*, Dissertation, University of Neuchâtel (1989) pp. 106-109

[122] H. Allen, S. Terry, J. Knutti, *Understanding Silicon Accelerometers*, expanded version of an article by the same title which appeared in Sensors (Sept. 89) pp. 17-31

[123] L. Roylance, *A Miniature Integrated Circuit Accelerometer for Biomedical Applications*, Ph.D. Thesis, Stanford University (1977)

[124] O. Glembocki, R. Stahlbush, *Bias-Dependent Etching of Silicon in Aqueous KOH*, J. Electrochem. Soc., 132(1985) pp. 145-151

[125] R. Smith, B. Kloeck, N. de Rooij, S. Collins, *The Potential Dependence of Silicon Anisotropic Etching in KOH at 60°C*, J. Electroanal. Chem., 238 (1987) pp. 103-113

[126] B. Kloeck, S. Collins, N. de Rooij, R. Smith, *Study of Electrochemical Etch-Stop for High Precision Thickness Control of Silicon Membranes*, IEEE Trans. on Electron Devices, ED-36 (4) (1989) pp. 663-669

[127] S. Lin, I. Pugacz-Muraszkiewicz, *Local Stress Measurement in Thin Thermal SiO_2 Films on Si Substrates*, J. Appl. Phys., 43 (1) (1972) pp. 119-125

[128] R. Jaccodine, W. Schlegel, *Measurement of Strains at Si-SiO_2 Interface*, J. Appl. Phys., 37 (6) (1966) pp. 2429-2434

[129] T. Ma, *Stresses in SiO_2-on-Si Structures*, Properties of Silicon, EMIS Datareview (June 87) pp. 650-661

[130] T. Tschan, N. de Rooij, A. Bezinge, *Oil-damped Piezoresistive Silicon Accelerometers*, Tech. Digest of 6th Int. Conf. Solid-State Sensors and Actuators (Transducers '91) San Francisco, USA (1991) pp. 112-114

[131] T. Tschan, N. de Rooij, A. Bezinge, *Damping of Piezoresistive Silicon Accelerometers*, Sensors and Actuators, 32 (1-3) (1992) pp. 567-571

[132] C. Robinson, D. Overman, R. Warner, T. Blomquist, *Problems Encountered in the Development of a Microscale g-Switch Using Three Design Approaches*, Tech. Digest of 4th Int. Conf. Solid-State Sensors and Actuators (Transducers '87) Tokyo, Japan (1987) pp. 410-413

[133] S. Terry, *A Miniature Silicon Accelerometer with Built-In Damping*, Tech. Digest of IEEE Solid-State Sensor and Actuator Workshop, Hilton Head Island, USA (1988) pp. 114-116

[134] D. de Bruin, H. Allen, S. Terry, *Second-order Effects in Self-testable Accelerometers*, Tech. Digest of IEEE Solid-State Sensor and Actuator Workshop, Hilton Head Island, USA (1990) pp. 149-152

[135] I. Szabo, *Einführung in die technische Mechanik*, 8. Aufl., Springer Verlag (1975)

[136] W. Bohl, *Technische Strömungslehre*, VOGEL Buchverlag Würzburg pp. 22-24

[137] J. Starr, *Squeeze-Film Damping in Solid-State Accelerometers*, Tech. Digest of IEEE Solid-State Sensor and Actuator Workshop, Hilton Head Island, USA (1990) pp. 44-47

[138] W. Langlois, *Isothermal Squeeze Films*, Quarterly of Appl. Mathematics, XX (2) (1962) pp. 131-150

[139] J. Blech, *Squeeze Films*, Technion Report EEC-111 (March 1981)

[140] J. Blech, *On Isothermal Squeeze Films*, J. of Lubrication Technology, 105 (Oct. 83) pp. 615-620

[141] W. Gross, *Gas Film Lubrication*, John Wiley and Sons Inc., New York (1962)

[142] R. Blevins, *Formulas for Natural Frequency and Mode Shape*, Robert E. Krieger Publishing Company, Malabar, Florida (1979) chapter 14, pp. 386-424

[143] McConnell, D. Young, *Added Mass of a Sphere in a Bounded Viscous Fluid*, J. Eng. Mech. Div., Am. Soc. Civil Engrs. 91, EM4 (1965) pp. 147-164

[144] N. Ackermann, A. Arbhabhirama, *Viscous and Boundary Effects on Virtual Mass*, J. Eng. Mech. Div., Am. Soc. Civil Engrs. 90, EM4 (1964) pp. 123-130

[145] H. Thomann, *Strömungslehre II*, AMIV-Verlag, ETH Zürich, pp. 128-131

[146] S. Timoshenko, D. Young, W. Weaver, *Vibration Problems in Engineering,* John Wiley & Sons, 4th ed. (1974) pp. 72-81

[147] C. Harris, *Shock and Vibration Handbook,* McGraw-Hill Book Comp., 3rd Ed. (1988)

[148] W. Griffin, H. Richardson, S. Yamanami, *A Study of Fluid Squeeze-Film Damping,* J. of Basic Engineering (June 1966) pp. 451-456

[149] KELLER AG für druckmesstechnik, St.Gallerstr. 119, CH-8404 Winterthur, phone ++41 52 29 11 26

[150] C. Harendt, H. Graf, E. Penteker, B. Höfflinger, *Wafer Bonding: Investigation and in situ Observation of the Bond Process*, Sensors and Actuators, A21 - A23 (1990) pp. 927-930

[151] C. Harendt, B. Höfflinger, H. Graf, E. Penteker, *Silicon Direct Bonding for Sensor Applications: Characterization of the Bond Quality,* Sensors and Actuators A, 25 - 27 (1991) pp. 87-92

[152] K. Petersen, P. Barth, J. Poydock, J. Brown, J. Mallon, J. Bryzek, *Silicon Fusion Bonding For Pressure Sensors,* Tech. Digest of IEEE Solid-State Sensor and Actuator Workshop, Hilton Head Island, USA (1988) pp. 144-147

[153] J. Lasky, S. Stiffler, F. White, J. Abernathey, *Silicon-on-Insulator (SOI) by Bonding and Etch-Back,* Int. Electron Devices Meeting (Dec. 85) pp. 684-687

[154] K. Mitani, V. Lehmann, U. Gösele, *Bubble Formation During Silicon Wafer Bonding: Causes and Remedies,* Tech. Digest of IEEE Solid-State Sensor and Actuator Workshop, Hilton Head Island, USA (1990) pp. 74-77

[155] M. Shimbo, K. Furukawa, K. Fukuda, K. Tanzawa, *Silicon-to-silicon Direct Bonding Method,* J. Appl. Phys. 60 (8) (1986) pp. 2987-2989

[156] T. Anthony, *Dielectric Isolation of Silicon by Anodic Bonding*, J. Appl. Phys., 58 (3) (1985) pp. 1240-1247

[157] S. Lu, Z. Zheng, Q. Tong, *A new Silicon Micromachining Method Using SOI/SDB Technology*, Sensors and Actuators, A21 - A23 (1990) pp. 961-963

[158] J. Lasky, *Wafer Bonding for Silicon-on-insulator Technologies,* Appl. Phys. Lett. 48 (1) (1986) pp. 78-80

[159] R. Black, S. Arthur, R. Gilmore, N. Lewis, E. Hall, R. Lillquist, *Silicon and Silicon Dioxide Thermal Bonding for Silicon-on-insulator Applications,* J. Appl. Phys. 63 (8) (1988) pp. 2773-2777

[160] M. Shimbo, K. Furukawa, K. Fukuda, *A Newly Developed Silicon to Silicon Direct Adhesion Method,* Extended Abstract, Electrochem. Soc., 232, pp. 337-338

[161] G. Pollak-Diener, *Mounting Techniques for Silicon Sensors,* Technisches Messen tm, 56 (11) (1989) pp. 422-427

[162] S. Iyer, C. Ting, P. Fryer, *Ambient Gas Effects on the Reaction of Titanium with Silicon*, J. Electrochem. Soc., 132 (9) (1985) pp. 2240-2245

[163] G. Krooshof, F. Habraken, W. van der Weg, L. Van den Hove, K. Maex, R. De Keersmaecker, Study of the Rapid Thermal Nitridation and Silicidation of Ti using Elastic Recoil Detection. II. Ti on SiO_2, J. Appl. Phys. 63 (10) (1988) pp. 5110-5114

[164] L. Brillson, M. Slade, H. Richter, H. Van der Plas, R. Fulks, *Titanium-silicon and Silicon Dioxide Reactions Controlled by Low Temperature Rapid Thermal Annealing*, J. Vac. Sci. Technol. A, 4 (3) (1986) pp. 993-997

[165] C. Ting, M. Wittmer, S. Iyer, S. Brodsky, *Interaction Between Ti and* SiO_2, J. Electrochem. Soc., 131 (12) (1984) pp. 2934-2938

[166] J. Bergqvist, F. Rudolf, J. Maisano, F. Parodi, M. Rossi, *A Silicon Condenser Microphone with a Highly Perforated Backplate*, Tech. Digest of 6th Int. Conf. Solid-State Sensors and Actuators (Transducers '91) San Francisco (1991) pp. 266-269

[167] C. den Besten, R. van Hal, J. Munoz, P. Bergveld, *Polymer Bonding of Micro-Machined Silicon Structures*, Proceedings of IEEE Micro Electro Mechanical Systems (1992) pp. 104-109

[168] L. Field, R. Muller, *Fusing Silicon Wafers with Low Melting Temperature Glas*, Sensors and Actuators, A21 - A23 (1990) pp. 935-938

[169] R. Legtenberg, S. Bouwstra, M. Elwenspoek, *Low-Temperature Glass Bonding for Sensor Applications*, Tech. Digest Micromechanics Europe (1990) pp. 94-97

[170] H. Reichl, *Packaging and Interconnection of Sensors*, Sensors and Actuators A, 25 - 27 (1991) pp. 63-71

[171] H. Quenzer, W. Benecke, C. Dell, *Low Temperature Wafer Bonding for Micromechanical Applications*, Proceedings of IEEE Micro Electro Mechanical Systems (1992) pp. 49-55

[172] E. Levin, C. Robbins, H. McMurdie, *Phase Diagrams for Ceramists (two volumes)*, The American Ceramic Society, Columbus, Ohio, 1060

[173] L. Field, R. Muller, *Low-Temperature Silicon-Silicon Bonding With Oxides*, Extended Abstract, Electrochem. Soc., May 1987, 87-1, No. 232 (1987) pp. 333-334

[174] W. Ko, J. Suminto, G. Yeh, *Bonding Techniques for Microsensors*, Micromachining and Micropackaging of Transducers, ed. C. Fung, P. Cheung, W. Ko, D. Fleming, Elesevier Science Puzblishers, Amsterdam (1985) pp. 41-61

[175] J. Vossen, W. Kern, *Thin Film Processes*, Academic Press, New York (1978)

[176] A. Hannebrog, *Silicon Wafer Bonding Techniques for Assembly of Micromechanical Elements*, Proceedings of IEEE Micro Electro Mechanical Systems, Japan (1991) pp. 92-98

[177] A. Hanneborg, M. Nese, P. Ohlckers, *Silicon-to-Silicon Anodic Bonding*, Tech. Digest of Micromechanics Europe, Berlin (1990) pp. 100-107

[178] H. Offereins, H. Sandmeier, B. Folkmer, U. Steger, W. Lang, *Stress Free Assembly Technique for a Silicon Based Pressure Sensor*, Tech. Digest of 6th Int. Conf. Solid-State Sensors and Actuators (Transducers '91) San Francisco, USA (1991) pp. 986-989

[179] M. Esashi, A. Nakano, S. Shoji, H. Hebiguchi, *Low-temperature Silicon-to silicon Anodic Bonding with Intermediate Low Melting Point Glass,* Sensors and Actuators, A21 - A23 (1990) pp. 931-934

[180] A. Hanneborg, P. Ohlckers, *A Capacitive Silicon Pressure Sensor with Low TCO and High Long-Term Stability,* Sensors and Actuators, A21-A23 (1990) pp. 151-154

[181] R. Zengerle, A. Richter, H. Sandmaier, *A Micro Membrane Pump with Electrostatic Actuation*, Proceedings of IEEE Micro Electro Mechanical Systems (1992) pp. 19-25

[182] R. Holm, T. Kvisteroy, H. Jakobsen, A. Hanneborg, P. Ohlckers, *Stability and Common Mode Sensitivity of Piezoresistive Silicon Pressure Sensors Made by Different Mounting Methods*, Tech. Digest of 6th Int. Conf. Solid-State Sensors and Actuators (Transducers '91) San Francisco, USA (1991) pp. 978-981

[183] H. Quenzer, W. Benecke, *Low Temperature Silicon Wafer Bonding,* will be published in Sensor and Actuators (Feb. 92) presented at Eurosensors V in Rome (1991)

[184] K. Yamada, T. Kuriyama, *A New Modal Mode Controlling Method for a Surface Format Surrounding Mass Accelerometer*, Tech. Digest of 6th Int. Conf. Solid-State Sensors and Actuators (Transducers '91) San Francisco, USA (1991) pp. 655-658

[185] ICSensors, *Temperature Compensation Techniques for Piezoresisitive Accelerometers*, Technical Note TN-009, (April 1988)

[186] P. Kopystynski, E. Obermeier, *An Interchangeable Silicon Pressure Sensor with On-Chip Compensation Circuitry*, Sensors and Actuators, 18 (1989) pp. 239-245

[187] J. Böttcher, *Software korrigiert Drucksensor*, Elektronik 15 (July 1989) pp. 38-42

[188] H. Kress, F. Bantien, J. Marek, M. Willmann, *Silicon Pressure Sensor with Integrated CMOS Signal-conditioning Circuit and Compensation of Temperature Coefficient,* Sensors and Actuators A, 25 - 27 (1991) pp. 21-26

[189] J. Bryzek, K. Petersen, J. Mallon, L. Christel, F. Pourahmadi, *Silicon Sensors and Microstructures,* published by NOVA Sensor (1990) chapter 4